Doctoral Thesis

Structural study for mitochondrial quality control

Hakbong Lee

Department of Biological Sciences

Ulsan National Institute of Science and Technology

2022

Structural study for mitochondrial quality control

Hakbong Lee

Department of Biological Sciences

Ulsan National Institute of Science and Technology

Structural study for mitochondrial quality control

A thesis/dissertation submitted to
Ulsan National Institute of Science and Technology
in partial fulfillment of the
requirements for the degree of
Doctor of Philosophy

Hakbong Lee

11.17.2021 of submission

Approved by

Advisor
Changwook Lee

Structural study for mitochondrial quality control

Hakbong Lee

This certifies that the thesis/dissertation of Hakbong Lee is approved.

11.17.2021 of submission

Advisor: Changwook Lee

Byoung Heon Kang

Young Chan Chae

Eunhee Kim

Cheol-Min Park

Abstract

Mitochondria are essential multifunctional organelles that produce the energy of cell, synthesize macromolecules and regulate cell death. They produce ATP using oxygen and nutrients from food by oxidative metabolism. In addition to ATP production, intermediates in energy metabolism of mitochondria are utilized to metabolites for biosynthesis, metabolic homeostasis, signal transduction, and protein modification. Maintenance of healthy mitochondria is important for cells. For quality control of mitochondria, Cells respond to damage and dysfunction of mitochondria through a selective autophagy pathway called mitophagy. Mitophagy degrades damaged mitochondria under various environmental stresses and oxidative stress. Recently, NIPSNAP1 and NIPSNAP2, mitochondrial proteins, participate in mitophagy mechanism as a new player of Parkin-dependent mitophagy initiation. When mitochondria are depolarized by oxidative stress and mitochondria dysfunction, NIPSNAP1 and NIPSNAP2 are accumulated in mitochondrial outer membrane and play a role as ‘‘eat me’’ signals. They recruit autophagy receptors, which promote the autophagosomal machinery. In this study, we report the purification, crystallization and preliminary X-ray diffraction analysis of recombinant human NIPSNAP1 and NIPSNAP2 for characterization and identification at the molecular level.

Mitochondria are also involved in cancer cell. Heat shock protein 90 (Hsp90) family proteins are molecular chaperones that modulate the functions of various substrate proteins implicated in pro-tumorigenic pathways. In this study, the mitochondria-targeted antioxidant mitoquinone (MitoQ) was identified as a potent inhibitor of mitochondrial Hsp90, known as tumor necrosis factor receptor-associated protein 1 (TRAP1). Structural analyses revealed an asymmetric bipartite interaction between MitoQ and the previously unrecognized drug binding sites located in the middle domain (MD) of TRAP1, believed to be a client binding region. MitoQ effectively competed with TRAP1 clients, and MitoQ treatment facilitated the identification of 103 TRAP1-interacting mitochondrial proteins in cancer cells. MitoQ and its redox-crippled SB-U014/SB-U015 exhibited more potent anticancer activity in vitro and in vivo than previously reported mitochondria-targeted TRAP1 inhibitors. The findings indicate that targeting the client binding site of Hsp90 family proteins offers a novel strategy for the development of potent anticancer drugs.

Additionally, this study reports the implication of neurological disorder Kohlschutter-Tönz syndrome (KTS) by human protein Rogdi. KTS is a rare autosomal-recessive disorder of childhood onset characterized by global developmental delay, spasticity, epilepsy, and amelogenesis imperfecta. Rogdi is an essential protein that is highly conserved across metazoans, and mutations have been implicated as the genetic cause of KTS. Although genetic causes for KTS patients are relatively well established, the molecular basis of how the specific mutations abolish its physiological functions and cause KTS

has not yet been elucidated. To gain structural insight into Rogdi mutants and their relationship with KTS, we determined the crystal structure of human Rogdi protein at atomic resolution. Rogdi forms a novel elongated curved structure comprising the α domain, a leucine-zipper-like four-helix bundle, and a characteristic β-sheet domain. Especially within α domain, the N-terminal H1 helix (residues 19–45) pairs with the C-terminal H6 helix (residues 252–287) in an antiparallel manner, indicating that the integrity of the four-helix bundle requires both N- and C-terminal residues. The crystal structure, in conjunction with biochemical data, indicates that the α domain might undergo a conformational change and provide a structural platform for protein–protein interactions. Disruption of the four-helix bundle by mutation results significant destabilization of the structure. Through this structural and biochemical study, we provide structural insight into the link between mutations in Rogdi and the causes of KTS. This fundamental knowledge could assist the development of pharmaceutical agents for the treatment and cure of this debilitating neurological disease.

Contents

List of Figures

List of tables

Abbreviations

AMPPNP : Adenylyl-imidodiphosphate

ATP : adenosine triphosphate

AUC : Analytical ultracentrifugation

CD : Circular dichroism

CTD : C-termical domain

DISC1 : Disrupted-In-Schizophrenia-1

Hsp90 : Heat shock protein 90

KTS : Kohlschutter-Tönz syndrome

LMD : Large middle domain

MD : Middle domain

MitoQ : Mitoquinone

MTS : mitochondrial targeting sequence

NIPSNAP : nitrophenylphosphatase domain and non-neuronal SNAP25-like protein homolog

NTD : N-terminal domain

PINK1 : PTEN-induced putative kinase 1

RMSD : root mean square deviation

SAD : Single-wavelength anomalous dispersion

Se-Met : Selenomethionine

SMD : Small middle domain

TPP : mitochondria-targeting triphenylphosphonium

TRAP1 : Tumor necrosis factor receptor-associated protein 1

Ub : ubiquinone

Chapter 1. Crystallization and preliminary X-ray diffraction analysis of human protein NIPSNAP1 and NIPSNAP2.

1.1. Abstracts

Mitochondria are essential multifunctional organelles that produce the energy of cell, synthesize macromolecules and regulate cell death. They produce ATP using oxygen and nutrients from food by oxidative metabolism. In addition to ATP production, intermediates in energy metabolism of mitochondria are utilized to metabolites for biosynthesis, metabolic homeostasis, signal transduction, and protein modification. Maintenance of healthy mitochondria is important for cells. For Quality control of mitochondria, Cells respond to damage and dysfunction of mitochondria through a selective autophagy pathway called mitophagy. Mitophagy degrades damaged mitochondria under various environmental stresses and oxidative stress. Recently, NIPSNAP1 and NIPSNAP2, mitochondrial proteins, participate in mitophagy mechanism as a new player of Parkin-dependent mitophagy initiation. When mitochondria are depolarized by oxidative stress and mitochondria dysfunction, NIPSNAP1 and NIPSNAP2 are accumulated in mitochondrial outer membrane and play a role as ‘‘eat-me’’ signals. They recruit autophagy receptors, which promote the autophagosomal machinery. In this study, we report the purification, crystallization and preliminary X-ray diffraction analysis of recombinant human NIPSNAP1 and NIPSNAP2 for characterization and identification at the molecular level.

1.2. Introduction

Mitochondria are a significant organelle in eukaryotic cell. They produce most of the required energy using oxidative phosphorylation (OXPHOS) carried out by the electron transport chain and supply the ATP to the cell for various metabolism. Mitochondria operate metabolic pathway to generate the energy. Many metabolites, derived from the mitochondrial metabolic pathway, participate in cell signaling pathway, biosynthesis, and protein modifications[1]. Mitochondrial dysfunction, impaired by environmental stress, is implicated in many disease such as neurodegeneration, cancer, epilepsy, autism, and inflammation[2].

Mitochondrial autophagy (Mitophagy) is important for maintaining cellular homeostasis, removing damaged mitochondria by mitochondrial dysfunction. In mitophagy, the E3 ubiquitin ligase Parkin and PTEN-induced putative kinase 1 (PINK1) are essential proteins. In normal mitochondria, PINK1 is eliminated by E3 ubiquitin ligases UBR1, UBR2 and UBR4 in the N-end rule pathway. On the other hand, depolarization of mitochondria induces the accumulation of PINK1 in mitochondrial outer membrane. The stabilized PINK1 activate Parkin through phosphorylation. The activated PINK1 and Parkin promote ubiquitination and phosphorylation of Mitochondrial outer membrane proteins[3-6]. It recruits autophagy receptors[7], and allows the formation of autophagosome.

Recently, the nitrophenylphosphatase domain and non-neuronal SNAP25-like protein homolog 1 and 2 (NIPSNAP 1 and 2) are identified a key protein of the mitophagy process[8]. NIPSNAP1 and NIPSNAP2 have two N-terminal mitochondrial targeting sequence (MTS). In healthy mitochondria, they are localized in mitochondrial matrix by first MTS. However, their function is not elucidated yet. Upon depolarization of mitochondria by environmental stress, NIPSNAP1 and NIPSNAP2 are accumulated in mitochondrial outer membrane. They interact with key member of parkin-dependent mitophagy such as Parkin, autophagy receptor, LC3, and ATG8 family proteins, and form a atophagosome. In zebrafish model, The deficiency of NIPSNAP1 reduced mitophagy turnover and showed parkinsonism. In this study, we report the purification and preliminary X-ray crystallographic analysis of NIPSNAP1 and NIPSNAP2, providing insight into their function.

1.3. Results and discussion

1.3.1. NIPSNAP1 and NIPSNAP2 form oligomeric state.

The human NIPSNAP1 and NIPSNAP2 consists of 284 and 286 amino acids, respectively. NIPSNAP1 have 67.7% identity compared to and NIPSNAP2. Their N-terminus sequences are recognized as mitochondrial targeting sequence (MTS) (Figure 1.1.A). N-terminal MTS regions are predicted that they have no secondary structure. To obtain soluble protein and crystals, we constructed truncated sequence of NIPSNAP1 (68-284) and NIPSNAP2 (70-286). They were expressed with His_6-tagged proteins at the N-terminus and purified to a series of chromatography. We performed size-exclusion chromatography as a final purification step to obtain homogeneous NIPSNAP1 and NIPSNAP2. The proteins were eluted at a volume of the oligomeric molecular size. The purity of proteins was at least 95% as monitored by SDS–PAGE and protein. Additionally, we purified the NIPSNAP1 substituted methionine to selenomethionine for phasing. For successful crystallization, we performed a limited proteolysis (Figure 1.1.B). The limited proteolysis result suggested that the purified NIPSNAP1 and NIPSNAP2 are compact.

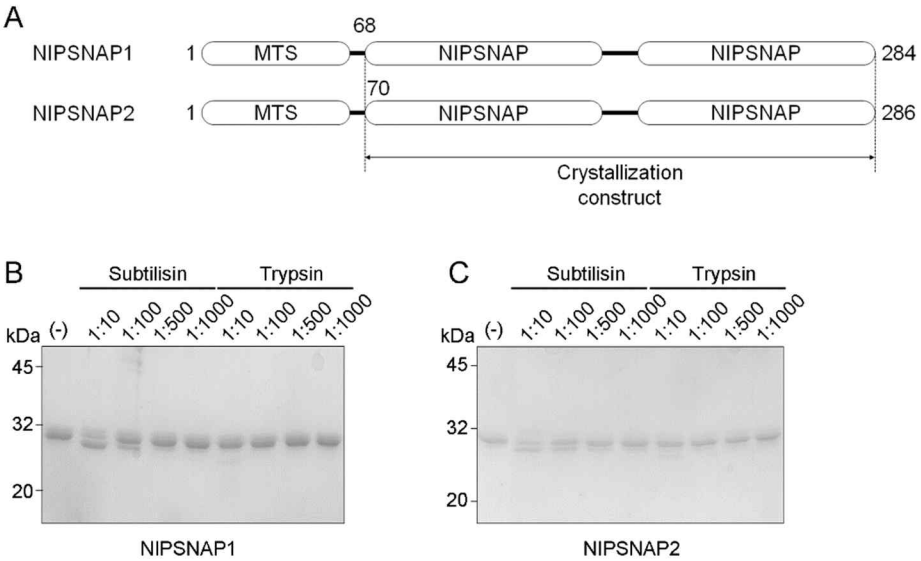

Figure 1.1. Crystallization constructs of NIPSNAP1 and NIPSNAP2.

(A) Domain structures of NIPSNAP1 and NIPSNAP2 are shown as a Diagram. (B, C) limited proteolysis of NIPSNAP1 and NIPSNAP2.

1.3.2. NIPSNAP1/2 crystals improvement and X-ray diffraction.

Crystals of NIPSNAP1 were initially obtained in a crystallization condition consisting of 1.4M Na-malonate pH 8.0. We finally improved the condition to 1.4M Na-malonate pH 8.3, 100mM KCl (Figure 1.2.A). NIPSNAP1 with selenomethionine was crystallized in the different condition to 1.4M Na-malonate pH 8.0, 80mM KCl, 2% Acetone (Figure 1.2.B). Although NIPSNAP2 is highly conserved with NIPSNAP1, NIPSNAP2 crystallization is different. The initial crystallization condition of NIPSNAP2 was 1.8M K/Na phosphate pH 5.0. Final condition was 1.7M K/Na phosphate pH 5.1, 2% PEG 5K MME (Figure 1.2.C). In order to collect X-ray diffraction data, all crystals were cryo-cooled using cryo-protection solution consisting of crystallization solution with 30% glycerol. We collected X-ray diffraction data on beamline 7A at PAL. Native NIPSNAP1 was diffracted to a maximum of 2.8 Å resolution (Figure 1.3.A), and NIPSNAP1 with selenium was diffracted to 2.4 Å resolution (Figure 1.3.B). NIPSNAP2 was diffracted to 1.9 Å (Figure 1.3.C). The Native and Selenomethionine NIPSNAP1 belonged to space group $C222_1$, with unit-cell parameters a = b = 95.8 Å, c = 108.9 Å, assuming the presence of four molecules per asymmetric unit, the Matthews coefficient (V_M) was estimated to be 2.89 $Å^3\ Da^{-1}$, with a solvent content of 57.5%. NIPSNAP2 belonged to space group $P42_12$, with. the V_M was estimated to be 2.08 $Å^3\ Da^{-1}$, with a solvent content of 40.9%. We are attempt to solve the phase problem using SAD phasing and molecular displacement.

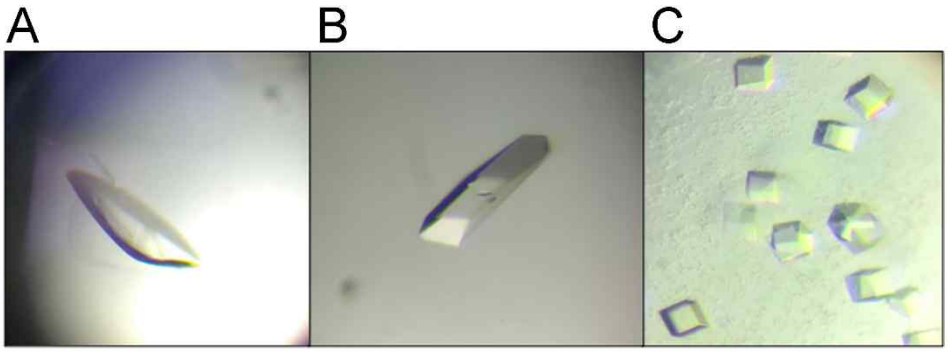

Figure 1.2. Crystals of human NIPSNAP1 and NIPSNAP2.

(A) Crystals of native NIPSNAP1 (68-284) crystallized in condition of 1.4M Na-malonate pH 8.3. (B) Crystals of selenomethionine-substituted NIPSNAP1 (68-284) grown in 1.4M Na-malonate pH 8.0, 80mM KCl, 2% Acetone. (C) crystals of native NIPSNAP2 (70-286) in 1.7M K/Na phosphate pH 5.1, 2% PEG 5K MME.

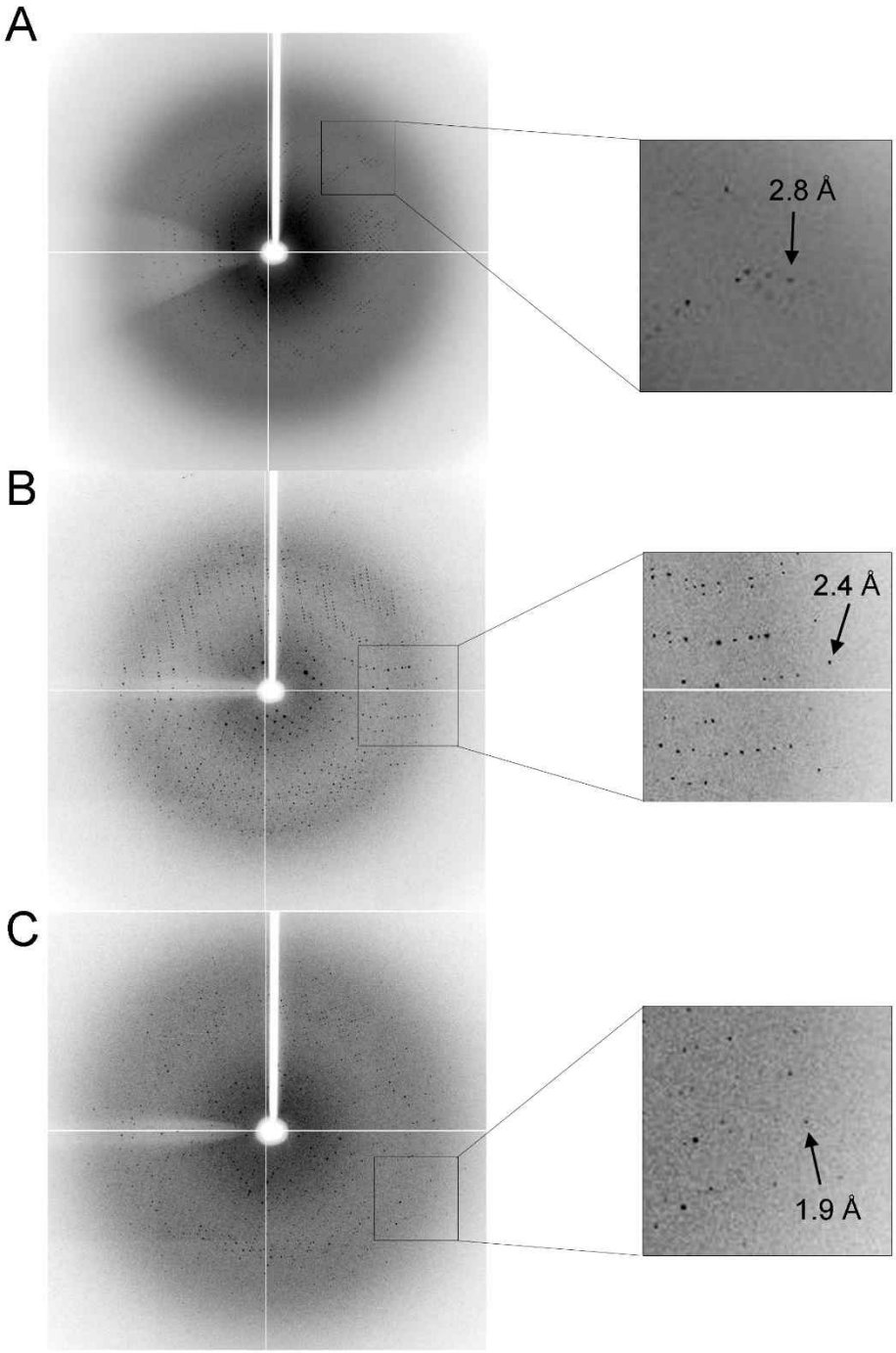

Figure 1.3. X-ray diffraction images.

X-ray diffraction patterns collected from a single crystal of (A) native NIPSNAP1 (68-284), (B) Selenomethionine-substituted NIPSNAP1 (68-284), and (C) native NIPSNAP2 (70-286). The diffraction images were obtained using a synchrotron radiation source. The maximum observed resolution is 2.8 Å, 2.4 Å, and 1.9 Å, respectively.

1.4. Materials and methods

1.4.1. Protein Production.

The human gene encoding NIPSNAP1 (68-284) and NIPSNAP2 (70-286) proteins excluding the N-terminal mitochondrial targeting sequence were amplified by PCR and cloned into a modified pET-Duet vector including an N-terminal histidine tag and a TEV proease cleavage site. For protein production, the plasmids encoding NIPSNAP1 and NIPSNAP2 were transformed into *Escherichia coli* strain BL21 (DE3) cells with extra chaperon plasimid, respectively. Each cells grew at 37 ºC up to an OD_{600} 0.6 using fresh LB medium containing ampicillin (50 μg/ml). After cooled to 18 ºC, cells were induced by 0.25 mM isopropyl β-D-1-thiogalactopyranoside (IPTG) for protein expression. Cells were harvested by centrifugation at 10,000g for 15 min after 18 hours post induction, and the pellet was resuspended in a lysis buffer (25 mM sodium phosphate pH 7.8, 400 mM sodium chloride, and 10 mM imidazole). The cells were lysed by sonication and the laysed cells were clarified using centrifugation at 32,000g for 60 min. After centrifugation, the supernatant was loded onto an Ni^{2+}-IMAC affinity column (GE Healthcare) equilibrated with binding buffer (25 mM sodium phosphate pH 7.8, 400 mM NaCl, and 10 mM imidazole). After washing the column with washing buffer (25 mM sodium phosphate pH 7.8, 400 mM NaCl, and 50 mM imidazole), The bound proteins were eluted with elution buffer (25 mM sodium phosphate pH 7.8, 300 mM NaCl, and 400 mM imidazole). The eluted proteins were purified with a Superdex 200 HR 16/60 gel-filtration column (GE Healthcare) equilibrated with buffer consisting of 25 mM Tris pH 7.5, 150 mM sodium chloride, 5 mM DTT. The eluted homogenous NISPANP1 and NIPSNAP2 proteins were fanally concentrated to 20 mg per ml using an Amicon Ultra-15 centrifugal filter (30 kDa molecular-weight cutoff, Millipore) and flash-frozen in liquid nitrogen for storage. All purification steps were carried out at 277 K and were monitored by SDS–PAGE. Selenomethionine-substituted NIPSNAP1 was expressed in *E. coli* B834 (DE3) cells (Novagen) using M9 minimal medium plus selenomethionine. Purification steps were identical to native proteins purification steps.

1.4.2. Crystallization.

Initial crystallization screening was performed using crystallization robot Mosquito (STP labtech) at both 277 and 293 K by the sitting-drop vapour-diffusion method commercially available screening solutions including Structure Screen 1 and 2 (Molecular Dimensions), (Hampton Research), Wizard 1 and 2 (Emerald Bio), MIDAS 1 and 2 (Molecular Dimensions), and Grid screens. Crystallization drops

were prepared by mixing 0.2 μl of a 20 mg per ml protein solution in buffer (25 mM Tris, 150 mM NaCl, 5 mM DTT pH 7.5) and 0.2 μl well solution. The obtained initial crystals were optimized by varying the protein concentration, the precipitant concentration and the pH and by using Additive Screen (Hampton Research).

1.4.3. Data collection and processing.

For X-ray diffraction studies, crystals were transferred to a cryoprotectant solution comprising reservoir buffer plus 30% glycerol and flash-frozen in liquid nitrogen. X-ray diffraction data were collected at beamline 7A of Pohang Accelerator Laboratory (PAL). X-ray diffraction data were processed with HKL-2000[9]. SAD data analysis was performed using Phenix[10]. The data-collection statistics are summarized in Table 1.1.

1.4.4. Limited Proteolysis.

Limited proteolysis experiments were carried out to define compact domain of protein. Purified recombinant NIPSNAP1 and NIPSNAP2 were digested with trypsin and subtilisin using a series of protein concentrations and incubation times at 4 °C. The reaction was stopped with 1 mM PMSF, and products were analyzed by SDS-PAGE.

Table 1.1. Data Collection and Refinement Statistics.

	hNIPSNAP1-native	hNIPSNAP1-SeMet	hNIPSNAP2
X-ray source	Beamline 7A, PAL	Beamline 7A, PAL	Beamline 7A, PAL
Temperature (K)	100	100	100
Space group:	$C222_1$	$C222_1$	$P42_12$
Cell parameters			
a, b, c (Å)	140.858.145.000.135.	140.858.145.000.135.	95.780, 95.780,
α, β, γ (°)	85	85	108.850
	90.000, 90.000, 90.00(	90.000, 90.000,	90.000, 90.000,
		90.000	90.000
Data processing			
Wavelength (Å)	0.97934	0.97934	0.97934
Resolution (Å)	50.00 - 2.80	50.00 - 2.40	50.00 – 1.90
R_{merge} (%)	6.8 (42.7)	9.6 (62.9)	5.8 (38.4)
I/σ	15.0 (2.1)	31.0 (2.5)	18.0 (4.6)
Completeness (%)	98.9 (94.2)	97.5 (93.9)	99.8 (97.6)
Redundancy	4.8 (3.3)	5.9 (3.9)	4.3 (3.1)
Measured reflections	378974	385474	137098
Unique reflections	73687	69287	50192

*Highest resolution shell is shown in parenthesis.

1.5. Reference

1. McBride, H. M.; Neuspiel, M.; Wasiak, S., Mitochondria: more than just a powerhouse. *Current biology : CB* **2006,** *16* (14), R551-60.

2. Lin, M. T.; Beal, M. F., Mitochondrial dysfunction and oxidative stress in neurodegenerative diseases. *Nature* **2006,** *443* (7113), 787-95.

3. Kondapalli, C.; Kazlauskaite, A.; Zhang, N.; Woodroof, H. I.; Campbell, D. G.; Gourlay, R.; Burchell, L.; Walden, H.; Macartney, T. J.; Deak, M.; Knebel, A.; Alessi, D. R.; Muqit, M. M., PINK1 is activated by mitochondrial membrane potential depolarization and stimulates Parkin E3 ligase activity by phosphorylating Serine 65. *Open biology* **2012,** *2* (5), 120080.

4. Kane, L. A.; Lazarou, M.; Fogel, A. I.; Li, Y.; Yamano, K.; Sarraf, S. A.; Banerjee, S.; Youle, R. J., PINK1 phosphorylates ubiquitin to activate Parkin E3 ubiquitin ligase activity. *Journal of Cell Biology* **2014,** *205* (2), 143-153.

5. Kazlauskaite, A.; Kondapalli, C.; Gourlay, R.; Campbell, David G.; Ritorto, Maria S.; Hofmann, K.; Alessi, Dario R.; Knebel, A.; Trost, M.; Muqit, Miratul M. K., Parkin is activated by PINK1-dependent phosphorylation of ubiquitin at Ser65. *Biochemical Journal* **2014,** *460* (1), 127-141.

6. Koyano, F.; Okatsu, K.; Kosako, H.; Tamura, Y.; Go, E.; Kimura, M.; Kimura, Y.; Tsuchiya, H.; Yoshihara, H.; Hirokawa, T.; Endo, T.; Fon, E. A.; Trempe, J. F.; Saeki, Y.; Tanaka, K.; Matsuda, N., Ubiquitin is phosphorylated by PINK1 to activate parkin. *Nature* **2014,** *510* (7503), 162-6.

7. Lazarou, M.; Sliter, D. A.; Kane, L. A.; Sarraf, S. A.; Wang, C.; Burman, J. L.; Sideris, D. P.; Fogel, A. I.; Youle, R. J., The ubiquitin kinase PINK1 recruits autophagy receptors to induce mitophagy. *Nature* **2015,** *524* (7565), 309-314.

8. Princely Abudu, Y.; Pankiv, S.; Mathai, B. J.; Håkon Lystad, A.; Bindesbøll, C.; Brenne, H. B.; Yoke Wui Ng, M.; Thiede, B.; Yamamoto, A.; Mutugi Nthiga, T.; Lamark, T.; Esguerra, C. V.; Johansen, T.; Simonsen, A., NIPSNAP1 and NIPSNAP2 Act as "Eat Me" Signals for Mitophagy. *Developmental cell* **2019,** *49* (4), 509-525.e12.

9. Otwinowski, Z.; Minor, W., Processing of X-ray diffraction data collected in oscillation mode. *Method Enzymol* **1997,** *276*, 307-326.

10. Adams, P. D.; Afonine, P. V.; Bunkoczi, G.; Chen, V. B.; Davis, I. W.; Echols, N.; Headd, J. J.; Hung, L. W.; Kapral, G. J.; Grosse-Kunstleve, R. W.; McCoy, A. J.; Moriarty, N. W.; Oeffner, R.; Read, R. J.; Richardson, D. C.; Richardson, J. S.; Terwilliger, T. C.;

Zwart, P. H., PHENIX: a comprehensive Python-based system for macromolecular structure solution. *Acta Crystallogr D Biol Crystallogr* **2010,** *66* (Pt 2), 213-21.

Chapter 2. Mitoquinone inactivates mitochondrial chaperone TRAP1 by blocking the clien binding site.

(Original article : Yoon NG, Lee H, Kim SY, Hu S, Kim D, Yang S, Hong KB, Lee JH, Kang S, Kim BG, Myung K, Lee C, Kang BH. Mitoquinone Inactivates Mitochondrial Chaperone TRAP1 by Blocking the Client Binding Site. *J Am Chem Soc.* 2021 Dec 1;143(47):19684-19696.)

2.1. Abstract

Heat shock protein 90 (Hsp90) family proteins are molecular chaperones that modulate the functions of various substrate proteins (clients) implicated in pro-tumorigenic pathways. In this study, the mitochondria-targeted antioxidant mitoquinone (MitoQ) was identified as a potent inhibitor of mitochondrial Hsp90, known as tumor necrosis factor receptor-associated protein 1 (TRAP1). Structural analyses revealed an asymmetric bipartite interaction between MitoQ and the previously unrecognized drug binding sites located in the middle domain (MD) of TRAP1, believed to be a client binding region. MitoQ effectively competed with TRAP1 clients, and MitoQ treatment facilitated the identification of 103 TRAP1-interacting mitochondrial proteins in cancer cells. MitoQ and its redox-crippled SB-U014/SB-U015 exhibited more potent anticancer activity in vitro and in vivo than previously reported mitochondria-targeted TRAP1 inhibitors. The findings indicate that targeting the client binding site of Hsp90 family proteins offers a novel strategy for the development of potent anticancer drugs.

2.2. Introduction

Heat shock protein 90 (Hsp90) family proteins are highly conserved ATP-dependent molecular chaperones supporting the stability and activity of structurally labile substrate proteins, also known as clients, which are often related to tumorigenesis.[1-2] Expressed in subcellular compartments, Hsp90 family proteins regulate organelle-specific populations of client proteins. For example, Hsp90 supports the functions of many mutated or overexpressed oncoproteins located in the cytoplasm and nucleus, including various kinases, steroid hormone receptors, and transcription factors.[3] Meanwhile, tumor necrosis factor (TNF) receptor-associated protein 1 (TRAP1), a mitochondrial Hsp90 paralog, reprograms cellular metabolic and signaling pathways by altering the functions of various mitochondrial matrix and inner membrane proteins in cancer cells.[4-7] Consequently, Hsp90 family proteins allow cancer cells to adapt to a variety of cellular stresses in rapidly growing tumors, and subsequently to evolve into more aggressive tumors.[1, 8] Thus, Hsp90 family proteins have been proposed as promising targets for the development of potent cancer therapeutics.[9-10]

Several small molecule inhibitors targeting the ATP binding site of Hsp90 have been developed and have already entered clinical evaluation.[3, 11] Due to structural similarity, many Hsp90 inhibitors display cross-reactivity with TRAP1 in vitro.[12-14] However, in contrast to the in vitro activity, most Hsp90 inhibitors cannot inactivate TRAP1 in vivo, likely due to insufficient accumulation of the drug inside mitochondria.[15-17] To overcome this limitation of the cellular drug distribution and to efficiently inactivate TRAP1, several inhibitors with improved mitochondrial accumulation have been developed by conjugating a mitochondria-targeting triphenylphosphonium (TPP) moiety. This approach successfully converted cytoplasmic Hsp90 inhibitors (moderate activity) to mitochondria-accumulating TRAP1 inhibitors (potent cytotoxic activity). Examples include gamitrinib, SMTIN-P01, and SMTIN-C10.[15, 17-20]

In addition to the ATP binding site, Hsp90 family proteins possess other druggable sites, including the putative ATP binding site in the C-terminal domain (CTD),[13] and the client binding site in the middle domain (MD). Unlike the putative ATP binding site, inhibitor development targeting the client binding site has been relatively unexplored. In the present study, we identified the mitochondria-targeted antioxidant, mitoquinone (MitoQ), as a potent TRAP1 inhibitor that interacts with the client binding site in MD. The molecular interaction between TRAP1 and MitoQ was confirmed and analyzed by X-ray crystallography. MitoQ blocked client interaction with TRAP1 and consequently achieved stronger anticancer activity in vivo than previously reported TRAP1 inhibitors.

2.3 Results

2.3.1. TPP with a long alkyl chain inhibits TRAP1 chaperone activity

We recently reported that the TPP moiety of the mitochondria-targeted TRAP1 inhibitor SMTIN-C10 can interact with a potential allosteric site, triggering conformational changes in TRAP1 and elevating its ATPase activity.[20] Thus, in the present work, we explored the effects of several alkyl (methyl to hexadecyl) TPPs (TPP-1 - TPP-16, respectively; Figure 2.1.A) on the ATPase activity of TRAP1. TPP-1, -2, -4, -6, and -8 marginally increased the ATPase activity of purified recombinant TRAP1, up to 1.5 fold (Figure 2.1.B). Meanwhile, TPP-10 and -12 caused a dramatic elevation in ATPase activity, by 2.3 fold in the case of TPP-10 (at 20 μM), and by 2.4 fold in the case of TPP-12 (ATPase activity was saturated at ~10 μM) (Figure 2.1.B). TPP molecules with the longest alkyl chains (TPP-14 and -16) caused a 2.4 fold elevation in ATPase activity at 5 μM and 2 μM, respectively, and a further increase in drug concentration resulted in complete inhibition of the ATPase activity at 15 μM and 10 μM, respectively (Figure 2.1.B). TPP-16 at concentrations >2 μM increased aggregation of TRAP1 in chemical cross-linking experiments (Figure 2.2.A), and the two longest alkyl chain TPPs, but not PU-H71 (an Hsp90/TRAP1 inhibitor targeting the ATP binding site) appeared to trigger dramatic conformational changes in TRAP1 at high drug concentrations, resulting in aggregation-sensitive structures and leading to consequent inhibition of the ATPase activity (Figure 2.1.B). None of the alkyl TPPs interacted with the ATP binding site, based on a lack of competition with FITC-labeled PU-H71 (Figure 2.1.C).[16]

To examine TRAP1 inhibition, the 22Rv1 prostate cancer cell was treated with each alkyl TPP to analyze degradation of TRAP1 client proteins, succinate dehydrogenase B (SDHB) and sirtuin-3 (SIRT3).6 Long alkyl TPPs (TPP-10 - 16) inhibited TRAP1 based on degradation of client proteins (Figure 2.1.D), and TPP-14 and -16 were the most potent inhibitors. However, none inhibited cytoplasmic Hsp90 (Figure 2.1.D), since there were no changes in the expression of Hsp90 client proteins (Akt and Cdk4) or a pharmacodynamic marker of Hsp90 inhibition (Hsp70).[21] Thus, the long alkyl TPPs were able to inhibit the chaperone activity of TRAP1, probably through allosteric modulation triggering conformational changes, without direct interaction with the ATP binding site.

2.3.2. TRAP1 inhibitory activity of TPP-conjugates

Various antioxidants have been conjugated with the TPP moiety to deliver them effectively to mitochondria, the major reactive oxygen species (ROS)-producing cellular organelle.[22-23] Thus, to identify small molecules targeting the allosteric site of TRAP1, we examined TPP-conjugated

antioxidants (Figure 2.1.E-F), including mitoquinone (MitoQ) and visomitin (SkQ1), both approved for human application.[24-25] TPP-antioxidant conjugates with long linkers (≥C10; MitoQ, Mito-CP, and SkQ1; Figure 2.1.E) increased ATPase activity by 2.4 fold, 2.6 fold, and 2.5 fold compared with controls. By comparison, those with short hydrocarbon linkers, namely Mito-TEMPO and Mito-VitE (Figure 2.1.F), increased TRAP1 ATPase activity by no more than 1.3 fold (Figure 2.1.G). None of the antioxidants interacted with the ATP binding site in TRAP1 (Figure 2.1.H). Consistent with the drug effects on ATPase activity, long linker TPP-antioxidants reduced expression of TRAP1 client proteins without inhibition of Hsp90 in 22Rv1 cells (Figure 2.1.I), while short linker-TPPs did not affect expression of these proteins (Figure 2.1.J).

At the molecular level, MitoQ, a potent TPP-antioxidant and TRAP1 inhibitor, did not induce TRAP1 aggregation at 37°C, in contrast to TPP-16 (Figure 2.2.A), which could explain why MitoQ did not reduce the ATPase activity of TRAP1 at high drug concentrations. Interestingly, however, at high temperature, MitoQ also increased TRAP1 oligomerization and made it prone to aggregation (Figure 2.2.B-D). The thermal aggregation properties were further exploited to examine cellular conformation changes of TRAP1, and long linker-TPPs (MitoQ, Mito-CP, and SkQ1) strongly induced aggregation, whereas short linker-TPPs (Mito-TEMPO and Mito-VitE) did not induce TRAP1 thermal aggregation in 22Rv1 cells (Figure 2.2.E). These results indicate that the mode of action of long linker-TPPs is closely related to the conformational transition of TRAP1, which is not the case with the orthosteric inhibitor PU-H71 (Figure 2.2.D)

Among alkyl TPPs and TPP-antioxidants examined in this study, MitoQ most potently induced degradation of client proteins and TRAP1 thermal aggregation in cancer cells (Figures 2.1.D, 2.1.I, and 2.2.E), and recorded the highest cancer-specific cytotoxic activity (Table 2.1). Thus, in subsequent studies, we chose MitoQ and further analyzed this novel allosteric TRAP1 inhibitor.

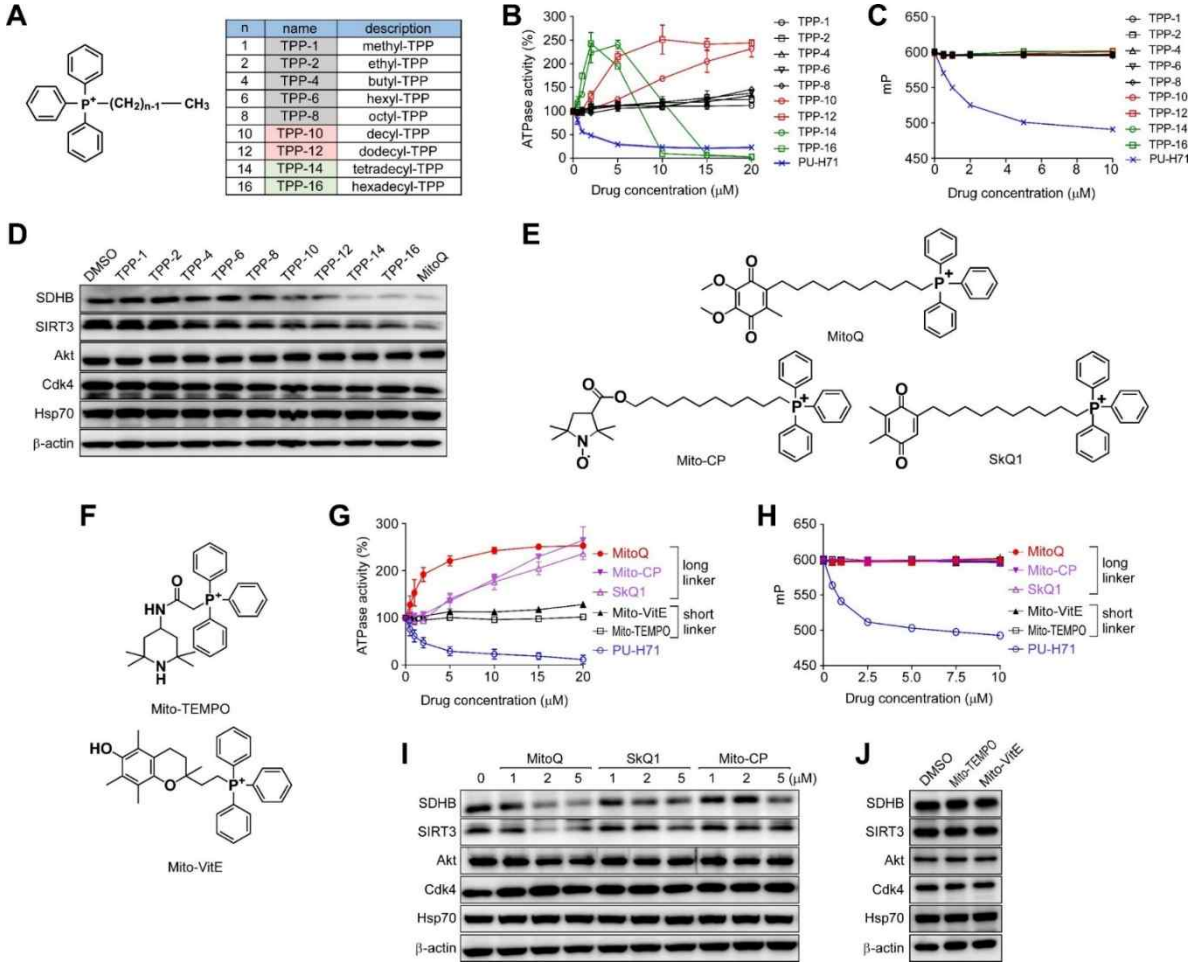

Figure 2.1. Effects of alkyl TPPs and TPP-conjugated antioxidants on TRAP1.

(A) Chemical structures of alkyl TPPs with various chain lengths. Methyl-hexadecyl TPPs are named TPP-1-TPP-16, respectively. (B) Activation of TRAP1 ATPase activity. ATP hydrolysis by human TRAP1 (hTRAP1) was measured in the presence of alkyl TPPs as indicated. (C) Binding affinity of alkyl TPPs to the ATP binding pocket of TRAP1. hTRAP1 was incubated with alkyl TPPs in the presence of PU-H71-FITC320 and analyzed by fluorescence polarization. mP, millipolarization. (D) Inhibition of TRAP1 and Hsp90 in a cancer cell. 22Rv1 cells were incubated with 5 μM drugs as indicated and analyzed by western blotting. (E) Chemical structures of TPP-antioxidants with a long hydrocarbon linker. (F) Chemical structures of TPP-antioxidants with a short hydrocarbon linker. (G) TRAP1 ATPase activity. ATP hydrolytic activity of hTRAP1 was measured in the presence of drugs as indicated. (H) Drug interactions with the ATP binding pocket of hTRAP1. (I) Cellular effects of long linker TPP-antioxidants. 22Rv1 cells were incubated with drugs as indicated for 2 h and analyzed by western blotting. (J) Cellular effects of short linker TPP-antioxidants. The effects of drugs at 5 μM concentration were analyzed as in (I). Data (n = 4-6) in (B), (C), (G), and (H) are mean ± standard error of the mean (SEM) from two independent experiments.

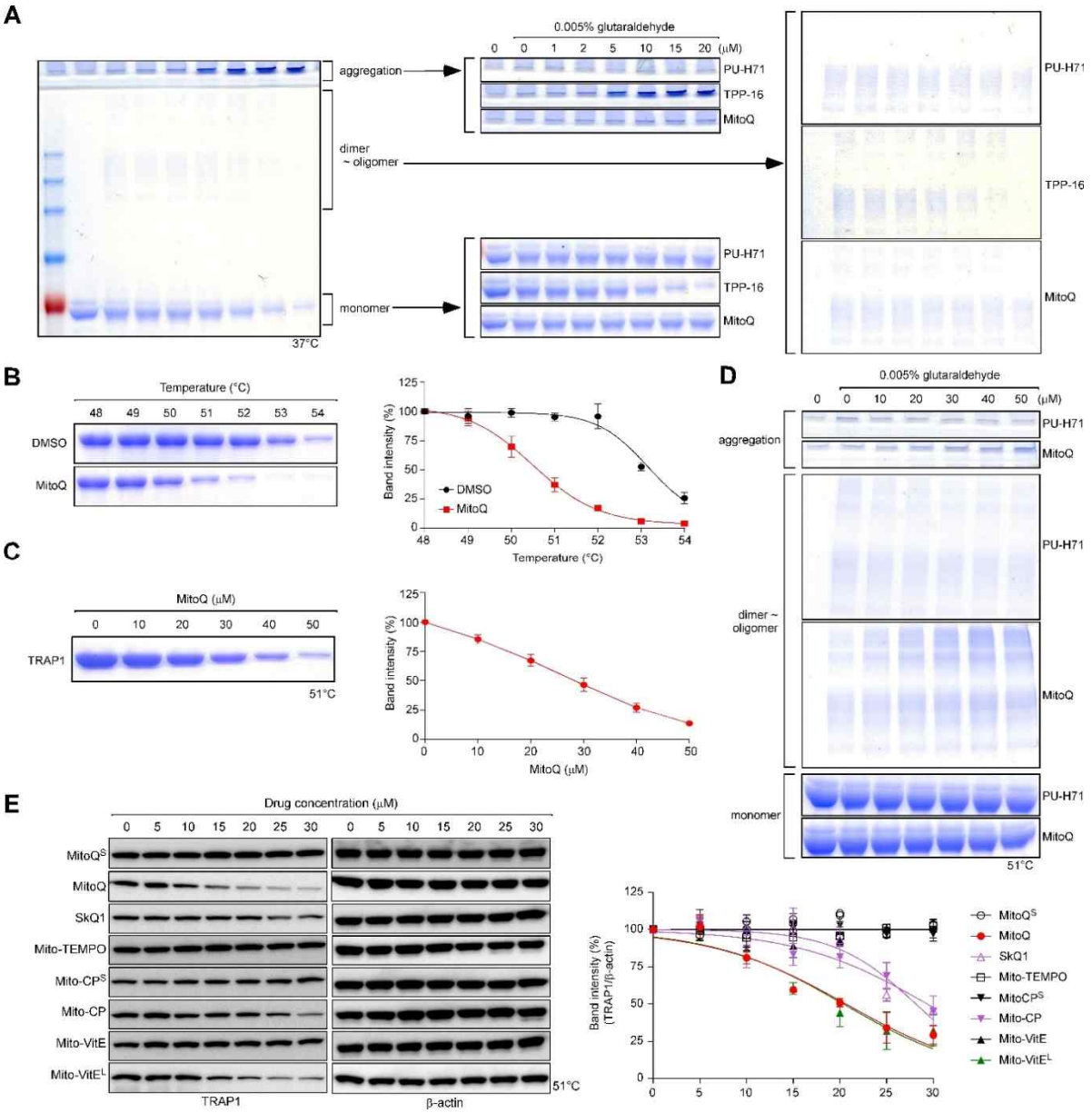

Figure 2.2. Drug-induced aggregation and thermal denaturation of TRAP1.

(A) Analysis of TRAP1 oligomerization and aggregation. Purified human TRAP1 (hTRAP1) was incubated with drugs as indicated for 3 h at 37 ºC. Drug-treated proteins were cross-linked for 5 min at 4 ºC with 0.005% glutaraldehyde and analyzed by SDS-PAGE and Coomassie staining. Aggregated proteins (remaining on the top of the stacking gel) and oligomers/monomers in the separating gel were compared. PU-H71 and MitoQ treatment yielded monomer/dimer bands without formation oligomers/aggregates; meanwhile, TPP-16 induced oligomer/aggregate formation and reduced the amount of monomer/dimer. (B) Thermal denaturation of TRAP1. Purified hTRAP1 was heat-denatured for 5 min in the presence of MitoQ (50 μM), and soluble proteins were analyzed by SDS-PAGE (left). Quantification of Coomassie-stained band intensity is shown on the right. At around 51-52 ºC, MitoQ induced thermal denaturation of TRAP1 most potently compared with DMSO controls, which could be related to MitoQ-induced conformational changes. (C) MitoQ induction of TRAP1 thermal denaturation. Purified hTRAP1 was incubated with MitoQ as indicated for 5 min at 51 ºC, and soluble proteins were analyzed by SDS-PAGE (left). Quantification of Coomassie-stained band intensity is shown on the right. MitoQ reduced the amount of soluble TRAP1 protein in a dose-dependent manner, indicating dose-dependent thermal denaturation at 51 ºC. (D) Chemical cross-linking after thermal denaturation. Purified hTRAP1 was incubated with MitoQ as indicated for 5 min at 51 ºC and then cross-linked for 5 min at 4 ºC with 0.005% glutaraldehyde. Cross-linked proteins were analyzed by SDS-PAGE and Coomassie staining. Conformational changes caused by MitoQ could lead to aggregation of TRAP1 at 51 ºC; meanwhile, PU-H71 did not affect TRAP1 thermal aggregation. (E) Drug-induced changes in thermal stability of TRAP1 in cancer cells. HeLa cells were treated with drugs for 30 min as indicated and incubated at 51 ºC for 5 min. Soluble fractions of the heat-treated cell extracts were analyzed by western blotting (left). Thermal aggregation curves are shown on the right. The data for quantification of protein band intensity in (B), (C), and (E) are means ± SEM from three independent experiments, and representative images are shown.

2.3.3 Structural analysis of the ternary complex of MitoQ, AMPPNP, and TRAP1.

To explore the molecular mechanism of the allosteric effects of MitoQ, we attempted to obtain complex structures through cocrystallization of MitoQ and full-length human TRAP1 (hTRAP1) under various conditions, but this was unsuccessful. Instead, full-length zebrafish TRAP1 (zTRAP1) was first crystallized in the presence of AMPPNP as reported by the Agard group,[26] and the zTRAP1 crystals were soaked with MitoQ. In this way, we determined the structures of zTRAP1 bound to both MitoQ and AMPPNP at a resolution of 2.3 Å (Figure 2.3.A). MitoQ was asymmetrically bound to a large channel generated between the MDs of two protomers, with the ubiquinone (Ub) moiety of MitoQ associated with one protomer (indicated as protomer A), whereas TPP contacts the other protomer (indicated as protomer B). The long hydrocarbon chain linking Ub and TPP of MitoQ is disordered in the structure (Figure 2.3.A-B). AMPPNP induced asymmetric buckling at the MD-CTD interface to reduce the strain caused by ligand binding in one of the protomers,[26] which consequently generates different MitoQ binding sites with the conserved nonpolar residues in the MDs of each protomer (Figures 2.3.C and 2.4). The buckled form protomer A generates a deep and narrow nonpolar pocket (L461, V468, T469, F546, and L549) that can accommodate a planar quinone ring, while the straight form protomer B has a large nonpolar surface (F368, L461, V468, T469, F546, and L549) to better accommodate phenyl rings of MitoQ (Figures 2.3.C, 2.5.A, and 2.5.B). Furthermore, the positively charged phosphonium atom of TPP lies in close proximity to E465 in protomer B and contributes to MitoQ-protomer B interactions (Figure 2.5.C).

2.3.4. MitoQ–TRAP1 interactions depend on the nonpolar nature of the binding pockets.

Among the nonpolar residues in the pocket, two highly conserved Phe residues, F368 and F546, play a pivotal role in recognizing MitoQ; Ub and TPP moieties of MitoQ interact with F546 residues from protomer A and B, respectively, through pi stacking, while TPP interacts with F368 from protomer B (F368 from protomer A was not ordered in the structure; Figure 2.3.B-C). F368A and F546A zTRAP1 mutants were inhibited by PU-H71, which targets the ATP binding pocket in the N-terminal domain (NTD), comparably to wild-type (WT) zTRAP1. By contrast, F368A and F546A mutants, either single or double, did not display MitoQ-induced elevation of ATPase activity (Figure 2.3.D). To probe the MitoQ interaction with human TRAP1, the zTRAP1 structure was compared with the full-length hTRAP1 structure recently resolved by cryo-electron microscopy (cryo-EM).27 The dimeric hTRAP1 superimposes with a root mean square deviation (RMSD) of 1.74 Å for 1126 of 1189 zTRAP1 Cα atoms, and amino acid residues forming the MitoQ binding pocket in zTRAP1 are structurally conserved in hTRAP1 (Figure 2.4.D, 2.4.E). To further confirm the binding mode of MitoQ in hTRAP1, equivalent

Phe residues (hTRAP1 F353 and F531) were mutated to Ala. F353A and F531A single mutants of hTRAP1 partially reversed the MitoQ-induced elevation of ATPase activity, and the F353A/F531A double mutant fully reversed the elevation (Figure 2.4.F), suggesting very similar modes of MitoQ interaction between zTRAP1 and hTRAP1. When binding constants (KD) between TRAP1 and MitoQ were directly measured using microscale thermophoresis (MST),29 the F353A/F531A double mutant showed a 5-fold weaker interaction with MitoQ compared with the WT protein (KD values of 30.6 μM and 6.6 μM, respectively; Figure 2.3.E). MitoQ binds to the MD of TRAP1 in an asymmetric bipartite manner, and conserved hydrophobic residues including F368 and F546 are important for forming the binding interface.

2.3.5. The importance of the distance between quinone and TPP moieties.

MitoQ was made by conjugating the Ub moiety (2,3-dimethoxy-5-methyl-1,4-benzoquinone, CoQ_0) with decyl TPP (TPP-10). The requirement of the TPP moiety in the interaction with TRAP1 was further analyzed by ATPase activity assay. Neither Ub nor its C_{10}-conjugated form (decylubiquinone, Ub-C10; Figure 2.6.A) further augmented TRAP1 ATPase activity in the presence of TPP-10 and TPP-1 (Figure 2.6.B). These results suggest that Ub alone, with or without a long hydrocarbon linker (C_{10}), did not significantly interact with TRAP1, without tethering to the TPP moiety.

In addition to tethering, the distance between Ub and TPP appears to be essential for MitoQ interaction with TRAP1, consistent with the fact that the binding pockets for Ub and TPP moieties in protomer A and B are separated by ~25 Å (Figure 2.4.E). Furthermore, short linker-TPPs did not affect TRAP1 activity as much as long linker-TPPs (Figure 1G). To confirm this experimentally, we prepared short linker derivatives of MitoQ and Mito-CP, and long linker derivatives of Mito-VitE, named $MitoQ^S$, $Mito\text{-}CP_S$, and $Mito\text{-}VitE^L$, respectively (Figures 2.3.F and 2.6.C). As expected, $MitoQ^S$ and $Mito\text{-}CP_S$ did not significantly elevate the ATPase activity of TRAP1, while $Mito\text{-}VitE^L$ did dramatically elevate the ATPase activity of TRAP1, similar to TPP-16 (Figure 2.6.D). Consistently, $Mito\text{-}VitE^L$ showed cellular TRAP1 inhibition activity, while $MitoQ^S$ and $Mito\text{-}CP^S$ did not (Figures 2.3.G, 2.2.E, 2.6.E). Consequently, short linker $MitoQ^S$ lost its mitochondrial TRAP1 inhibitor activity according to mitochondrial membrane potential (TMRM staining) and ROS production (Mito-SOX staining) experiments (Figure 2.3.H). Collectively, the results suggest that both tethering and appropriate distancing between Ub and TPP moieties are necessary to establish a strong interaction between MitoQ and MD in TRAP1.

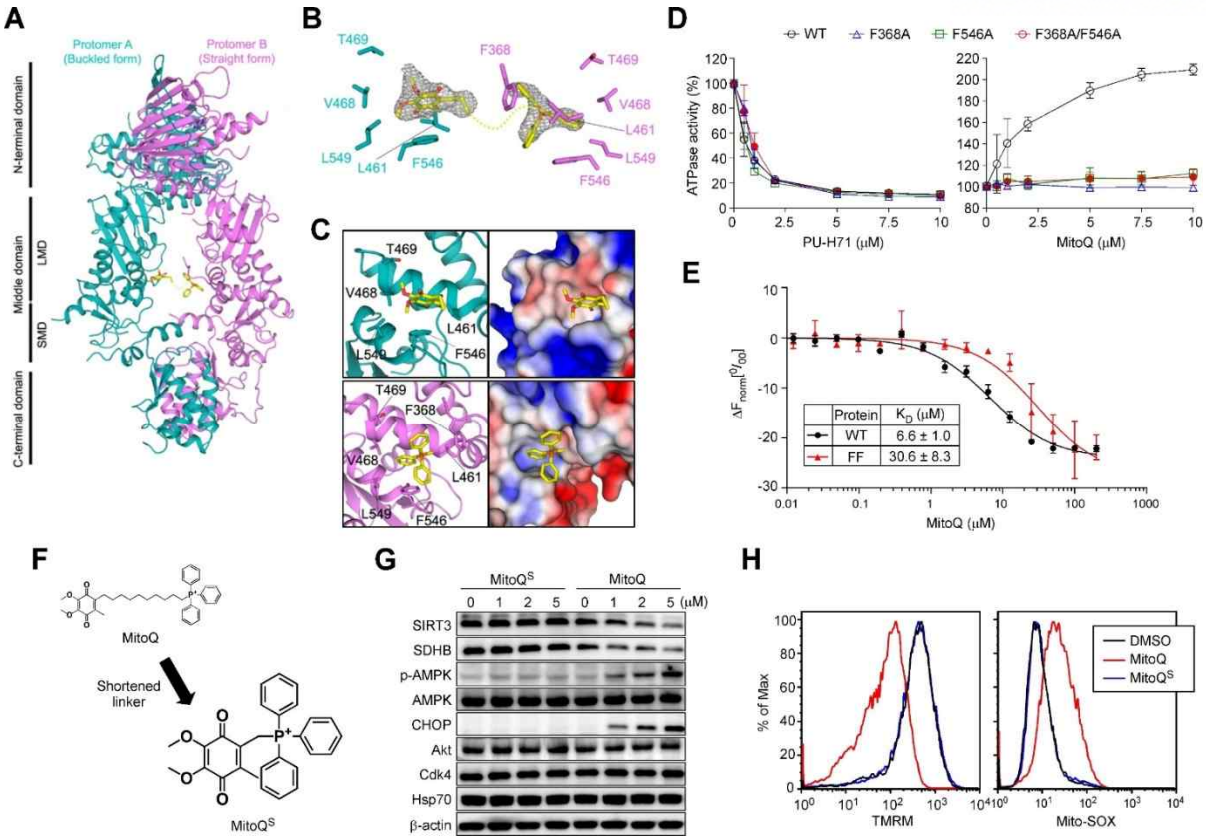

Figure 2.3. Analysis of the TRAP1–MitoQ interaction.

(A) Overall structure of the zTRAP1 dimer complexed with MitoQ and AMPPNP. Protomer A (buckled form) and protomer B (straight form) are colored cyan and magenta, respectively. (B) Detailed view of the recognition of MitoQ by TRAP1. The side chains of residues interacting with MitoQ are shown. The Fo-Fc map (gray mesh) around MitoQ was calculated in the absence of MitoQ (2.3 Å resolution, contoured at 2.0 σ). (C) MitoQ binding pocket structures. MitoQ binding pockets for Ub (top) and TPP (bottom) are shown in ribbon diagrams (left) and surface models depicting electrostatic potential (right). (D) ATPase activity of zTRAP1 mutants. ATPase activities of wild-type (WT) and mutant zTRAP1 proteins were analyzed and compared. Data are means ± SEM (n = 5). (E) Microscale thermophoresis (MST) analysis. Fluorescence-labeled WT or mutant hTRAP1 was incubated with various concentrations of MitoQ and analyzed by Monolith NT.115 (NanoTemper Technologies). The difference in normalized fluorescence (ΔFnorm, [‰]) was calculated. Data are means ± SEM (n = 3). (F) Chemical structure of MitoQS. (G) Effects of MitoQS on cellular Hsp90 and TRAP1. 22Rv1 cells were treated with drugs as indicated for 2 h and analyzed by western blotting. Activation of AMPK (p-AMPK) and induction of the mitochondrial unfolded protein response (CHOP) were analyzed as cellular markers for mitochondrial dysfunction upon TRAP1 inhibition.[7, 28] (H) Mitochondrial membrane potential and ROS production. 22Rv1 cells labeled with TMRM (left) or Mito-SOX (right) were incubated with 5 μM drugs for 2 h and analyzed by flow cytometry.

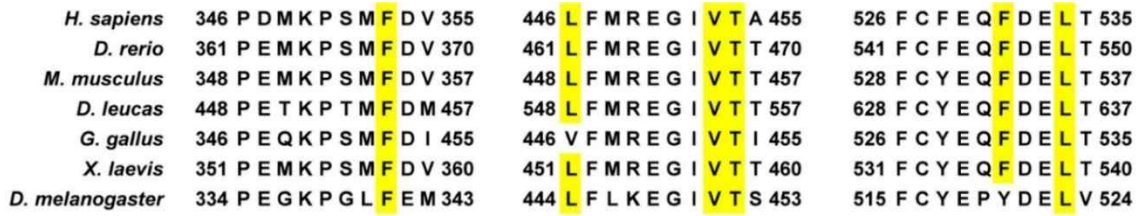

Figure 2.4. Evolutionary conserved MitoQ-interacting residues in TRAP1. The amino acid sequences of MitoQ-interacting residues and flanking region from various organisms were aligned, and the residues directly contacting MitoQ are highlighted

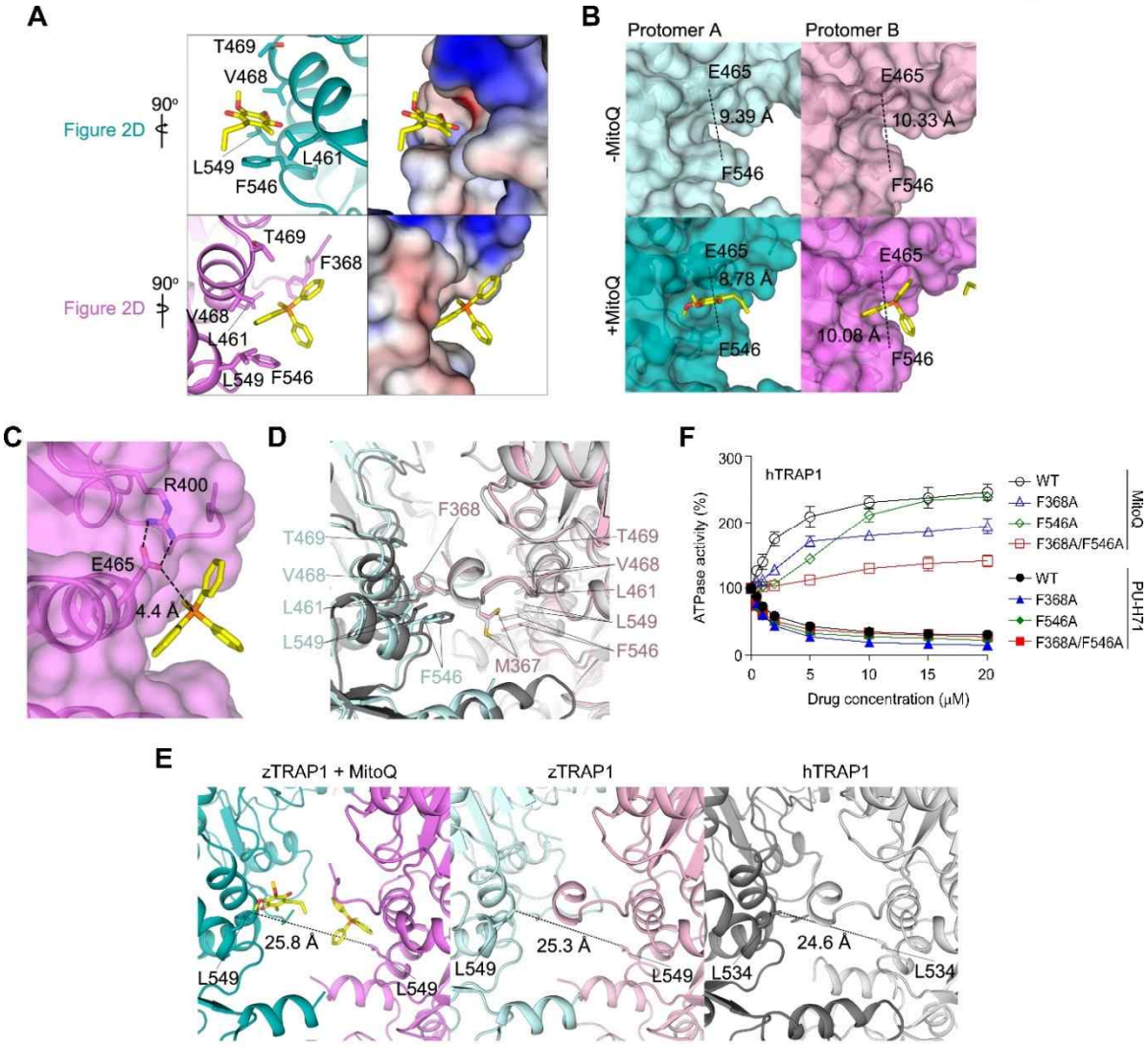

Figure 2.5. Molecular interaction between TRAP1 and MitoQ.

(A) MitoQ binding pocket. MitoQ (yellow) binding pockets of each protomer for ubiquinone (Ub, top) and triphenylphosphonium (TPP, bottom) are shown. These views are rotated 90° about a perpendicular axis relative to Figure 2.3.C, and are shown as a ribbon diagram (left) and surface model depicting electrostatic potential (right). (B) Comparison of MitoQ binding pockets between protomer A (Ub binding pocket) and protomer B (TPP binding pocket) in the absence (pale cyan, pale magenta) and presence (cyan, magenta) of MitoQ. Distance between Glu 465 and Phe 546 residues from the same protomer are indicated. The TPP binding pocket in protomer B is slightly larger than the Ub binding pocket in protomer A (top). MitoQ binding induces local conformational changes (narrowing of the pocket in TRAP1) to better fit the drug molecule (bottom). (C) Ionic interaction of TPP with Glu 465 in protomer B. The distance between the E465 oxygen atom and the protonated phosphine (TPP) was indicated. (D) Ribbon diagram showing superposition of hTRAP1 and zTRAP1. The MitoQ binding pocket of zTRAP1 (pale cyan and pale magenta, PDB access code 4IPE) is compared with that of the full-length hTRAP1 structure (gray and pale gray; PDB access code 6XG6). (E) Structural comparison of the MitoQ binding region in zTRAP1 and hTRAP1. The distances between two Leu 549 residues from each protomer of dimeric zTRAP1 (equivalent to Leu 534 residues in hTRAP1) are indicated. (F) Drug effects on the ATPase activity of TRAP1. The ATPase activity of wild-type and mutant hTRAP1 proteins was analyzed. Data are means ± SEM (n = 6).

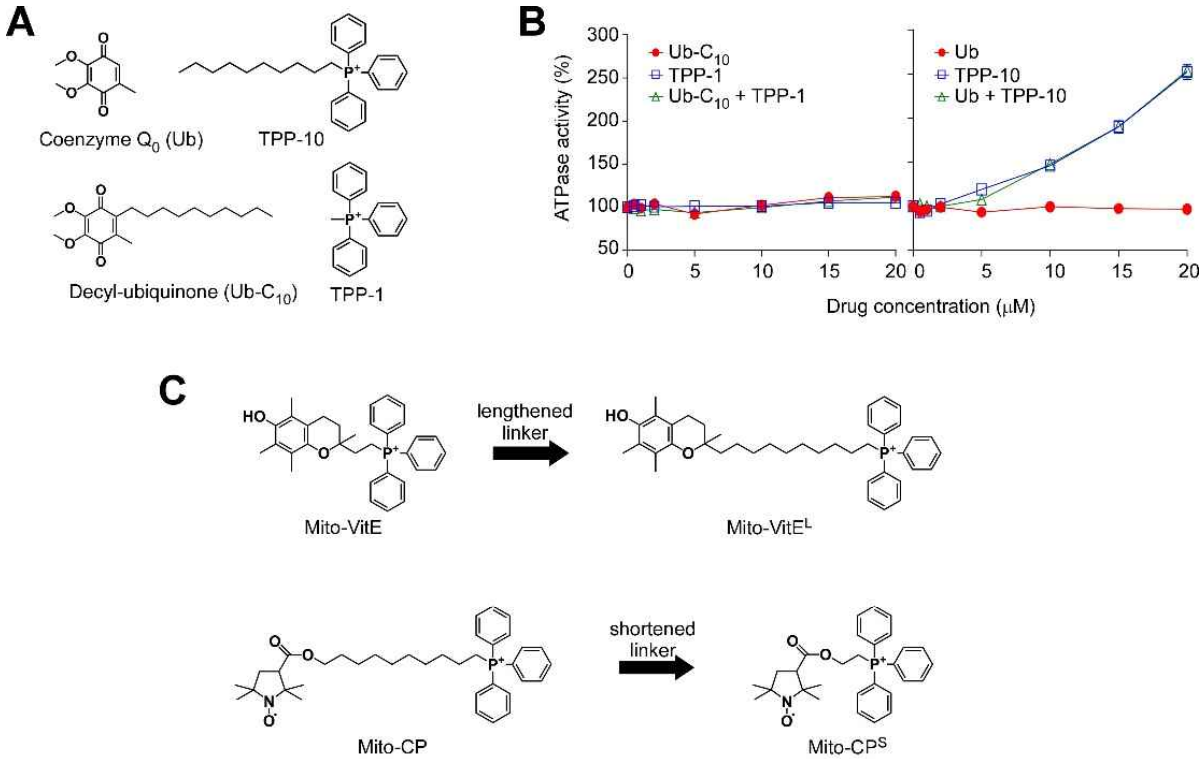

Figure 2.6. The importance of the distance between Ub and TPP moieties.

(A) Chemical structures of Ub and Ub-C_{10}. CoenzymeQ_0 is indicated as Ub. Decyl-ubiquinone is indicated as Ub-C_{10}. (B) hTRAP1 ATPase activity. An uncoupled mixture of Ub/TPP-10 or Ub-10/TPP-1 has no combinational effect on TRAP1. Data are means ± SEM (n = 5). (C) Chemical structures of Mito-VitE^L and Mito-CP^S. (D) TRAP1 ATPase activity. ATPase activity of hTRAP1 was measured in the presence of drugs and compared with each other. Data are means ± SEM (n = 4). (E) Effects of Mito-VitEL and Mito-CP^S on cellular Hsp90 and TRAP1. 22Rv1 cells were treated with drugs as indicated for 2 h and analyzed by western blotting

2.3.6. Reorganization of TRAP1 local structure upon MitoQ binding.

AMPPNP binding induces structural asymmetry of zTRAP1, especially around residue G471 in MD.[26] Residues 311-470 were designated the large MD (LMD) and residues 472-571 the small MD (SMD). To explore the effect of MitoQ binding on LMD and SMD, the structures of zTRAP1-AMPNP in the presence and absence of MitoQ were comparatively analyzed by superimposing them. The overall structures with and without MitoQ are very similar (RMSD = 0.7607 Å, Figure 2.7.A). However, without MitoQ, the extended loop containing M367 and F368 in LMD forms inter-protomer MD–MD interactions between the two protomers, while these interactions are completely absent when MitoQ binds to TRAP1 (Figures 2.7.B, 2.8.A). Rather, trans-protomer interactions between M367 of protomer A and F368 of protomer B are replaced with TPP and Ub moieties, respectively (Figure 2.7.B, 2.7.C). In more detail, the intermolecularly projected F368 residue points back toward protomer B and directly contacts the phenyl ring of TPP, and the M367 residue projecting from protomer A is disordered in the structure of TRAP1 bound to MitoQ (Figures 2.7.B-C, 2.8.A). SMD and CTD in protomer A had relatively high B-factors (Figure 2.8.B), consistent with a previous report.[26] MitoQ binding pushed SMD of protomer A further away (~2.34 Å) from protomer B (Figure 2.8.C), and concomitantly, an α-helix (residues 526-535) of protomer A is partially unwound, and loops in SMD (residues 506-507, 533-537) and CTD (residues 616-618) of protomer A are disordered (Figure 2.8.A). A disulfide bond between C516 and C542 is exclusively formed in protomer A but not in protomer B (Figure 2.8.D),[26] which may contribute to the structural stabilization of SMD upon MitoQ-induced local unfolding.

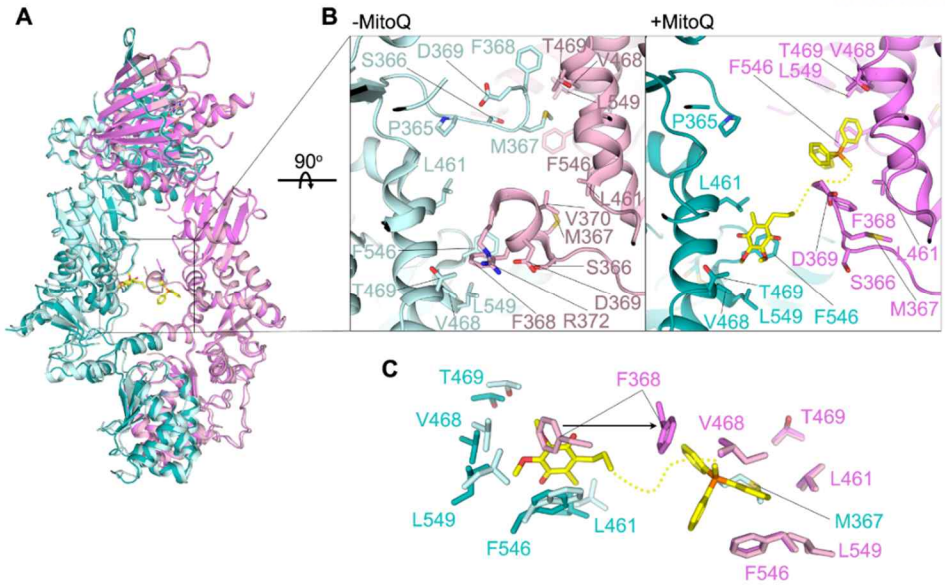

Figure 2.7. Conformational changes of zTRAP1 upon MitoQ binding.

(A) Comparison of TRAP1 structures. MitoQ (yellow)-bound structure of zTRAP1, protomer A (Cyan), and B (magenta), overlayed with that of MitoQ-unbound zTRAP1 (protomer A and B are colored pale cyan and pale magenta, respectively). (B) Close-up view of the binding region in the absence (left) and presence (right) of MitoQ. This view is rotated 90º about a horizontal axis relative to (A). (C) MitoQ-induced conformational rearrangement of zTRAP1. Large conformational changes of F368 from protomer B are indicated by a black arrow. The M367 residue from protomer A is disordered in the structure when MitoQ binds to zTRAP1. The hydrocarbon chain connecting the Ub and TPP moieties of MitoQ is disordered in the structure and indicated by a yellow dotted line.

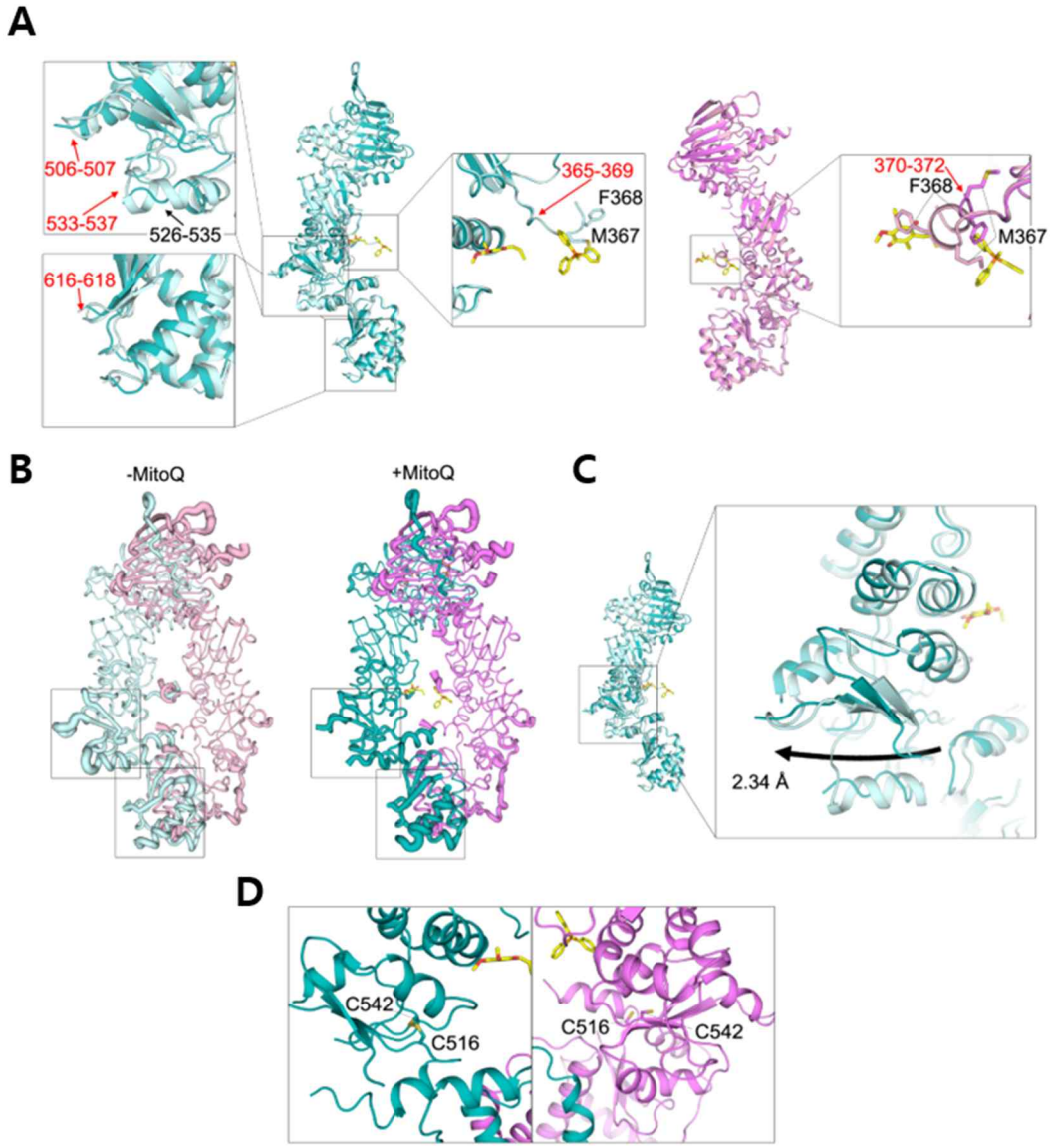

Figure 2.8. MitoQ-induced conformational changes of zTRAP1.

(A) Detailed view of conformational changes. The complex structures of zTRAP1–AMPPNP (pale cyan and pale magenta) and zTRAP1–AMPPNP–MitoQ (cyan and magenta) are superimposed. Close-up views highlight a large conformational change in TRAP1 upon MitoQ binding. Disordered amino acid residues and the α-helix unwound upon MitoQ binding are indicated as red and black arrows, respectively. (B) B-factor representation of zTRAP1 in the absence and presence of MitoQ. B-factor values are proportional to the thickness of the line. (C) Overlaid structures of zTRAP1 protomer A in the absence (pale cyan) and presence (cyan) of MitoQ. The right close-up view highlights the SMD region that undergoes the largest conformational rearrangement. The black arrow indicates the direction of transition when MitoQ binds TRAP1. (D) Close-up view of the disulfide bond between C516 and C542. The disulfide bond is present in SMD of protomer A (left) but not protomer B (right).

2.3.7. MitoQ interaction with the client binding site of TRAP1.

TRAP1 ATPase activity is closely correlated with conformational transition between open and closed forms.[20, 30] Thus, to address the effect of MitoQ on the TRAP1 conformation, we analyzed the solution structure of hTRAP1 using small-angle X-ray scattering (SAXS). The results showed that MitoQ induced the formation of the closed form of the hTRAP1 dimer to a similar extent to AMPPNP treatment (Figure 2.10.A). Similarly, AMPPNP-induced closed conformation did not alter the binding affinity between TRAP1 and MitoQ, considering KD values (μM) of 6.6±1.0 and 6.9±1.1 in the absence and presence of AMPPNP, respectively (Figures 2.3.E and 2.10.B), indicating AMPPNP is not necessary for MitoQ binding. MitoQ-induced conformation was completely reversed by the F353A/F531A double mutation (Figure 2.10.C). The analyses of solution structures strongly validate our crystal structure in both overall conformation and local key interactions.

To further explore the effect of MitoQ binding on TRAP1, we compared our results with the cryo-EM structure of the Hsp90 complex with the cochaperone Cdc37 and the client protein Cdk4.31 The C-terminal strand of Cdk4 interacts with the lumen of Hsp90 MD mainly through hydrophobic interactions (Figure 2.9.A). Interestingly, when the 3D structures of zTRAP1–MitoQ–AMPPNP and Hsp90–Cdc37–Cdk4 were compared, the location of MitoQ was found to completely overlap with that of Cdk4 (Figure 2.9.A). Based on the analysis, we speculated that MitoQ binds to the client binding site to block interaction with real client proteins. Consistently, MitoQ effectively competed with the known TRAP1 client proteins SIRT3 and SDHB in a dose-dependent manner, while PU-H71 targeting the ATP binding site did not (Figure 2.9.B). F353A and/or F531A mutation of hTRAP1 dramatically reduced interactions with client proteins (Figure 2.9.C). The MitoQ-induced elevation of ATPase activity appears to mimic the activation of ATPase activity upon client binding to Hsp90.[32-33] As expected, recombinant SIRT3 elevated the ATPase activity of TRAP1 in a dose-dependent manner (Figure 2.11.A), but this SIRT3 effect was suppressed in the MitoQ binding-defective TRAP1 F353A/F531A mutant (Figure 2.11.B). TRAP1 could activate the deacetylase activity of SIRT3 in vitro through direct interaction,6 and MitoQ inhibited TRAP1-mediated SIRT3 activation (Figure 2.9.D). Similarly, F353A/F531A mutation significantly impaired the SIRT3-activating function of TRAP1 (Figure 2.9.E) and was unable to further stabilize client proteins, unlike WT TRAP1, when overexpressed in 22Rv1 cells (Figure 2.9.F). Thus, the results collectively indicate that MitoQ interacts with the client binding site and competes efficiently with client proteins of TRAP1.

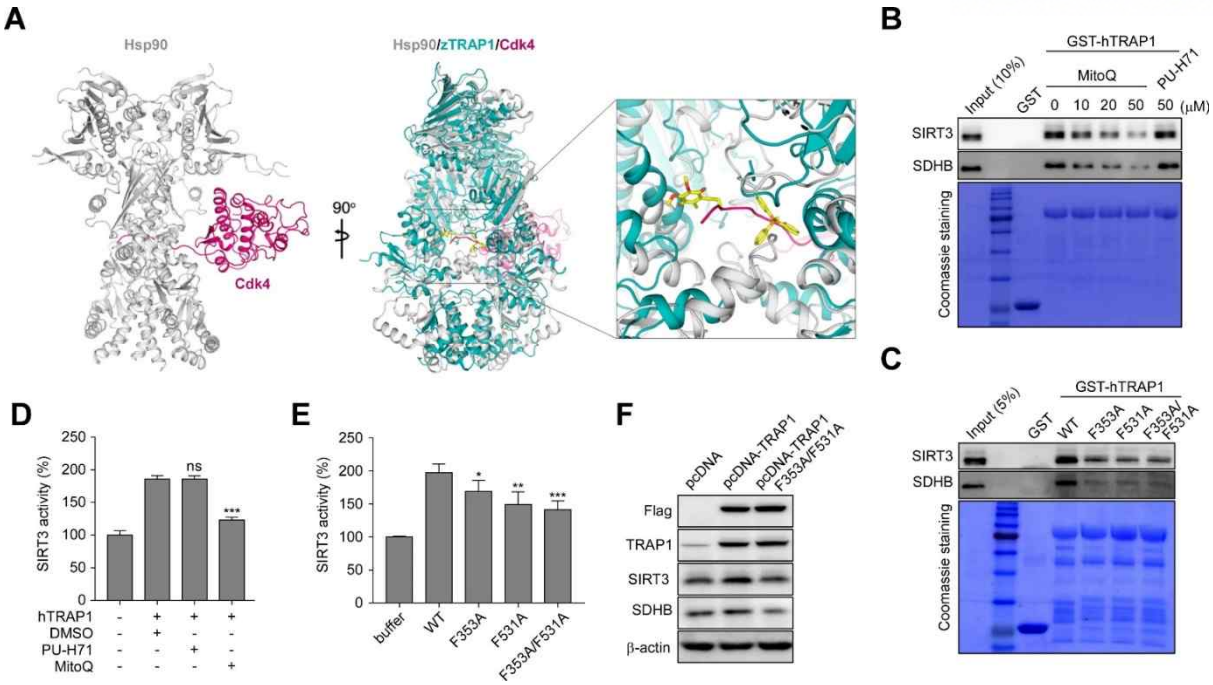

Figure 2.9. MitoQ interaction with the client binding site of TRAP1.

(A) Structural comparison between Hsp90–Cdc37–Cdk4 and zTRAP1–MitoQ. The picture on the left shows the overall structure of Hsp90 bound to Cdk4 (PDB access code: 5FWK). The structure of Cdc37 is removed for clarity. The ribbon diagram on the right shows a superposition of Hsp90–Cdk4 and zTRAP1–MitoQ complexes. The close-up view highlights the Cdk4 binding region in the superposed structure. Hsp90, Cdk4, and zTRAP1 are colored gray, magenta, and cyan, respectively. (B) In vitro pull-down assay with hTRAP1. hTRAP1 beads were incubated with 22Rv1 mitochondrial extracts and drugs (MitoQ or PU-H71) at the indicated concentrations, and bound TRAP1 client proteins (SIRT3 and SDHB) were analyzed by western blotting. (C) Interaction of MitoQ binding-defective TRAP1 mutants with client proteins. Mitochondrial extracts were incubated with beads containing hTRAP1 F353A and/or F531A mutant protein, and bead-bound proteins were analyzed by western blotting. (D) Activation of SIRT3 enzyme activity. Deacetylase activity of SIRT3 was measured in the presence of hTRAP1 and drugs (10 μM) as indicated. (E) SIRT3 activation by mutant hTRAP1. SIRT3 activity was measured in the presence of WT or F353A/F531A mutant hTRAP1, and enzyme activities were compared. (F) Overexpression of F353A/F531A hTRAP1. 22Rv1 cells were transfected with plasmids as indicated and analyzed by western blotting. Data in (D) and (E) are means ± SEM (n = 5). *$p < 0.05$; **$p < 0.01$; ***$p < 0.001$; ns, not significant.

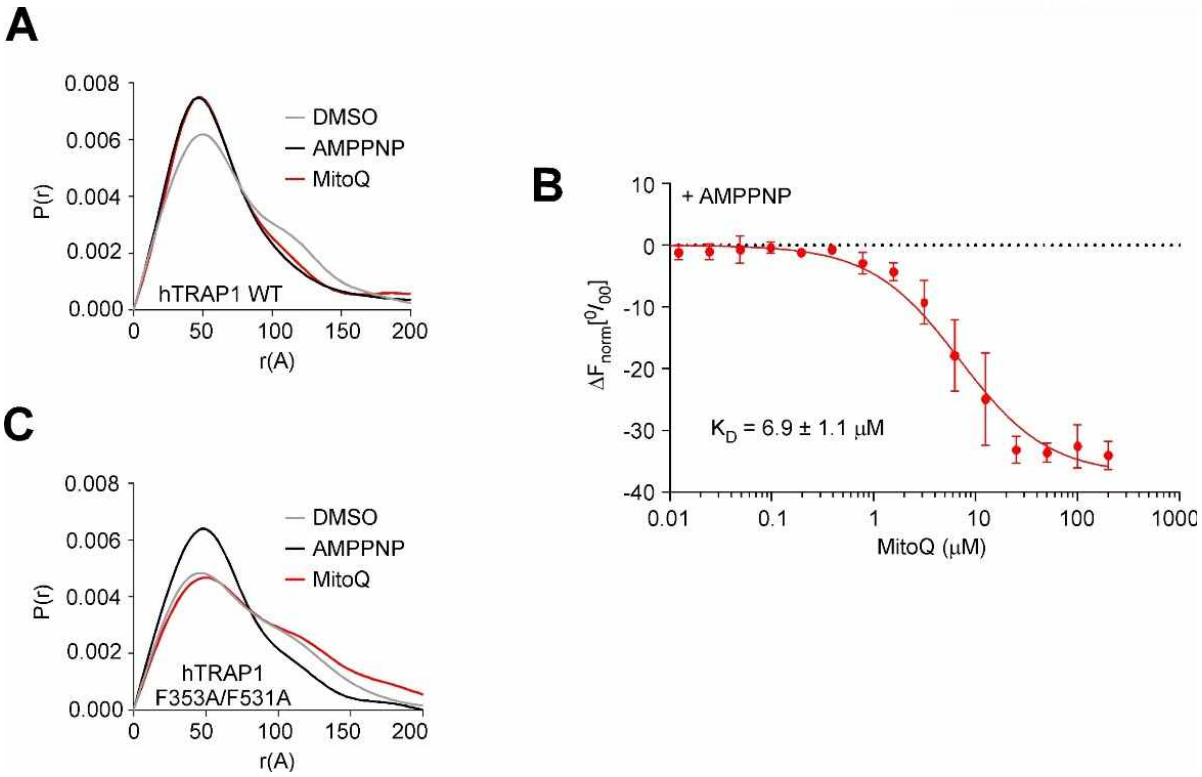

Figure 2.10. SAXS and MST analyses of TRAP1. (A) P(r) curves of TRAP1. Wild-type (WT) hTRAP1 was incubated with 2 mM AMPPNP or 50 μM MitoQ and analyzed by SAXS. (B) Microscale thermophoresis (MST) analysis. Fluorescence-labeled wild type hTRAP1 was incubated with MitoQ same as in Figure 2E in the presence of 2 mM AMPPNP, and analyzed by Monolith NT.115 (NanoTemper Technologies). (C) P(r) curves of a MitoQ binding-defective TRAP1 mutant. MitoQ or AMPPNP was incubated with hTRAP1 F353A/F531A and analyzed by SAXS.

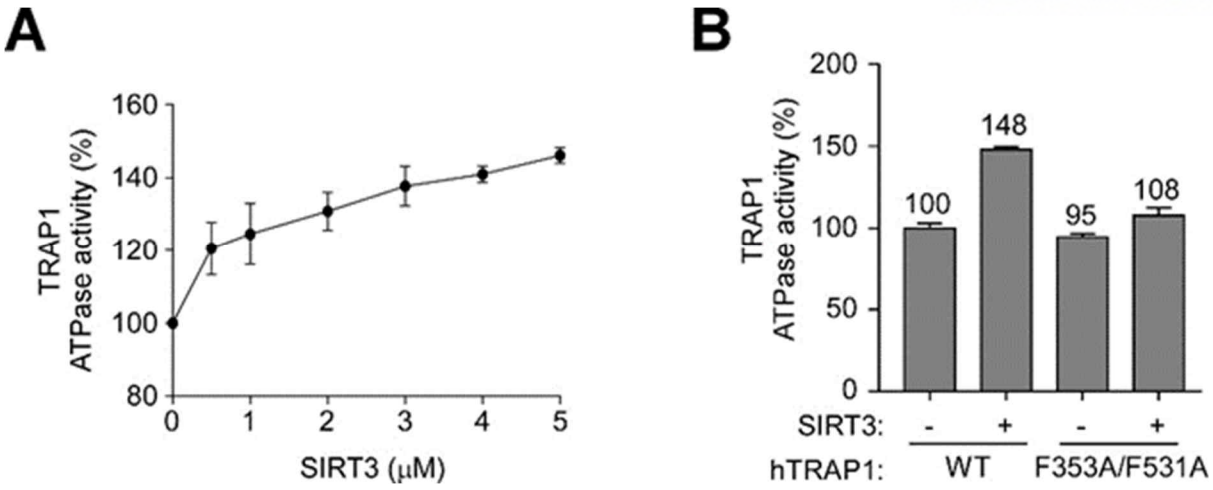

Figure 2.11. SIRT3 stimulation of TRAP1 ATPase activity.

(A) The ATPase activity of hTRAP1 was measured in the presence of recombinant SIRT3 as indicated. (B) The effect of SIRT3 on the client binding-defective TRAP1 mutant. The ATPase activity of WT and mutant hTRAP1 (0.5 μM) was measured in the presence or absence of SIRT3 (5 μM). Data are means ± SEM (n = 6), and mean values are indicated.

2.3.8. Analysis of the TRAP1 interactome using MitoQ.

To understand functions of chaperones in the cellular context, we analyzed the TRAP1 interactome, including clients and modulators. Systematic analysis of the TRAP1 interactome could provide insights into the mitochondrial functions of chaperones. To this end, MitoQ was employed to specifically enrich proteome components interacting with TRAP1. Specifically, TRAP1 bead-bound proteins (from mitochondrial extracts of HeLa and 22Rv1 cells) were eluted by MitoQ and subsequently analyzed by LC-MS/MS (Figure 2.12.A). A total of 371 proteins were initially identified, and this number was reduced to 194 by selecting proteins with three or more identified unique peptides and with 2-fold or more spectral counts in MitoQ-eluted samples compared with controls (Figure 2.13.A-B). The list was further reduced to 103 proteins (43 proteins identified in both HeLa and 22Rv1 cells) by selecting mitochondrial proteins using MitoCarta3.0 and MitoXplorer databases[34-35] (Figure 2.12.B). Among the 103 proteins, 73 were newly identified TRAP1 interactors not reported previously. Most of the identified TRAP1-interacting proteins (101/103) are localized in the mitochondrial matrix and inner membrane (IM) where TRAP1 exerts its chaperone function (Figure 2.13.C). Pathway analysis using MitoXplorer[35] revealed that the 103 TRAP1 interactors participate in various mitochondrial pathways: replication and maintenance of mitochondrial DNA; transcription and translation for mitochondrial gene expression; metabolic pathways including the tricarboxylic acid cycle, oxidative phosphorylation, and fatty acid β-oxidation; amino acid and pyruvate metabolism; detoxification of ROS; protein homeostasis including chaperone, protease, preprotein import, and sorting machineries (Figure 2.13.D). Although previously reported TRAP1 clients such as SDHB and SIRT3 were not detected by MS, western blotting analysis of eluted samples revealed the presence of these client proteins (Figure 2.12.C). To further confirm the interactions between TRAP1 and the identified proteins, eight proteins (GLS, PRDX3, SSBP1, NDUFS1, ATP5F1B, FH, LONP1, and HSPD1) were randomly selected from the list of proteins detected in both HeLa and 22Rv1 cells. Consistent with the proteomics results, all eight proteins interacted with TRAP1, and the interactions were effectively blocked by MitoQ treatment (Figure 2.12.C). To determine TRAP1 dependency, protein expression was analyzed after pharmacological and genetic inactivation of TRAP1 in the cancer cell. Expression of half of the proteins (GLS, PRDX3, SSBP1, and NDUFS1) was reduced, but the other four (ATP5F1B, FH, LONP1, and HSPD1) were not affected by TRAP1 inactivation (Figure 2.12.D-E). TRAP1 inhibition did not affect mRNA levels of the TRAP1 interactors (Figure 2.12.F), suggesting post-translational regulation of protein stability by the chaperone. Interestingly, the effect of MitoQ was indistinguishable from those of gamitrinib and TRAP1 small interfering RNA (siRNA), further confirming specific TRAP1 inactivation by MitoQ.

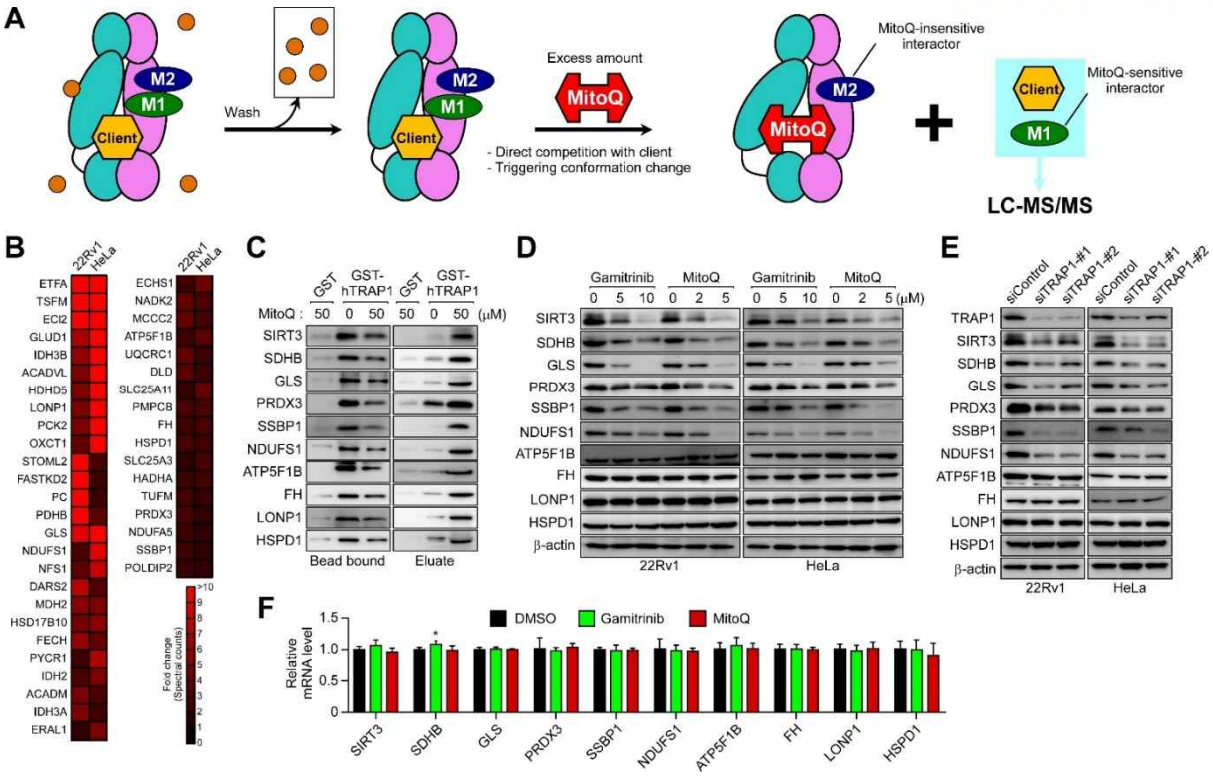

Figure 2.12. Analysis of TRAP1 interactomes.

(A) Schematic representation of the enriched TRAP1 interactome following MitoQ treatment. TRAP1 beads were incubated with mitochondrial extracts prepared from 22Rv1 and HeLa cells. After washing beads to remove non-specifically-bound proteins, TRAP1 bead-bound proteins were eluted with 50 μM MitoQ to specifically dissociate not only client proteins (competing directly with MitoQ for the client binding site) but also TRAP1 interactors (M1) sensitive to MitoQ-induced conformational changes (including TRAP1 modulators as well as client proteins). By contrast, some interactors (M2) may not be dissociated from TRAP1 by MitoQ-induced conformational changes. MitoQ-eluted proteins were analyzed by LC-MS/MS. Among the identified proteins, mitochondrial proteins were selected using Mitocarta3.0 and MitoXplorer databases. (B) Heatmap of the mitochondrial TRAP1 interactome. The fold change of 43 mitochondrial proteins in spectral counts of MitoQ-eluted samples were compared with controls. (C) Western blotting analysis of pull-down samples. TRAP1-interacting proteins were analyzed by western blotting. Briefly, 22Rv1 mitochondrial extracts were incubated with glutathione S-transferase (GST) and GST-hTRAP1 beads. After washing the beads, TRAP1 bead-bound proteins were eluted by MitoQ. Bead (pellet, left) and MitoQ-eluted samples (supernatant, right) were analyzed by western blotting. (D) Effects of pharmacological inhibition of TRAP1 on selected interactors. 22Rv1 and Hela cells were incubated with gamitrinib (12 h) or MitoQ (2 h) at the indicated drug concentrations, and analyzed by western blotting. (E) Effects of genetic inhibition of TRAP1 on the interactors. 22Rv1 and Hela cells were treated with TRAP1 siRNAs and analyzed by western blotting. (F) Transcription levels of TRAP1 interactors. 22Rv1 cells were incubated with 5 μM gamitrinib for 12 h or 2 μM MitoQ for 2 h, and then analyzed by real-time PCR. Data are means ± SEM ($n = 5$; $^*p < 0.05$).

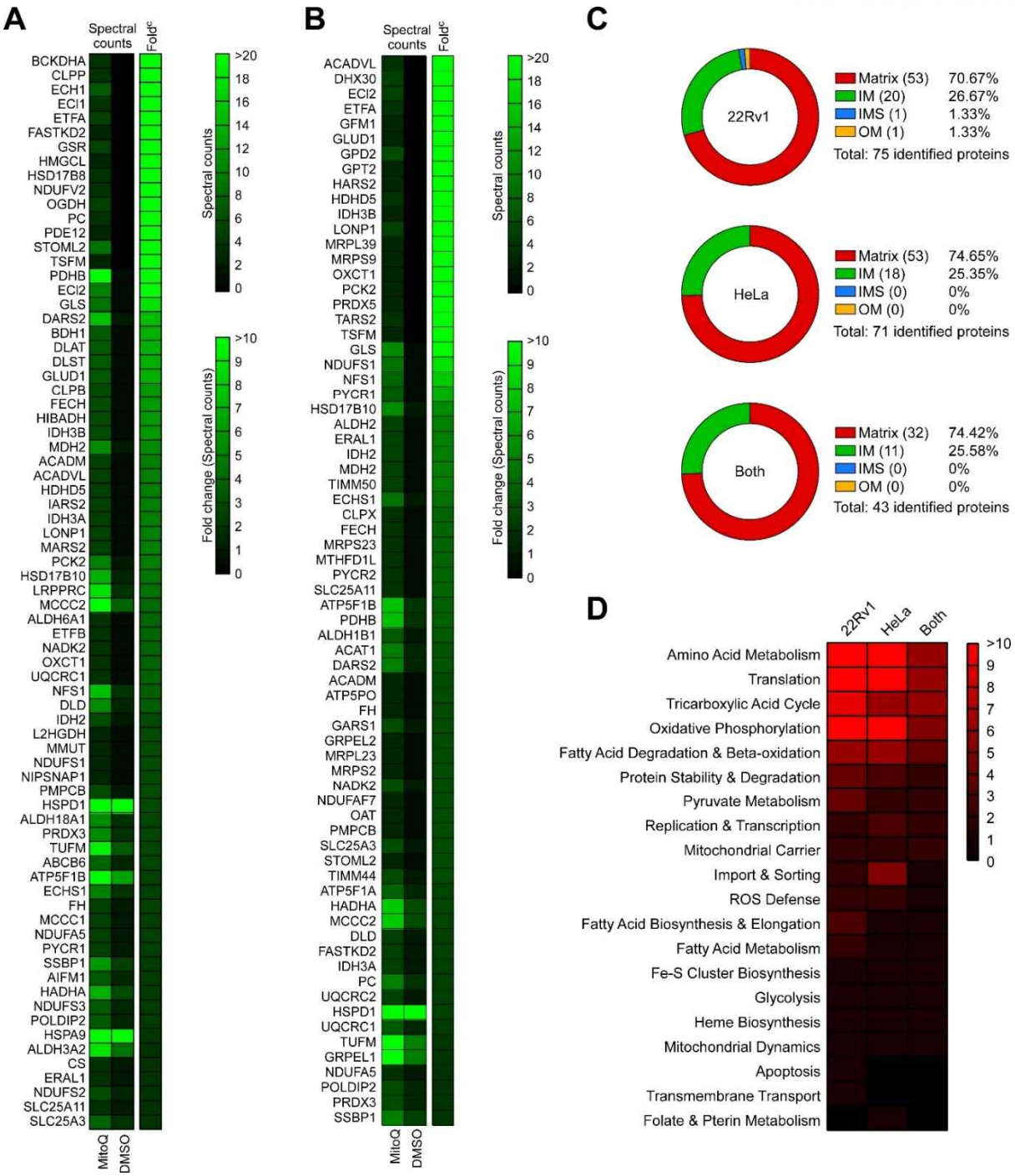

Figure 2.13. Identification of TRAP1-interacting proteins.

(A) Heatmap of the TRAP1 interactome identified in 22Rv1 cells. (B) Heatmap of the TRAP interactome identified in HeLa cells. A total of 194 MitoQ-eluted TRAP1-interacting proteins were reduced to 103 by selecting mitochondrial proteins. The fold change of mitochondrial proteins in spectral counts of MitoQ-eluted samples compared with DMSO-eluted samples was calculated. (C) Sub-mitochondrial distribution of the TRAP1 interactome. Proteins identified in HeLa, 22Rv1, and both cell lines were grouped into mitochondrial matrix, inner membrane (IM), intermembrane space (IMS), and outer membrane (OM) according to their reported location. (D) Mitochondrial process analysis of the TRAP1 interactome by MitoXplorer. The number of identified proteins participating in each pathway is shown.

2.3.9. MitoQ inactivates Hsp90.

TRAP1 shares significant sequence homology and structural similarity with Hsp90, one of the most abundant and conserved chaperones.[12, 36] Structural comparison of TRAP1 with Hsp90 and Grp94 (endoplasmic reticulum paralog of Hsp90) at the MitoQ binding pocket revealed that TRAP1, Hsp90, and Grp94 all form hydrophobic pockets, although the accessibility to the pocket differs slightly among them (Figure 2.14.A). Unlike zTRAP1 and hTRAP1, hydrophobic residues from one protomer occupy the pocket from the other protomer in Hsp90 and Grp94; in more detail, the side chain of Leu611 from Hsp90 faces toward the entry site of the pocket, and Tyr667 of Grp94 are more deeply buried inside the hydrophobic pocket of the other protomer. This arrangement might inhibit access of MitoQ to the hydrophobic pocket through steric hindrance. Consistently, binding constants for TRAP1 and Hsp90 were determined as 6.6 μM and 26.8 μM, respectively, using MST (Figure 2.14.B). Hsp90 ATPase activity was marginally (~1.3 fold) elevated by MitoQ (Figure 2.15). The data indicate that MitoQ has inhibitory activity toward Hsp90, though not as strong as TRAP1, and may affect the ATPase activity in a different manner than TRAP1.

Drug treatment for less than 6 h induced degradation of TRAP1 client proteins but did not show any signs of Hsp90 inhibition (Figures 2.1.D, 2.1.I, 2.3.G, 2.6.E); treatment for longer than 12 h started to show degradation of Hsp90 client proteins Akt and Cdk4 (Figure 2.14.C). These results suggest that MitoQ immediately accumulates in mitochondria as it is depleted from the cytoplasm, and upon mitochondrial dysfunction, including loss of membrane potential caused by TRAP1 inhibition, MitoQ can be redistributed to the cytoplasm to inhibit Hsp90. To examine the effects of MitoQ on Hsp90 in the absence of mitochondrial drug accumulation, mitochondria-depleted HeLa (ρ^0) cells were prepared. As expected, following a short (6 h) incubation, MitoQ reduced expression of Hsp90 clients by as much as did PU-H71 in ρ^0 cells (Figure 2.14.D), indicating potent Hsp90 inhibitory activity of MitoQ in the absence of mitochondrial drug accumulation. However, HeLa ρ^0 cells became resistant to MitoQ (Figure 2.14.E), further confirming that the mitochondriotoxic effects of the drug are the prime mechanism of action of the drug.

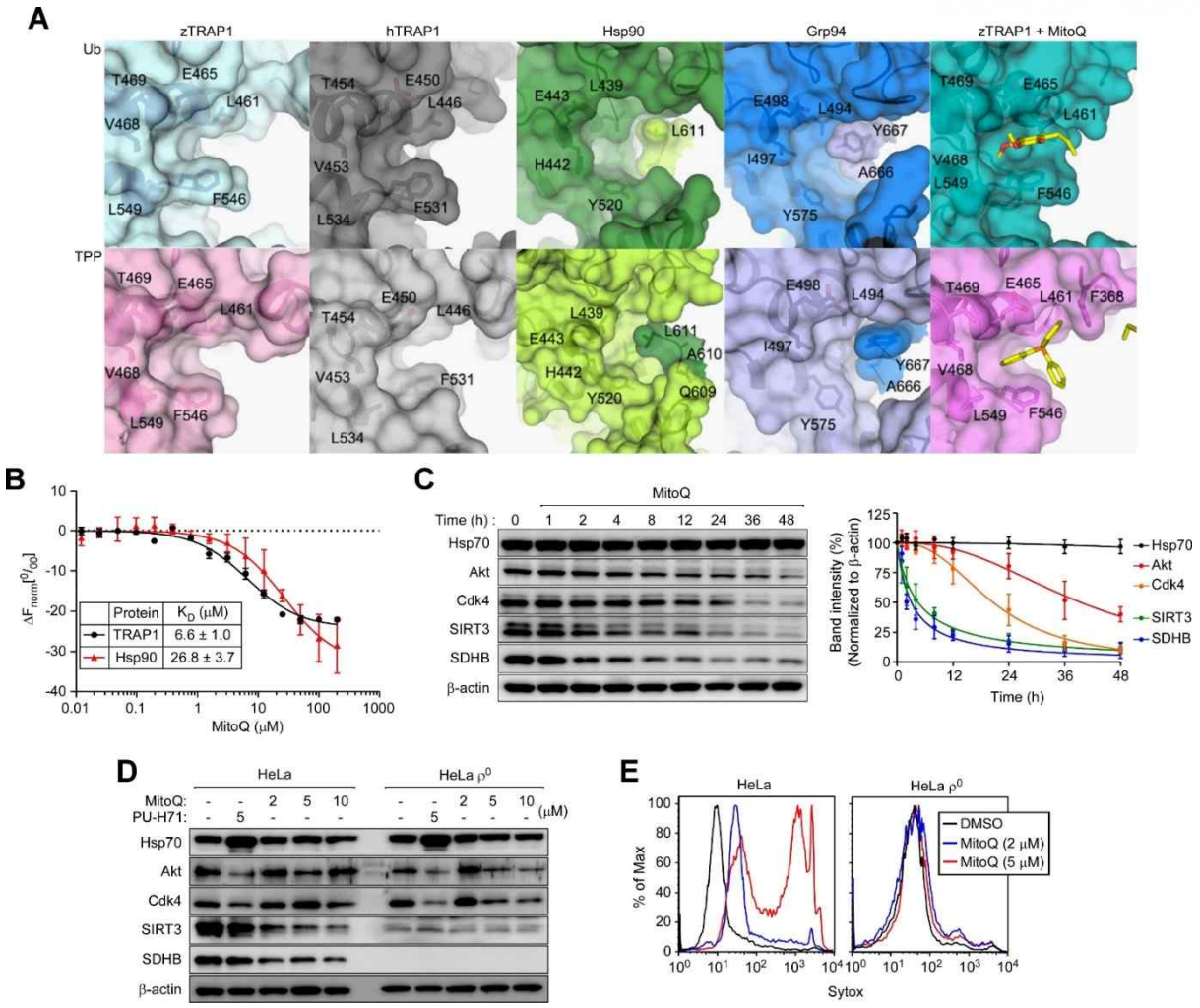

Figure 2.14. MitoQ inhibition of Hsp90.

(A) Structural comparison of MitoQ binding pockets among Hsp90 family proteins. The pocket structures of zTRAP1 (PDB access code: 4IPE), hTRAP1 (PDB access code: 6XG6), Hsp90 (PDB access code: 5FWK), and Grp94 (PDB access code: 5ULS) complexed with ATP analogs were compared with that of zTRAP1–AMPPNP–MitoQ (far right). Each protomer in the dimer is colored differently. Residues involved in forming pockets are shown in stick representation. (B) Comparison of binding constants. Fluorescence-labeled hTRAP1 and Hsp90 at a concentration of 200 nM were incubated with MitoQ (0.0061–200 μM) and analyzed by microscale thermophoresis. The difference in normalized fluorescence (ΔFnorm, [‰]) is presented. (C) Destabilization of client proteins of TRAP1 and Hsp90 by MitoQ. HeLa cells were incubated with MitoQ (2 μM) at the indicated time points and analyzed by western blotting (left). All band intensities were quantified, normalized against β-actin, and compared with each other (right). (D) Effects of MitoQ on mitochondria-depleted HeLa (ρ^0) cells. HeLa and HeLa ρ0 cells were incubated with MitoQ or PU-H71 for 6 h as indicated, and analyzed by western blotting. (E) Cell death analysis. HeLa and HeLa ρ^0 cells were incubated with MitoQ as indicated for 12 h, stained with Sytox, and analyzed by flow cytometry. Data in (B) and (C) are means ± SEM (n = 3).

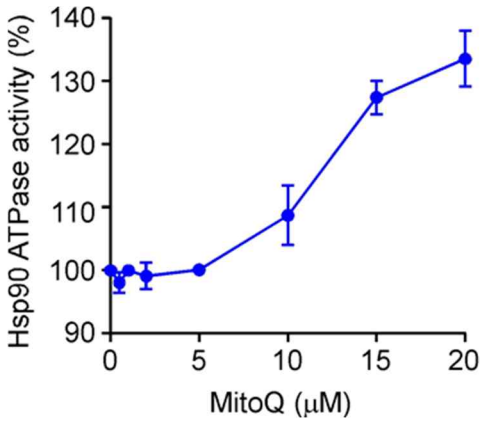

Figure 2.15. Measurement of Hsp90 ATPase activity in the presence of MitoQ. ATP hydrolysis by Hsp90 was measured in the presence of MitoQ as indicated.

2.3.10. MitoQ is a potent inhibitor of TRAP1 activity in cancer cells.

Most previously reported TRAP1 inhibitors with sub-micromolar cellular activity are ATP-mimic Hsp90 inhibitors (geldanamycin and PU-H71) conjugated with TPP such as gamitrinib, SMTIN-P01, and SMTIN-C10 (Figure 2.17.A).[15,18-20] Compared with these, MitoQ and SMTIN-C10 displayed more potent TRAP1 inhibition in 22Rv1 cells, based on the reduction of SDHB and SIRT3, and the increase in phosphor-AMPK and CHOP (Figure 2.17.B). Consistently, MitoQ and SMTIN-C_{10} potently disrupted the mitochondrial membrane potential (TMRM staining) and elevated ROS production (Mito-SOX staining; Figure 2.17.C), and consequently induced mitochondrial fragmentation and elevated cytoplasmic calcium levels in cancer cells (Figure 2.17.D). Similarly, MitoQ and SMTIN-C10 exhibited more potent cytotoxic activity, specifically toward various cancer cells; however, cytotoxicity of SMTIN-C_{10} toward normal cells (HFF-1 and mouse primary hepatocytes) was strongest among the examined drugs (Table 2.2), suggesting relatively strong non-specific cytotoxic activity for SMTIN-C_{10}. Thus, we concluded that MitoQ has the most potent cancer-specific cytotoxicity among the examined TRAP1 inhibitors, and 22Rv1 cells were more easily killed by MitoQ than by the other drugs (Table 2.2). Mitochondrial accumulation, driven by the TPP moiety,[15] and subsequent inhibition of mitochondrial function (IC50=0.6 μM, 2 h; Figure 2.18) resulted in potent cytotoxic activity in 22Rv1 (IC50=0.2 μM, 24 h; Table 2.2).

Since antioxidant activity can contribute to anticancer activity,[37] we synthesized MitoQ derivatives (SB-U011, SB-U014, and SB-U015) in which the ubiquinone moiety was modified to completely block the redox reaction (Figure 2.16.A). SB-U011 showed robust elevation at ~2 μM and complete inhibition at 15 μM in TRAP1 ATPase activity assays, similar to TPP-14 and -16, unlike MitoQ (Figure 2.16.B). Meanwhile, SB-U014 and SB-U015 showed gradual activation of ATPase activity up to 20 μM, similar to MitoQ (Figure 2.16.B). The redox-crippled drugs showed client degradation activity (Figure 2.16.C) and cytotoxicity toward cancer cells comparable to that of MitoQ (Tables 2.3); specifically, SB-U015 exhibited about 2-fold higher cancer cell-specific cytotoxicity than MitoQ. The results further confirm that TRAP1 inhibition, but not antioxidant function, is essential for the anticancer activity of MitoQ.

2.3.11. In vivo anticancer activities of MitoQ, SB-U014, and SB-U015.

To examine in vivo anticancer activities, 22Rv1-xenografted nude mice were administered with MitoQ intraperitoneally. MitoQ significantly reduced the growth of established tumors (Figure 2.19.A-B), and tumors collected from MitoQ-treated mice showed clear signs of TRAP1 inhibition, such as elevated expression of phosphor-AMPK and CHOP, and reduction of TRAP1 client proteins SDHB and SIRT3 (Figure 2.19.C-D), indicating that the mode of action of MitoQ is the same in vivo and in vitro. MitoQ

showed reduced Ki-67 and increased TUNEL-positive cells in tumors compared with vehicle (DMSO) treatment, suggesting a reduction in cell proliferation and an increase in cell death by MitoQ (Figure 2.19.E-F). Similarly, MitoQ derivatives lacking antioxidant activity (SB-U014 and SB-U015) showed not only comparable in vivo anti-tumor activity to MitoQ (Figure 2.16.D-E), but also clear signs of TRAP1 inhibition indistinguishable from MitoQ (Figure 2.16.F-G).

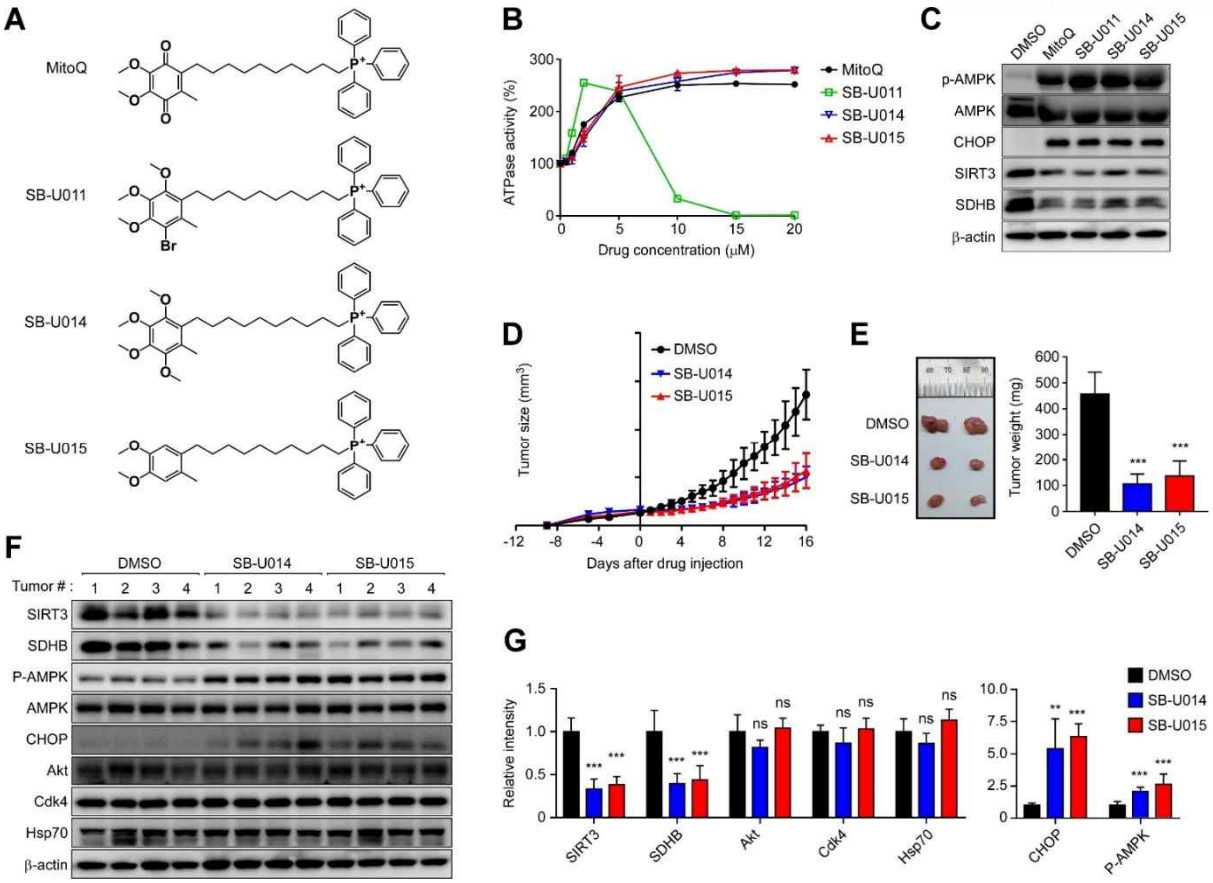

Figure 2.16. TRAP1 inhibitory activity of SB-series in vitro and in vivo.

(A) Chemical structures of MitoQ and its derivatives (SB-U011, SB-U014, and SB-U015) with crippled redox activity. (B) Drug effects on TRAP1 ATPase activity. (C) Cellular TRAP1 inhibition. 22Rv1 cells were treated with 5 μM drug for 2 h and analyzed by western blotting. (D) Tumor growth suppression in vivo. 22Rv1 cells were subcutaneously injected into both planks of nude mice (six mice/group). After tumors were established (day 0), vehicle (DMSO), SB-U014 (3 mg/kg), and SB-U015 (3 mg/kg) were intraperitoneally injected daily. Tumor size was measured with calipers. (E) Collected tumors (12 tumors/group). At the end of xenograft experiments in (D), tumors were collected, imaged (left), and weighed (right). (F) Western blotting analysis of tumors. Collected tumors in (E) were analyzed by western blotting. (G) Quantification of client protein expression. Band intensity in (F) was quantified by ImageJ and compared for each sample. Data in (B), (D), (E), and (G) are means ± SEM (n = 6). **p < 0.01; ***p < 0.001; ns, not significant.

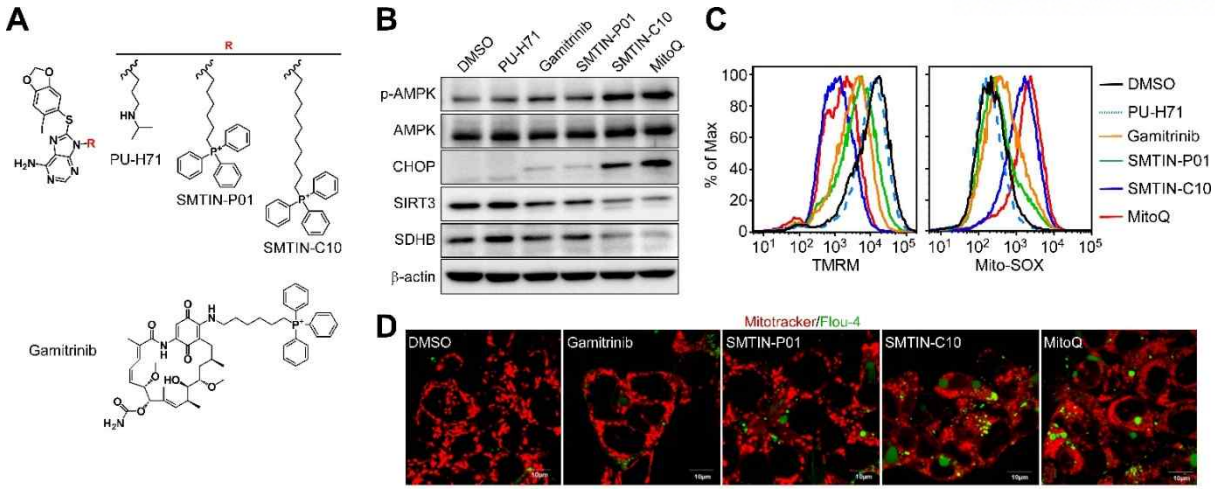

Figure 2.17. Comparison of TRAP1 inhibitory activity of MitoQ with TPP-conjugates targeting the ATP binding site of TRAP1.

(A) The reported TRAP1-specific (mitochondria-accumulating) inhibitors targeting the ATP binding pocket. (B) Cellular TRAP1 inhibition. 22Rv1 cells were incubated with 5 μM drug for 2 h and analyzed by western blotting. (C) Mitochondrial membrane potential and ROS production. 22Rv1 cells labeled with TMRM (left) or Mito-SOX (right) were incubated with 5 μM drug for 2 h and analyzed by flow cytometry. (D) Mitochondrial fragmentation and calcium discharge after TRAP1 inhibition. 22Rv1 cells labeled with MitoTracker and fluo-4 were incubated with 5 μM drug for 2 h and analyzed by confocal microscopy.

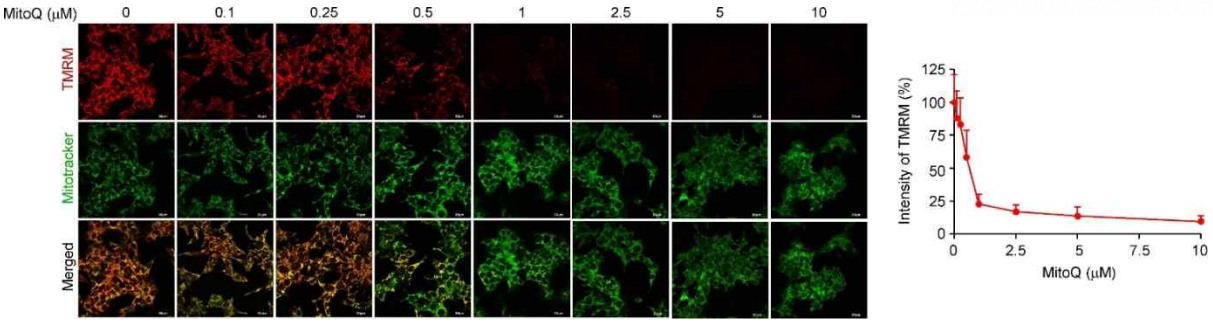

Figure 2.18. Mitochondrial membrane potential change after TRAP1 inhibition.

TMRM (red) and mitotracker (green) labeled 22Rv1 cells were incubated for 2 h with MitoQ as indicated concentration and analyzed by confocal microscope (left). The intensity of TMRM fluorescence (n=3) was quantified by ImageJ (NIH) and compared (right). IC50 value (μM) was calculated as 0.61 ± 0.03 using GraphPad Prism.

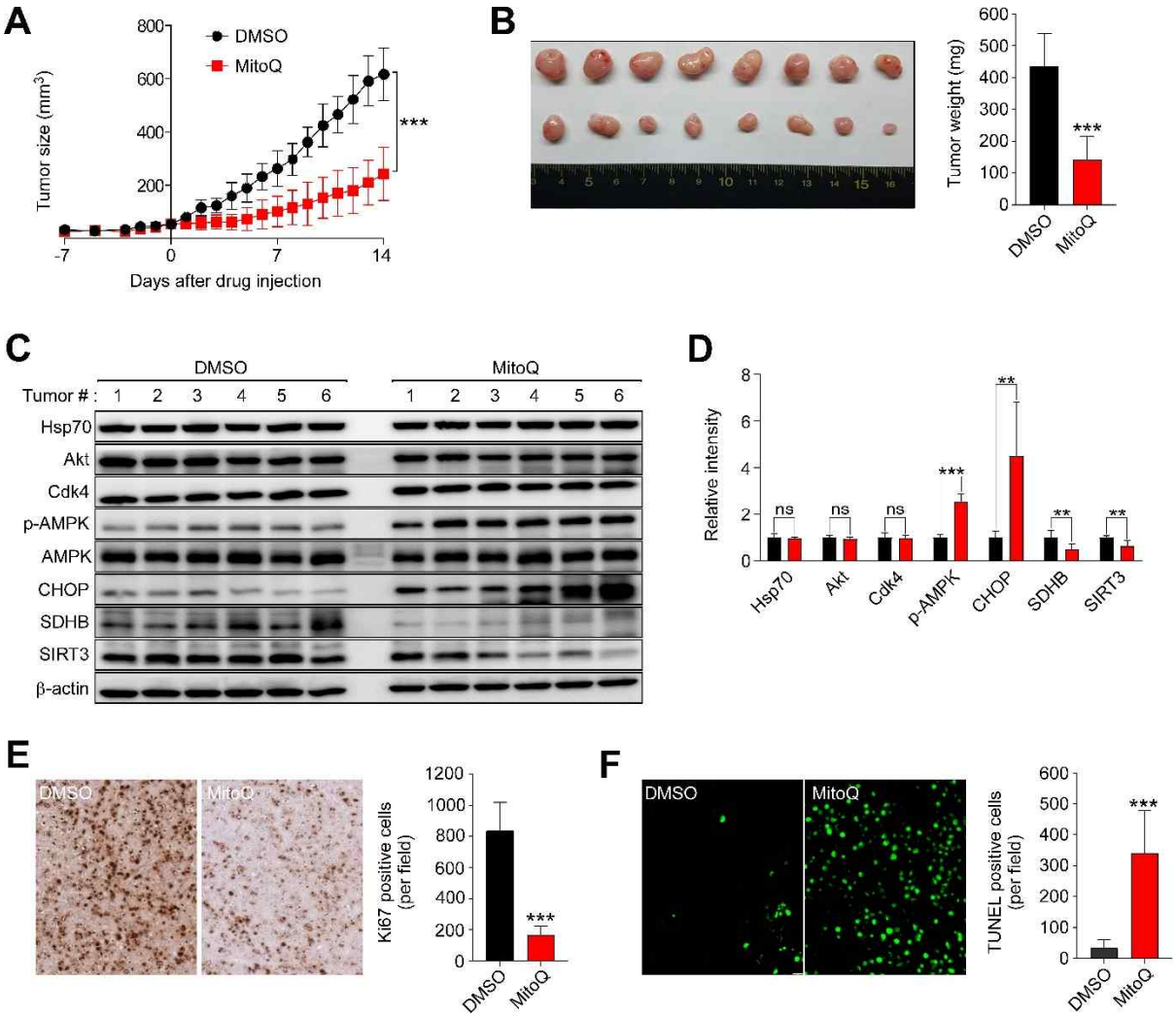

Figure 2.19. In vivo anticancer activities of MitoQ.

(A) Tumor growth. 22Rv1 cells were subcutaneously injected into both planks of nude mice (five mice/group). After tumors were established (Day 0), vehicle (DMSO) and MitoQ (3 mg/kg) were intraperitoneally injected daily. Tumor size was measured with calipers. (B) Tumor size. Collected tumors (10 tumors/group) were imaged (left) and weighed (right). (C) Mode of action of MitoQ. Tumor samples collected in (B) were analyzed by western blotting. (D) Quantification of band intensity. Western blotting data (n = 6) in (C) were quantified by ImageJ and compared between groups. (E) Ki-67 staining. Tumor specimens were analyzed by immunohistochemical staining (left). The number of Ki-67+ cells per field (n = 8) was counted. (F) Cell death induction. Tumor specimens were analyzed by TUNEL staining (left). The number of TUNEL+ cells per field (n = 6) was counted (right). Data in (A), (B), (D), (E), and (F) are means ± SEM. ***$p < 0.0001$; **$p < 0.009$; ns, not significant.

2.4. Discussion

MitoQ induced global structural changes in the TRAP1 dimer from open to closed conformations, similar to AMPPNP, consistent with the indistinguishable SAXS curves. However, the local conformation differed markedly from the AMPPNP-bound structure, especially around the region where MitoQ docks, including loss of inter-protomer MD–MD interactions, partial disordered structures in SMD and CTD, and an enlarged binding cavity between the two protomers. These MitoQ-triggered structural transitions may be necessary for both accommodating client proteins and for proper chaperone functions upon docking of client proteins, including regulating ATPase activity and interactions with modulators known as cochaperones in mitochondria.

Interestingly, post-translational modifications (PTMs) important in regulating chaperone activity, including S-nitrosylation and phosphorylation, are reportedly associated with SMD, which experiences extensive structural changes upon binding the client mimic MitoQ. The structural changes include the S-nitrosylation site Cys 501 (to avoid confusion, hereafter, all residue numberings refer to human TRAP1), one of the Cys residues participating in disulfide bond formation,38 and the phosphorylation sites Ser 511 and Ser 568,39 which are located at the N-terminal side of the MitoQ-triggered unwinding α-helix (residues 510-519) in SMD and the flexible loop (residues 554-572; no electron density in X-ray crystal structures) connecting SMD and CTD, respectively. Therefore, these PTMs may fine-tune binding and/or binding preferences toward client proteins through restructuring the client binding cleft, which may also affect TRAP1 interactions with cochaperones.

We selected eight TRAP1 interactors, and divided them into two different groups depending on their stability after TRAP1 inhibition. Glutaminase (GLS), thioredoxin-dependent peroxide reductase (PRDX3), single-strand DNA-binding protein 1 (SSBP1), and NADH-ubiquinone oxidoreductase 75 kDa subunit (NDUFS1) were degraded similarly to the reported TRAP1 client proteins SDHB and SIRT3; by contrast, ATP synthase subunit β (ATP5F1B), fumarate hydratase (FH), Lon peptidase 1 (LONP1), and Hsp60 (HSPD1) were not affected by TRAP1 inhibition. The interactors degraded after TRAP1 inhibition can be considered as TRAP1 client proteins. However, the non-degrading interactors could be modulators affecting TRAP1 chaperone activity (such as the protease LON peptidase and the chaperone Hsp60), client proteins for which functions (activity), but not protein stability, might be regulated by TRAP1, or simply co-purified proteins with other direct TRAP1 interactors. Regardless, compared with previous interactome analyses using TRAP1 inhibitors (client degradation) and affinity purification (pull-down and immunoprecipitation),[40-41] affinity purification combined with specific elution of the bound proteins in the present study is likely to reduce false positives, and also enrich

some TRAP1 modulators, in addition to clients, by triggering structural transition of TRAP1 to a modulator binding-incompetent conformation. However, the binding site for potential TRAP1 modulators remains to be determined.

Among 103 mitochondrial TRAP1 interactors identified in this study, only 29 proteins overlapped with 122 proteins identified previously.40-41 Thus, 74 proteins were newly identified as TRAP1 interactors in this study. This enabled us to predict novel functions for TRAP1. For example, TRAP1 supports high glutamine catabolism (a metabolic hallmark of many cancer cells) through chaperoning glutaminase, the enzyme catalyzing the first cellular step of glutaminolysis.[42-43] TRAP1 may also participate in the maintenance and expression of the mitochondrial genome, which could be related not only to mitochondriotoxic effects upon TRAP1 inhibition, but also TRAP1-dependent rewiring of mitochondrial metabolism in cancer cells.[4, 44] Therefore, extensive analysis of the interactome using MitoQ and its derivatives, in a variety of cell types, and under diverse sets of signaling and stress conditions, could reveal novel mitochondrial functions and regulatory mechanisms of TRAP1.

In terms of drug specificity and efficacy, MitoQ targeting the client binding site has many advantages over current TRAP1 and Hsp90 inhibitors targeting the ATP binding site. Firstly, TRAP1 and Hsp90 are members of the GHKL superfamily of ATPase/kinases, and structurally similar due to the Bergerat ATP binding fold.[45] Thus, there have been many concerns about off-target effects of Hsp90 inhibitors targeting the highly conserved structures shared by functionally important GHKL members as well as Hsp90 family proteins.[13] However, MitoQ and SB-series drugs could avoid this by targeting the structurally unique client binding site, which differs significantly even between Hsp90 family proteins. Secondly, Hsp90 family proteins generally require ATP hydrolysis for their chaperone functions, but TRAP1 also displayed holdase-type chaperone activity for certain client proteins, which does not require ATP hydrolysis. For example, PU-H71 strongly interacted with the ATP binding site of TRAP1 but did not inhibit chaperone functions, such as activating SIRT3 deacetylase activity. The groups of Picard and Necker also reported that inhibiting the ATPase cycle of TRAP1 could not fully inactivate its chaperone activity.[40] Consistently, the client binding site inhibitors achieved the most potent TRAP1 inhibition activity in vitro and in vivo in the present study, presumably through blocking the essential holdase function of TRAP1. Although ATP dependency needs to be further investigated to understand the chaperone mechanism of action, targeting the client binding site directly and thereby compromising holdase activity seems to be a better strategy for the development of potent TRAP1 inhibitors compared with targeting the traditional ATP binding site.

Thirdly, current Hsp90 inhibitors targeting the ATP binding site inevitably trigger a pro-survival adverse response, as exemplified by induction of heat shock proteins including Hsp70, which is also used as a pharmacodynamic marker of Hsp90 inhibition.[14, 21] This adverse effect seems to be specific

to ATP-competitive Hsp90 inhibitors because non-ATP-competitive inhibitors, such as novobiocin and its derivatives, did not elevate Hsp70.[46-47] Similar to novobiocin, MitoQ was able to inhibit Hsp90 to degrade its client proteins without this adverse Hsp70 induction (Figure 2.14.C-D). Thus, targeting the client binding site could overcome the fundamental limitations of ATP-competitive Hsp90 drugs.

Some TPP-antioxidant conjugates, including MitoQ, possess anticancer activity,[48-51] which has been attributed to their antioxidant activity since mitochondrial ROS regulate various aspects of tumorigenesis and survival of cancer cells.[37] However, many reports have demonstrated overproduction of ROS and subsequent mitochondrial dysfunction in cancer cells after treatment with TPP-antioxidants, rather than scavenging ROS or protecting mitochondrial functions,[48, 52] consistent with the results of the present study. Furthermore, MitoQ derivatives (SB-U011, SB-U014, and SB-U015) lacking antioxidant activity achieved comparable TRAP1 inhibition and consequent cytotoxic activity toward cancer cells, confirming that TRAP1 inhibition, but not antioxidant activity, is crucial for the anticancer activity of MitoQ. Thus, the pharmacological activity of various TPP-antioxidants and other TPP-conjugates intended for efficient mitochondrial drug delivery 22 should be cautiously interpreted, with the possibility of TRAP1 inhibition, especially in cancer cells that often overexpress TRAP1 and are dependent on the function of this chaperone.

2.5. Conclusions

In this study, we identified a novel druggable client binding site in TRAP1 and discovered that MitoQ is a small molecule client mimic that binds this site. Structural analysis revealed that MitoQ interacts in an asymmetric bipartite manner with the client binding pocket located in MD of TRAP1. Consistently, MitoQ competed effectively for the binding of client proteins to TRAP1 and displayed more potent inhibitory activity than other inhibitors targeting the ATP pocket in NTD of TRAP1. The revealed molecular interaction not only makes the optimization of TRAP1-selective inhibitors feasible for improving anticancer activities, but may also be applicable for the development of potent inhibitors targeting various Hsp90 family proteins to treat a range of human diseases.

2.6. Materials and Methods

2.6.1. Antibodies and Reagents.

*A*nti-Phospho-AMPKα, anti-Cdk4, anti-CHOP, anti-GLS, anti-FH and anti-SIRT3 antibodies were purchased from Cell Signalling Technology; anti-Akt, anti-AMPK and anti-PRDX3 were purchased from Santa Cruz Biotechnology; anti-TRAP1, anti-Hsp60 (*HSPD1*) and anti-Hsp70 were purchased from BD Biosciences; anti-β-actin antibody was purchased from MP Biomedicals; anti-Ki67, anti-SDHB, anti-ATP5B (*ATP5F1B*), and anti-NDUFS1 were purchased from Abcam; anti-SSBP1 was purchased from Invitrogen; anti-LONP1 was purchased from Novus Biologicals. IHC kit (ab64264), SIRT3 activity assay kit (ab156067), and PiColor Gold Phosphate Detection kit were purchased from Abcam; RNeasy Plus Mini kit (74134) was purchased from QIAGEN; ProtoScript First Strand cDNA Synthesis kit (E6300) was purchased from New England Biolabs; SYBR qPCR Master Mix (RT500) was purchased from Enzynomics; Mitochondria isolation kit (89874) was purchased from Thermo Fisher Scientific; Monolith NT^{TM} Protein Labeling Kit RED-NHS (L001) was purchased from NanoTemper Technologies.

2.6.2. Chemicals.

Coenzyme Q_0 (20504) was purchased from Cayman; methyl-triphenylphosphonium bromide (130079), decylubiquinone (D7911), and Mito-TEMPO (SML0737) were purchased from Sigma; SkQ1 (HY-100474) and mitoquinone (HY-100116A) were purchased from MedchemExpress; butyl-triphenylphosphonium bromide (B0970) was purchased from TCI; ethyl-triphenylphosphonium bromide (B23096), (1-hexyl)-triphenylphosphonium bromide (A13826), (1-Octyl)-triphenylphosphonium bromide (L02412), (1-decyl)-triphenylphosphonium bromide (A11021), (1-dodecyl)-triphenylphosphonium bromide (A14295), (1-tetradecyl)-triphenylphosphonium bromide (L04311), and (1-hexadecyl)-triphenylphosphonium bromide were purchased from Alfa Aesar.

2.6.3. Cells and Culture Conditions.

Human cancer cell lines, Hela, 22Rv1, PC3, NCI-H460, U251, MDA-MB-231, and SK-HEP-1, and normal human skin fibroblast HFF-1 were purchased from the American Type Culture Collection

(ATCC) and were maintained as recommended by the supplier. Briefly, the cancer cells were cultured in a DMEM or RPMI medium (GIBCO) containing 10% fetal bovine serum (FBS; ATCC) and 1% penicillin/streptomycin (GIBCO) at 37 °C in a humidified atmosphere of 5% CO_2. HFF-1 was cultured in DMEM supplemented with 15% FBS and 1% penicillin/streptomycin at 37°C in a humidified atmosphere of 5% CO_2. Primary hepatocytes were prepared from 8 weeks old C57BL/6 mice as described previously.[1] Briefly, harvested livers from collagenase-perfused mice were dissected and filtered by a 100 μm cell strainer (BD Biosciences). The collected cells were washed several times with M199/EBSS medium (Hyclone), and hepatocytes were separated by gradient centrifugation with Percoll (Sigma). The isolated hepatocytes were resuspended and maintained in M199/EBSS medium containing 10% FBS at 37°C in a humidified atmosphere of 5% CO_2. To obtain ρ^0 cell, HeLa cells were treated for 2-3 weeks with low dosage (50 ng/ml) ethidium bromide (Sigma). Consequent mitochondria-depleted cells were maintained in DMEM containing 10% FBS, 1% penicillin/streptomycin, 50 μg/ml uridine (Sigma), and 1 mM sodium pyruvate at 37°C in a humidified atmosphere of 5% CO_2. The medium was changed every 2 days and cells were passaged upon reaching 70-90% confluency.

2.6.4. Analysis of Cell Viability.

Cells were incubated with 3-(4,5-dimethyl-thyzozl-2-yl)-2,5-diphenyltetrazolium bromide (MTT) for 4 h, and crystallized formazan was dissolved by DMSO and quantified by measuring absorbance at 595nm using a SYNERGY NEO microplate reader (BioTek Instruments, Inc.). Absorbance data were normalized to the DMSO and presented as percent viability. IC_{50} was determined at least from two independent measurements.

2.6.5. Measurement of Mitochondrial Superoxide, Membrane Potential, and Calcium.

Cells were labeled with 200 nM Mito-SOX red (Invitrogen) or 200 nM TMRM (Invitrogen) in the presence of Sytox (Invitrogen) for 20 min, and analyzed by flow cytometry with FACS Calibur™ system (BD Biosciences). The collected data from Sytox negative cells were analyzed. To measure induction of cell death, cells were labeled with Sytox for 20 min, and analyzed by flow cytometry with FACS Calibur™ system. The collected data were analyzed using the FlowJo software (TreeStar). To measure intracellular calcium, 22Rv1 Cells were incubated with 5 μM Fluo4-AM (Invitrogen) and 100 nM Mitotracker (Invtirogen) for 30 min at 37°C and 5% CO_2. After washing with fresh RPMI medium, cells were analyzed under a FV1000 confocal microscope (Olympus).

2.6.6. Western Blot Analysis.

Cell lysates were separated by SDS-PAGE, and transferred onto a PVDF membrane. The membranes were blocked with 10% skim milk in TBST (TBS containing 0.05% Tween-20) for 1 h at room temperature and incubated with primary antibodies overnight at 4°C. Membranes were washed three times with TBST for 1 h and incubated with the secondary antibodies diluted for 1 h in 10% skim milk in TBST (1:5000). The membranes were washed three times with TBST and visualized using an enhanced chemiluminescence detection kit (BioRad).

2.6.7. Preparation of Recombinant Proteins and Fluorescence Polarization Assays.

The genes encoding zTRAP1, hTRAP1, Hsp90, and SIRT3 were cloned into a modified pET-Duet vector with an N-terminal hexa-histidine tag followed by a TEV protease cleavage site, and expressed in *E. coli* BL21 (DE3) cells. After 15 h post-induction with 0.4 mM IPTG at 20 °C, cells were harvested and lysed via sonication. The soluble fraction of the lysates applied to Ni^{2+} affinity chromatography column (GE Healthcare). The hexa-histidine tag was cleaved by TEV protease, and the protein were purified further by gel-filtration chromatography in a buffer containing 25 mM Tris-HCl pH 7.5, 150 mM NaCl, 5 mM β-mercaptoethanol (β-ME). For fluorescence polarization assay, purified recombinant TRAP1 (400 nM) was incubated with the fluorescent probe PU-H71-FITC (10 nM) synthesized as described previously [2] in the presence of increasing concentrations of inhibitors for 2 h at room temperature. Fluorescence polarization was measured by using microplate reader (Synergy NEO, BioTek).

2.6.8. ATPase Activity Assay.

The ATPase activity of TRAP1 was measured using a PiColorLock Gold Phosphate Detection Kit (Abcam). 0.5 μM TRAP1 (wild type or mutant) was pre-incubated with various concentration of inhibitors for 30 min and then incubated with 0.2 mM ATP for 3 h at 37°C in an ATPase activity assay buffer containing 50 mM Tris-HCl, 20 mM KCl, and 6 mM $MgCl_2$ (pH 7.4). Next, 20 μL of PiColorLock Gold reagent and the accelerator mixture (100:1) were added to each sample (100μL). After 5 min incubation, 10 μL of stabilizer was added to stop color development. The absorbance was measured at 620 nm using a microplate reader (Synergy NEO, BioTek). The absorbance of the unreacted sample was subtracted to normalize the background signal.

2.6.9. Structure Determination.

The purified zTRAP1 was mixed with AMPPNP in a 1:1.5 molar ratio. The crystallization was performed as previously described.[3] After the crystals were grown, 0.1 mM MitoQ was added to the crystallization drop and incubated for 24 h. For X-ray diffraction experiments, crystals were transferred to a well solution containing 20% glycerol and flash-frozen in liquid nitrogen. The diffraction data were collected at a 5C beam line at the Pohang Accelerator Laboratory (PAL) and processed using HKL-2000 software.[4] The electron density for MitoQ was calculated by a difference Fourier method. The model building and refinement were carried out by Coot and Phenix program,[5, 6] respectively (Table 2.4).

2.6.10. Small Angle X-ray Scattering (SAXS) Analysis.

50 μM TRAP1 (wild type or mutant) in 50 mM Tris, 20mM KCl, 6 mM $MgCl_2$, and 1mM DTT (pH 7.4) was incubated with 50 μM inhibitors or 2 mM AMP-PNP for 1 h at 37°C. Data were collected at the 6D beamline of the Pohang Accelerator Laboratory (PAL). The sample-to-detector distance was 3,003 mm, and the X-ray energy was 11.6 keV. The scattered X-rays were analyzed with a CCD area detector (MX-225HS, Rayonix LLC). The scattering data were transformed to P(r) vs r using BayesApp server.[7]

2.6.11. Microscale Thermophoresis (MST) Binding Assay.

The MST experiments were performed using a Monolith NT.115 instrument (NanoTemper). Purified proteins were labeled with the Monolith NT™ Protein Labeling Kit RED-NHS (Amine-reactive; NanoTemper Technologies) according to the manufacturer's protocol. The determination of the apparent K_D values of proteins and inhibitors were performed by using a constant amount of 200 nM labeled proteins in a buffer containing 50mM Tris-HCl, 20 mM KCl, and 6 mM $MgCl_2$ (pH7.4) in the presence of increasing concentrations of inhibitors ranging from 6.1 nM to 200 μM. These mixtures were incubated for 3 h at 37°C in the data. Subsequently, thermophoresis of each concentration was measured using the Monolith NT.115 (NanoTemper Technologies). The measurement was independently repeated three times.

2.6.12. Proteomics Analysis.

Precleared mitochondrial protein extracts (1 mg) from 22Rv1 and Hela cells were incubated overnight at 4°C with GST and GST-TRAP1 beads. Bead-bound proteins were collected by centrifugation at 1,000 rpm for 1 min at 4°C, washed three times with the Lysis buffer, and eluted by incubating with 50μM MitoQ for 4 h at 4°C. The eluted proteins were analyzed by LC-MS/MS analysis as previously reported.[8] Briefly, the eluted proteins were separated by SDS-PAGE and the gel was divided into 10 mm sections and subjected to in-gel digestion with trypsin. The tryptic digests were separated by online reversed-phase chromatography using a Thermo Scientific Easy nano LC 1200 UHPLC equipped with an autosampler using a reversed-phase peptide trap Acclaim PepMap™ 100 (75 μm inner diameter, 2 cm length) and a reversed-phase PepMap™ RSLC C18 analytical column (75 μm inner diameter, 15cm length, 3 μm particle size), both from Thermo Scientific, followed by electrospray ionization at a flow rate of 300 nl/min. The chromatography system was coupled in line with an Orbitrap Fusion Lumos mass spectrometer. Comparative analysis of proteins identified in this study was performed in Scaffold4.

2.6.13. Pull Down Experiment.

GST and GST-TRAP1 proteins were induced in *E.coli* BL21 overnight with 0.2 mM IPTG at 18°C. Cells were harvested by centrifugation and lysed by sonication in Lysis buffer (50 mM Tris-HCl, pH 7.4, 150 mM NaCl, 5 mM $MgCl_2$, and 1 mM dithiothreitol). After centrifugation at 13,000 rpm for 30 min, the soluble fractions were mixed with glutathione-Sepharose beads (GE Healthcare). Protein-bound beads were washed three times with a wash buffer (50 mM Tris-HCl, 500 mM NaCl, 5 mM $MgCl_2$, and 1 mM dithiothreitol, pH 7.4). Mitochondria were isolated using a Mitochondria Isolation Kit (Thermo Fisher Scientific). Mitochondria isolated from 22Rv1 cells were lysed for 1 h at 4°C in RIPA buffer (50 mM Tris-HCl, 150mM NaCl, 1% NP-40, 0.25% sodium deoxycholate) with proteinase inhibitor (Invitrogen) under constant agitation. After centrifugation at 13,000 rpm for 5 min at 4°C, the supernatant was precleared for 1 h at 4°C with glutathione beads. Then, 100 μg of precleared protein extract was then incubated overnight at 4°C with GST and GST-TRAP1 beads. Bead-bound proteins were collected by centrifugation at 1,000 rpm for 1 min at 4°C, washed three times with Lysis buffer, and analyzed by western blot.

2.6.14. Measurement of Deacetylase Activity of SIRT3.

The enzyme activity of SIRT3 was determined using the SIRT3 Activity Assay Kit (Abcam), according to the manufacturer's instructions. Briefly, the assays were performed by incubating the recombinant SIRT3 proteins and Fluoro-Substrate Peptide, Developer, NAD, and inhibitors with or without TRAP1 at 37°C for 30 min. Fluorescent was measured immediately after initiation of the reaction at the excitation and emission wavelength of 355nm and 460nm, respectively, using a microplate reader (Synergy NEO, BioTek). Enzyme activity was calculated from the slope of the linear part of the fluorescence progress curve.

2.6.15. RNA Extraction and qPCR.

Total RNA was prepared using RNeasy Mini Kits (QIAGEN) according to the manufacturer's instructions, and cDNA was synthesized from the RNA using the ProtoScript First Strand cDNA Synthesis Kit (New England Biolabs, E6300) with an oligo(dT) primer. Real time quantitative PCR (qPCR) was used to analyze the cDNA with the LightCycler 480 II (Roche Applied Sciences, Indianapolis, IN). The resulting cycle threshold cycle (C_t) values were normalized with β-actin and expressed as fold change over control samples.

2.6.16. qPCR primers.

Gene	Sequence (5'→3')	
SIRT3	Forward	CAGTCTGCCAAAGACCCTTC
	Reverse	AAATCAACCACATGCAGCAA
SDHB	Forward	GGAAGGCAAGCAGCAGTATC
	Reverse	AGCGATAGGCCTGCATAAGA
GLS	Forward	GCTGTGCTCCATTGAAGTGA
	Reverse	GCAAACTGCCCTGAGAAGTC
FH	Forward	TCCAGGCCAATACAGAAAGG
	Reverse	ACCCATTCGTCAAACTGCTC

NDUFS1	Forward	GTGACCAGGGAGGTGAATGT
	Reverse	CAAACCTGATGCAGCGAGTA
ATP5F1B	Forward	GCACGGAAAATACAGCGTTT
	Reverse	TTGCCACAGCTTCTTCAATG
SSBP1	Forward	GCGATCAGGGGATAGTGAAG
	Reverse	TTGCTTGTCGCCTCACATTA
LONP1	Forward	CGGGAAGATCATCCAGTGTT
	Reverse	ACGTCCAGGTAGTGGTCCAG
HSPD1	Forward	CACCGTAAGCCTTTGGTCAT
	Reverse	CTTCTCCAAACACTGCACCA
PRDX3	Forward	GCCGTTGTCAATGGAGAGTT
	Reverse	TCCACTGAGACTGCGACAAC
β-*Actin*	Forward	AGAGCTACGAGCTGCCTGAC
	Reverse	AGCACTGTGTTGGCGTACAG
TRAP1	Forward	AGCGCACTCATCAGGAAACT
	Reverse	TCAAACTCACGAAGGTGCAG

2.6.17. *In vivo* Mouse Xenograft.

Immune-deficient athymic nude mice (male, 8-week-old) were purchased from OrientBio. They were maintained in the pathogen-free facility at the UNIST In Vivo Research Center (12 h dark/light cycle) and fed with standard diet and water. All animal experiments were approved by UNIST (UNISTIACUC-19-11). 22Rv1 cells (1×10^7) were injected subcutaneously into both flanks of the nude mice. When the tumor size reached approximately 100 mm^3, vehicle (DMSO) and 3 mg/Kg drug (MitoQ, SB-U014, and SB-U015) dissolved in 20% cremophor EL (Sigma) in PBS were administered intraperitoneally daily. Tumor volume was measured daily using electronic calipers and was calculated using the following formula: $V = 1/2 \times (width)^2 \times length$. At the end of the experiment, animals were euthanized

and tumors were collected for histology and western blot. The band intensity was quantified using ImageJ software (National Insutitute of Health, USA).

2.6.18. Crosslinking Experiments.

Purified recombinant TRAP1 (3 μM) was incubated with 2 mM AMP-PNP or various concentrations of drugs at 37°C for 3 hr, alternatively at 51°C for 5 min, followed by cooling at room temperature for another 5 min. The proteins were crosslinked with 0.005% glutaraldehyde at 4°C for 5 min and analyzed by SDS-PAGE.

2.6.19. Cellular Thermal Denaturation of TRAP1.

TRAP1 destabilization induced by the drugs targeting the client binding site was analyzed after thermal stress in cancer cells. Briefly, cells at 80% confluency (6 well plate) were treated with various concentrations of drugs for 30 min. The cells were detached by trypsin, collected by centrifugation, and subsequently resuspended in PBS. The resuspended cells were aliquoted into PCR tubes and heated at 51°C for 5 min, followed by cooling at room temperature for another 5 min. Subsequently, cells were disrupted by 3 freeze-thaw cycle with liquid nitrogen. Precipitated proteins were removed by centrifugation at 13,000 rpm at 4°C for 20 min. Soluble proteins in the supernatant fraction were collected, and analyzed by western blotting. The amount of proteins was quantified by densitometry analyses using the ImageJ software. The measurement was repeated three times independently.

2.6.20. Immunohistochemical Analyses.

To analyze cell proliferation in xenograft model, tumors were harvested and fixed in 10% formalin at 4°C. Formalin-fixed paraffin-embedded tumor samples were sectioned for histological analysis. After paraffin removal, sections were incubated in 3% hydrogen peroxide to block endogenous peroxidase. Sections were incubated in antigen retrieval in citrate buffer and stained with the IHC kit (Abcam, ab64264) according to the manufacturer's instructions. In brief, after permeabilization and blocking, sections were incubated overnight at 4°C with anti-Ki67 antibody (Abcam, 1/2000). Staining was developed by DAB chromogen and analyzed using a virtual microscope (Olympus). To count apoptotic dead cells in the tumor samples, fragmented DNA was labeled via the TUNEL method using an in situ cell death detection kit (Roche) following the manufacturer's protocol. The labeled DNA was detected

immunohistochemically and visualized using an inverted fluorescence microscope (Olympus). The average numbers of TUNEL-positive nuclei were calculated in six fields selected from a central region of tumor, excluding the necrosis region.

2.6.21. Statistical analyses.

All data were presented as mean ± standard error of the mean (SEM) from at least two independent experiments. Statistical analyses were performed using Prism 7 (GraphPad Software). Two-tailed student's *t* tests were performed to compare distributions between different groups. The differences were considered statistically significant when $p < 0.05$.

Table 2.1. Cytotoxic activity of drugs. 22Rv1 and HFF-1 cells were treated with various concentrations of drugs for 24 h and analyzed by MTT assay. Data are means ± SEM from duplicate independent experiments.

Substance	Cytotoxic activity (IC_{50}, μM)	
	22Rv1	HFF-1
MitoQ	0.19 ± 0.01	13.36 ± 0.19
SkQ1	0.46 ± 0.05	16.94 ± 0.04
Mito-CP	0.33 ± 0.04	13.81 ± 0.35
Mito-TEMPO	>20	>20
Mito-VitE	3.01 ± 0.28	>20
TPP-14	0.16 ± 0.01	5.12 ± 0.23
TPP-16	0.12 ± 0.01	5.20 ± 0.15

Table 2.2. Cytotoxic activity of MitoQ. Cancer and normal cells were incubated with various concentrations of drugs for 24 h and analyzed by MTT assay. Data (IC_{50}, μM) are means ± SEM from two independent experiments (n = 4).

Cell	PU-H71	Gamitrinib	SMTIN-P01	SMTIN-C10	MitoQ
Hela	>20	6.52 ± 0.19	7.57 ± 0.75	1.94 ± 0.06	1.27 ± 0.13
22Rv1	5.83 ± 0.90	1.09 ± 0.08	0.96 ± 0.05	0.25 ± 0.01	0.20 ± 0.01
MDA-MB-231	>20	6.00 ± 0.54	7.43 ± 0.26	1.93 ± 0.10	2.49 ± 0.23
PC3	>20	4.70 ± 0.11	7.87 ± 0.16	1.50 ± 0.03	0.71 ± 0.06
U251	>20	6.62 ± 0.46	6.94 ± 0.33	1.75 ± 0.10	1.33 ± 0.29
SK-HEP-1	1.23 ± 0.29	3.81 ± 0.11	4.52 ± 0.09	0.85 ± 0.00	1.02 ± 0.37
NCI-H460	>20	11.03 ± 0.28	13.13 ± 0.79	2.42 ± 0.11	3.56 ± 0.35
Hepatocyte	>20	>20	>20	3.74 ± 0.03	>20
HFF-1	>20	17.18 ± 0.66	15.22 ± 0.34	7.12 ± 0.23	13.30 ± 0.26

Table 2.3. Cytotoxic activity of MitoQ.. Cells were incubated with various concentrations of drugs for 24 h and analyzed by MTT assay. Data (IC_{50}, μM) are means ± SEM from two independent experiments (n = 5).

Cell	SB-U011	SB-U014	SB-U015
Hela	1.12 ± 0.09	1.09 ± 0.03	0.89 ± 0.05
22Rv1	0.14 ± 0.01	0.16 ± 0.01	0.11 ± 0.01
HFF-1	6.37 ± 0.13	7.97 ± 0.14	12.56 ± 0.16

Table 2.4. Data collection and refinement statistics

	zTRAP1–MitoQ–AMPPNP
X-ray source	Beamline 7A, PAL
Temperature (K)	100
Space group:	C2
Cell parameters	
a, b, c (Å)	179.339, 96.522, 125.615
α, β, γ (°)	90.000, 134.394, 90.000
Data processing	
Wavelength (Å)	0.97934
Resolution (Å)	50.00 - 2.30
R_{merge} (%)	8.8 (42.4)
I/σ	21.0 (1.9)
Completeness (%)	99.0 (95.2)
Redundancy	5.5 (3.4)
Measured reflections	369974
Unique reflections	67378
Refinement statistics	
Resolution (Å)	31.205 - 2.297
Reflections	67368
Number of atoms	
Protein	9697
Water	221
Ligand/ion	73
R-factor (%)	19.53
R_{free} (%)	24.12
RMSD	
Bond lengths (Å)	0.008
Bond angles (°)	1.404
B-factors (Å^2)	
Protein	42.6
Waters	49.2
Ligand/ion	55.1
Ramachandran plot, residues in	
Favored regions (%)	95.8
Allowed regions (%)	4.2
Disallowed regions (%)	0.0

*Highest resolution shell is shown in parenthesis.

2.7. References

1. Jaeger, A. M.; Whitesell, L., HSP90: Enabler of Cancer Adaptation. Annual Review of Cancer Biology 2019, 3 (1), 275-297.

2. Sanchez-Martin, C.; Serapian, S. A.; Colombo, G.; Rasola, A., Dynamically Shaping Chaperones. Allosteric Modulators of HSP90 Family as Regulatory Tools of Cell Metabolism in Neoplastic Progression. Frontiers in Oncology 2020, 10.

3. Schopf, F. H.; Biebl, M. M.; Buchner, J., The HSP90 chaperone machinery. Nat Rev Mol Cell Biol 2017, 18 (6), 345-360.

4. Rasola, A.; Neckers, L.; Picard, D., Mitochondrial oxidative phosphorylation TRAP(1)ped in tumor cells. Trends in cell biology 2014, 24 (8), 455-63.

5. Kang, B. H.; Altieri, D. C., Compartmentalized cancer drug discovery targeting mitochondrial Hsp90 chaperones. Oncogene 2009, 28 (42), 3681-8.

6. Park, H. K.; Hong, J. H.; Oh, Y. T.; Kim, S. S.; Yin, J.; Lee, A. J.; Chae, Y. C.; Kim, J. H.; Park, S. H.; Park, C. K.; Park, M. J.; Park, J. B.; Kang, B. H., Interplay between TRAP1 and Sirtuin-3 Modulates Mitochondrial Respiration and Oxidative Stress to Maintain Stemness of Glioma Stem Cells. Cancer Res 2019, 79 (7), 1369-1382.

7. Park, H. K.; Lee, J. E.; Lim, J.; Kang, B. H., Mitochondrial Hsp90s suppress calcium-mediated stress signals propagating from mitochondria to the ER in cancer cells. Molecular cancer 2014, 13, 148.

8. Park, H. K.; Lee, J. E.; Lim, J.; Jo, D. E.; Park, S. A.; Suh, P. G.; Kang, B. H., Combination treatment with doxorubicin and gamitrinib synergistically augments anticancer activity through enhanced activation of Bim. BMC cancer 2014, 14, 431.

9. Masgras, I.; Sanchez-Martin, C.; Colombo, G.; Rasola, A., The Chaperone TRAP1 As a Modulator of the Mitochondrial Adaptations in Cancer Cells. Front Oncol 2017, 7, 58.

10. Trepel, J.; Mollapour, M.; Giaccone, G.; Neckers, L., Targeting the dynamic HSP90 complex in cancer. Nature reviews. Cancer 2010, 10 (8), 537-49.

11. Neckers, L.; Trepel, J. B., Stressing the development of small molecules targeting HSP90. Clinical cancer research : an official journal of the American Association for Cancer Research 2014, 20 (2), 275-7.

12. Gewirth, D. T., Paralog specific Hsp90 Inhibitors - a brief history and a bright future. Curr Top Med Chem 2016, 16 (25), 2779-91.

13. Neckers, L.; Blagg, B.; Haystead, T.; Trepel, J. B.; Whitesell, L.; Picard, D., Methods to validate Hsp90 inhibitor specificity, to identify off-target effects, and to rethink approaches for further clinical development. Cell Stress Chaperones 2018, 23 (4), 467-482.

14. Park, H. K.; Yoon, N. G.; Lee, J. E.; Hu, S.; Yoon, S.; Kim, S. Y.; Hong, J. H.; Nam, D.; Chae, Y. C.; Park, J. B.; Kang, B. H., Unleashing the full potential of Hsp90 inhibitors as cancer therapeutics through simultaneous inactivation of Hsp90, Grp94, and TRAP1. Exp Mol Med 2020, 52 (1), 79-91.

15. Lee, C.; Park, H. K.; Jeong, H.; Lim, J.; Lee, A. J.; Cheon, K. Y.; Kim, C. S.; Thomas, A. P.; Bae, B.; Kim, N. D.; Kim, S. H.; Suh, P. G.; Ryu, J. H.; Kang, B. H., Development of a Mitochondria-Targeted Hsp90 Inhibitor Based on the Crystal Structures of Human TRAP1. Journal of the American Chemical Society 2015, 137 (13), 4358-67.

16. Park, H. K.; Jeong, H.; Ko, E.; Lee, G.; Lee, J. E.; Lee, S. K.; Lee, A. J.; Im, J. Y.; Hu, S.; Kim, S. H.; Lee, J. H.; Lee, C.; Kang, S.; Kang, B. H., Paralog Specificity Determines Subcellular Distribution, Action Mechanism, and Anticancer Activity of TRAP1 Inhibitors. J Med Chem 2017, 60 (17), 7569-7578.

17. Kang, B. H.; Plescia, J.; Song, H. Y.; Meli, M.; Colombo, G.; Beebe, K.; Scroggins, B.; Neckers, L.; Altieri, D. C., Combinatorial drug design targeting multiple cancer signaling networks controlled by mitochondrial Hsp90. The Journal of clinical investigation 2009, 119 (3), 454-64.

18. Kang, B. H., TRAP1 regulation of mitochondrial life or death decision in cancer cells and mitochondria-targeted TRAP1 inhibitors. BMB reports 2012, 45 (1), 1-6.

19. Bryant, K. G.; Chae, Y. C.; Martinez, R. L.; Gordon, J. C.; Elokely, K. M.; Kossenkov, A. V.; Grant, S.; Childers, W. E.; Abou-Gharbia, M.; Altieri, D. C., A Mitochondrial-targeted purine-based HSP90 antagonist for leukemia therapy. Oncotarget 2017, 8 (68), 112184-112198.

20. Hu, S.; Ferraro, M.; Thomas, A. P.; Chung, J. M.; Yoon, N. G.; Seol, J. H.; Kim, S.; Kim, H. U.; An, M. Y.; Ok, H.; Jung, H. S.; Ryu, J. H.; Colombo, G.; Kang, B. H., Dual Binding to Orthosteric and Allosteric Sites Enhances the Anticancer Activity of a TRAP1-Targeting Drug. J Med Chem 2020, 63 (6), 2930-2940.

21. Centenera, M. M.; Gillis, J. L.; Hanson, A. R.; Jindal, S.; Taylor, R. A.; Risbridger, G. P.; Sutherland, P. D.; Scher, H. I.; Raj, G. V.; Knudsen, K. E.; Yeadon, T.; Yeadon, T.; Tilley, W. D.; Butler, L. M., Evidence for Efficacy of New Hsp90 Inhibitors Revealed by Ex Vivo Culture of Human Prostate Tumors. Clinical Cancer Research 2012, 18 (13), 3562-3570.

22. Zielonka, J.; Joseph, J.; Sikora, A.; Hardy, M.; Ouari, O.; Vasquez-Vivar, J.; Cheng, G.; Lopez, M.; Kalyanaraman, B., Mitochondria-Targeted Triphenylphosphonium-Based Compounds: Syntheses, Mechanisms of Action, and Therapeutic and Diagnostic Applications. Chem Rev 2017, 117 (15), 10043-10120.

23. Murphy, M. P.; Smith, R. A., Targeting antioxidants to mitochondria by conjugation to lipophilic cations. Annu Rev Pharmacol Toxicol 2007, 47, 629-56.

24. Gane, E. J.; Weilert, F.; Orr, D. W.; Keogh, G. F.; Gibson, M.; Lockhart, M. M.; Frampton, C. M.; Taylor, K. M.; Smith, R. A.; Murphy, M. P., The mitochondria-targeted anti-oxidant mitoquinone decreases liver damage in a phase II study of hepatitis C patients. Liver Int 2010, 30 (7), 1019-26.

25. Brzheskiy, V. V.; Efimova, E. L.; Vorontsova, T. N.; Alekseev, V. N.; Gusarevich, O. G.; Shaidurova, K. N.; Ryabtseva, A. A.; Andryukhina, O. M.; Kamenskikh, T. G.; Sumarokova, E. S.; Miljudin, E. S.; Egorov, E. A.; Lebedev, O. I.; Surov, A. V.; Korol, A. R.; Nasinnyk, I. O.; Bezditko, P. A.; Muzhychuk, O. P.; Vygodin, V. A.; Yani, E. V.; Savchenko, A. Y.; Karger, E. M.; Fedorkin, O. N.; Mironov, A. N.; Ostapenko, V.; Popeko, N. A.; Skulachev, V. P.; Skulachev, M. V., Results of a Multicenter, Randomized, Double-Masked, Placebo-Controlled Clinical Study of the Efficacy and Safety of Visomitin Eye Drops in Patients with Dry Eye Syndrome. Adv Ther 2015, 32 (12), 1263-79.

26. Lavery, L. A.; Partridge, J. R.; Ramelot, T. A.; Elnatan, D.; Kennedy, M. A.; Agard, D. A., Structural asymmetry in the closed state of mitochondrial Hsp90 (TRAP1) supports a two-step ATP hydrolysis mechanism. Molecular cell 2014, 53 (2), 330-43.

27. Wang, F.; Liu, Y.; Yu, Z.; Li, S.; Feng, S.; Cheng, Y.; Agard, D. A., General and robust covalently linked graphene oxide affinity grids for high-resolution cryo-EM. Proc Natl Acad Sci U S A 2020, 117 (39), 24269-24273.

28. Chae, Y. C.; Caino, M. C.; Lisanti, S.; Ghosh, J. C.; Dohi, T.; Danial, N. N.; Villanueva, J.; Ferrero, S.; Vaira, V.; Santambrogio, L.; Bosari, S.; Languino, L. R.; Herlyn, M.; Altieri, D. C., Control of tumor bioenergetics and survival stress signaling by mitochondrial HSP90s. Cancer cell 2012, 22 (3), 331-44.

29. Wienken, C. J.; Baaske, P.; Rothbauer, U.; Braun, D.; Duhr, S., Protein-binding assays in biological liquids using microscale thermophoresis. Nat Commun 2010, 1, 100.

30. Elnatan, D.; Betegon, M.; Liu, Y.; Ramelot, T.; Kennedy, M. A.; Agard, D. A., Symmetry broken and rebroken during the ATP hydrolysis cycle of the mitochondrial Hsp90 TRAP1. Elife 2017, 6.

31. Verba, K. A.; Wang, R. Y.; Arakawa, A.; Liu, Y.; Shirouzu, M.; Yokoyama, S.; Agard, D. A., Atomic structure of Hsp90-Cdc37-Cdk4 reveals that Hsp90 traps and stabilizes an unfolded kinase. Science 2016, 352 (6293), 1542-7.

32. McLaughlin, S. H.; Smith, H. W.; Jackson, S. E., Stimulation of the weak ATPase activity of human Hsp90 by a client protein 1 1Edited by G. von Heijne. Journal of Molecular Biology 2002, 315 (4), 787-798.

33. Motojima-Miyazaki, Y.; Yoshida, M.; Motojima, F., Ribosomal protein L2 associates with E. coli HtpG and activates its ATPase activity. Biochemical and Biophysical Research Communications 2010, 400 (2), 241-245.

34. Rath, S.; Sharma, R.; Gupta, R.; Ast, T.; Chan, C.; Durham, T. J.; Goodman, R. P.; Grabarek, Z.; Haas, M. E.; Hung, W. H. W.; Joshi, P. R.; Jourdain, A. A.; Kim, S. H.; Kotrys, A. V.; Lam, S. S.; McCoy, J. G.; Meisel, J. D.; Miranda, M.; Panda, A.; Patgiri, A.; Rogers, R.; Sadre, S.; Shah, H.; Skinner, O. S.; To, T. L.; Walker, M. A.; Wang, H.; Ward, P. S.; Wengrod, J.; Yuan, C. C.; Calvo, S. E.; Mootha, V. K., MitoCarta3.0: an updated mitochondrial proteome now with sub-organelle localization and pathway annotations. Nucleic Acids Res 2021, 49 (D1), D1541-D1547.

35. Yim, A.; Koti, P.; Bonnard, A.; Marchiano, F.; Dürrbaum, M.; Garcia-Perez, C.; Villaveces, J.; Gamal, S.; Cardone, G.; Perocchi, F.; Storchova, Z.; Habermann, B. H., mitoXplorer, a visual data mining platform to systematically analyze and visualize mitochondrial expression dynamics and mutations. Nucleic Acids Research 2020, 48 (2), 605-632.

36. Biebl, M. M.; Buchner, J., Structure, Function, and Regulation of the Hsp90 Machinery. Cold Spring Harb Perspect Biol 2019. 11 (9), a034017.

37. Sabharwal, S. S.; Schumacker, P. T., Mitochondrial ROS in cancer: initiators, amplifiers or an Achilles' heel? Nat Rev Cancer 2014, 14 (11), 709-721.

38. Rizza, S.; Montagna, C.; Cardaci, S.; Maiani, E.; Di Giacomo, G.; Sanchez-Quiles, V.; Blagoev, B.; Rasola, A.; De Zio, D.; Stamler, J. S.; Cecconi, F.; Filomeni, G., S-nitrosylation of the Mitochondrial Chaperone TRAP1 Sensitizes Hepatocellular Carcinoma Cells to Inhibitors of Succinate Dehydrogenase. Cancer Res 2016, 76 (14), 4170-82.

39. Masgras, I.; Ciscato, F.; Brunati, A. M.; Tibaldi, E.; Indraccolo, S.; Curtarello, M.; Chiara, F.; Cannino, G.; Papaleo, E.; Lambrughi, M.; Guzzo, G.; Gambalunga, A.; Pizzi, M.; Guzzardo, V.; Rugge, M.; Vuljan, S. E.; Calabrese, F.; Bernardi, P.; Rasola, A., Absence of Neurofibromin Induces an Oncogenic Metabolic Switch via Mitochondrial ERK-Mediated Phosphorylation of the Chaperone TRAP1. Cell Rep 2017, 18 (3), 659-672.

40. Joshi, A.; Dai, L.; Liu, Y.; Lee, J.; Ghahhari, N. M.; Segala, G.; Beebe, K.; Jenkins, L. M.; Lyons, G. C.; Bernasconi, L.; Tsai, F. T. F.; Agard, D. A.; Neckers, L.; Picard, D., The mitochondrial HSP90 paralog TRAP1 forms an OXPHOS-regulated tetramer and is involved in mitochondrial metabolic homeostasis. BMC Biol 2020, 18 (1), 10.

41. Chae, Y. C.; Angelin, A.; Lisanti, S.; Kossenkov, A. V.; Speicher, K. D.; Wang, H.; Powers, J. F.; Tischler, A. S.; Pacak, K.; Fliedner, S.; Michalek, R. D.; Karoly, E. D.; Wallace, D. C.; Languino, L. R.; Speicher, D. W.; Altieri, D. C., Landscape of the mitochondrial Hsp90 metabolome in tumours. Nature communications 2013, 4, 2139.

42. Xiang, Y.; Stine, Z. E.; Xia, J.; Lu, Y.; O'Connor, R. S.; Altman, B. J.; Hsieh, A. L.; Gouw, A. M.; Thomas, A. G.; Gao, P.; Sun, L.; Song, L.; Yan, B.; Slusher, B. S.; Zhuo, J.; Ooi, L. L.; Lee, C. G. L.; Mancuso, A.; McCallion, A. S.; Le, A.; Milone, M. C.; Rayport, S.; Felsher, D. W.; Dang, C. V.,

Targeted inhibition of tumor-specific glutaminase diminishes cell-autonomous tumorigenesis. Journal of Clinical Investigation 2015, 125 (6), 2293-2306.

43. Yang, L.; Venneti, S.; Nagrath, D., Glutaminolysis: A Hallmark of Cancer Metabolism. Annu Rev Biomed Eng 2017, 19, 163-194.

44. Kang, B. H.; Plescia, J.; Dohi, T.; Rosa, J.; Doxsey, S. J.; Altieri, D. C., Regulation of tumor cell mitochondrial homeostasis by an organelle-specific Hsp90 chaperone network. Cell 2007, 131 (2), 257-70.

45. Dutta, R.; Inouye, M., GHKL, an emergent ATPase/kinase superfamily. Trends Biochem Sci 2000, 25 (1), 24-8.

46. Kijima, T.; Prince, T. L.; Tigue, M. L.; Yim, K. H.; Schwartz, H.; Beebe, K.; Lee, S.; Budzynski, M. A.; Williams, H.; Trepel, J. B.; Sistonen, L.; Calderwood, S.; Neckers, L., HSP90 inhibitors disrupt a transient HSP90-HSF1 interaction and identify a noncanonical model of HSP90-mediated HSF1 regulation. Scientific Reports 2018, 8 (1).

47. Marcu, M. G.; Chadli, A.; Bouhouche, I.; Catelli, M.; Neckers, L. M., The Heat Shock Protein 90 Antagonist Novobiocin Interacts with a Previously Unrecognized ATP-binding Domain in the Carboxyl Terminus of the Chaperone. Journal of Biological Chemistry 2000, 275 (47), 37181-37186.

48. Rao, V. A.; Klein, S. R.; Bonar, S. J.; Zielonka, J.; Mizuno, N.; Dickey, J. S.; Keller, P. W.; Joseph, J.; Kalyanaraman, B.; Shacter, E., The antioxidant transcription factor Nrf2 negatively regulates autophagy and growth arrest induced by the anticancer redox agent mitoquinone. J Biol Chem 2010, 285 (45), 34447-59.

49. Cheng, G.; Zielonka, J.; Dranka, B. P.; McAllister, D.; Mackinnon, A. C., Jr.; Joseph, J.; Kalyanaraman, B., Mitochondria-targeted drugs synergize with 2-deoxyglucose to trigger breast cancer cell death. Cancer Res 2012, 72 (10), 2634-44.

50. Cheng, G.; Zielonka, J.; McAllister, D. M.; Mackinnon, A. C., Jr.; Joseph, J.; Dwinell, M. B.; Kalyanaraman, B., Mitochondria-targeted vitamin E analogs inhibit breast cancer cell energy metabolism and promote cell death. BMC cancer 2013, 13, 285.

51. Titova, E.; Shagieva, G.; Ivanova, O.; Domnina, L.; Domninskaya, M.; Strelkova, O.; Khromova, N.; Kopnin, P.; Chernyak, B.; Skulachev, V.; Dugina, V., Mitochondria-targeted antioxidant SkQ1 suppresses fibrosarcoma and rhabdomyosarcoma tumour cell growth. Cell Cycle 2018, 17 (14), 1797-1811.

52. Sun, C.; Liu, X.; Di, C.; Wang, Z.; Mi, X.; Liu, Y.; Zhao, Q.; Mao, A.; Chen, W.; Gan, L.; Zhang, H., MitoQ regulates autophagy by inducing a pseudo-mitochondrial membrane potential. Autophagy 2017, 13 (4), 730-738.

Chapter 3. The crystal structure of human Rogdi provides insight into the causes of Kohlschutter-Tönz Syndrome.

(Original article : Lee H, Jeong H, Choe J, Jun Y, Lim C, Lee C. The crystal structure of human Rogdi provides insight into the causes of Kohlschutter-Tönz Syndrome. *Sci Rep.* 2017;7(1):3972.)

3.1. Abstract

Kohlschutter-Tönz syndrome (KTS) is a rare autosomal-recessive disorder of childhood onset characterized by global developmental delay, spasticity, epilepsy, and amelogenesis imperfecta. Rogdi is an essential protein that is highly conserved across metazoans, and mutations have been implicated as the genetic cause of KTS. Although genetic causes for KTS patients are relatively well established, the molecular basis of how the specific mutations abolish its physiological functions and cause KTS has not yet been elucidated. To gain structural insight into Rogdi mutants and their relationship with KTS, we determined the crystal structure of human Rogdi protein at atomic resolution. Rogdi forms a novel elongated curved structure comprising the α domain, a leucine-zipper-like four-helix bundle, and a characteristic β-sheet domain. Especially within α domain, the N-terminal H1 helix (residues 19–45) pairs with the C-terminal H6 helix (residues 252–287) in an antiparallel manner, indicating that the integrity of the four-helix bundle requires both N- and C-terminal residues. The crystal structure, in conjunction with biochemical data, indicates that the α domain might undergo a conformational change and provide a structural platform for protein–protein interactions. Disruption of the four-helix bundle by mutation results significant destabilization of the structure. Through this structural and biochemical study, we provide structural insight into the link between mutations in Rogdi and the causes of KTS. This fundamental knowledge could assist the development of pharmaceutical agents for the treatment and cure of this debilitating neurological disease.

3.2. Introduction

Genetic mutations often affect the structure of the encoded protein, resulting in structural disruption and, in some cases, disease. For example, sickle cell disease is caused by a single point mutation in the sixth codon of the β-globin gene[9-11]. A change from glutamic acid to valine induces a structural change in red blood cells that consequently adopt a sickle-like shape, and their physiological function is compromised. Similarly, a polymorphism in apolipoprotein E (APOE), a major cholesterol carrier, also demonstrates a cause-and-effect relationship between genetic risk and disease. APOE4, unlike other APOE alleles, has an arginine at residue 112, and the structure of APOE4 is more stable than other isoforms due to the formation of an additional salt bridge involving this residue[12, 13]. This structural feature of APOE4 affects its ability to bind lipids or β-amyloids (Aβ), and contributes to Alzheimer's disease pathogenesis in an Aβ-dependent manner, although the exact mechanism is not completely understood[14].

Kohlschutter-Tönz syndrome (KTS) is a rare genetic disorder characterized by severe global developmental delay, epilepsy, amelogenesis imperfecta, psychomotor delay or regression starting early in childhood, and intellectual disability[15-20]. Amelogenesis imperfecta, the most striking feature of KTS, is used as a clinical marker, which is most obviously observed as yellowed teeth and abnormal enamel[15]. The molecular cause of KTS has not yet been elucidated. However, recent genetic studies using a combination of whole-exome sequencing, autozygosity mapping, linkage analysis, and Sanger sequencing revealed that KTS is caused by putative loss-of-function mutations in the *ROGDI* gene on chromosome 16p13.3[21-24]. Mutations causing KTS include the premature termination of translation of Rogdi, a homozygous frameshift deletion, and an abnormal splicing error.

Rogdi is the human homolog of *Drosophila melanogaster* rogdi, and is a predicted leucine zipper protein of unknown function[21]. The protein is present in metazoan species ranging from worms to humans, and is highly conserved across taxa, indicating an essential functional role that is evolutionarily conserved. A previous study revealed that Rogdi is widely expressed, with particularly high expression in the adult brain, spinal cord, peripheral blood, heart, and bone marrow, suggesting an involvement in neurogenesis[21]. This is supported by data showing that Rogdi directly interacts with DISC1, which is necessary for neuronal proliferation, migration in cerebral interneurons, and their proper differentiation in the cerebral cortex[21, 25, 26]. Another study indicates an important role in tumorigenesis and the cell death mechanism in cervical cancer cells, in which knockdown of the *ROGDI* gene leads to increased p53 and p21 protein levels and downregulation of CDK1 and CDK2[27, 28].

Although the genetic causes of *ROGDI* mutants in KTS patients are relatively well established, the molecular basis by which specific mutations abolish protein function and cause KTS has not yet been elucidated. Herein, we report the atomic resolution structure of the human Rogdi protein for the first time. Combined with biochemical data, the structure provides insight into the link between Rogdi mutants and KTS at the molecular level.

3.3. Results

3.3.1. Crystal Structure Determination.

The human Rogdi protein comprises 287 residues, and is highly conserved among species including fish, fly, frog, worm, and mouse (Figure 3.1). To gain structural insight into Rogdi mutations and their link to KTS, we crystallized human Rogdi. Native crystals of the full-length protein grew in space group R3 and diffracted to 2.8 Å resolution using a synchrotron radiation source. However, we were unsuccessful in producing full-length selenomethionine (Se-Met) derivatized protein, due to poor protein expression in the methionine auxotrophic bacteria. Instead, Se-Met substituted Rogdi was produced and crystallized using N- and C-terminally truncated constructs (residues 11–276, referred to as tRogdi). The structure of tRogdi was determined by single-wavelength anomalous dispersion (SAD) and refined to 2.04 Å resolution. The structure of full-length Rogdi was determined by molecular replacement using the tRogdi structure as a search model and refined to 2.8 Å resolution, with R_{work}/R_{free} values of 21.9/26.8%. Statistics for data collection and refinement are presented in Table 3.1. The structures of full-length and truncated Rogdi are almost identical, with a root mean square deviation (RMSD) of 0.8 Å for all Cα atoms. Therefore, we discuss only the full-length Rogdi structure. Crystals of full-length Rogdi contain four molecules in the asymmetric unit. Interestingly, there are two conformations among the four molecules, with structural differences mainly at the N-terminus (residues 1–14), presumably due to crystal packing. The electron density at the N-terminal region is relatively well ordered in both conformations. Residues 1–14 in the two molecules fold into an alpha-helix (designated as $Rogdi^{H}$), extending the alpha-helix to residue 45, while the same regions in the remaining two molecules are unfolded and form a long loop (designated as $Rogdi^{L}$), suggesting that this region might be flexible in solution. Consistent with this observation, the N-terminus of Rogdi is vulnerable to proteolytic degradation (Figure 1B). The structure of the two $Rogdi^{H}$ molecules and the two $Rogdi^{L}$ molecules are almost identical, with RMSD values of 0.4 and 0.2 Å for all Cα atoms. The two loop regions (residues 92–96 and 212–221) are disordered in the two $Rogdi^{H}$ molecules; however, the electron density for $Rogdi^{L}$ is relatively well ordered throughout the protein chain. Apart from in these regions, no structural differences between $Rogdi^{H}$ and $Rogdi^{L}$ were apparent, as reflected by the RMSD values of 1.5 Å for 236 out of 255 aligned Cα atoms. The N-terminal amino acids 48–55, which correspond to the direct linker between H1 and S1 in all molecules including tRogdi, $Rogdi^{H}$, and $Rogdi^{L}$, were not visible in the electron density map, indicating high flexibility.

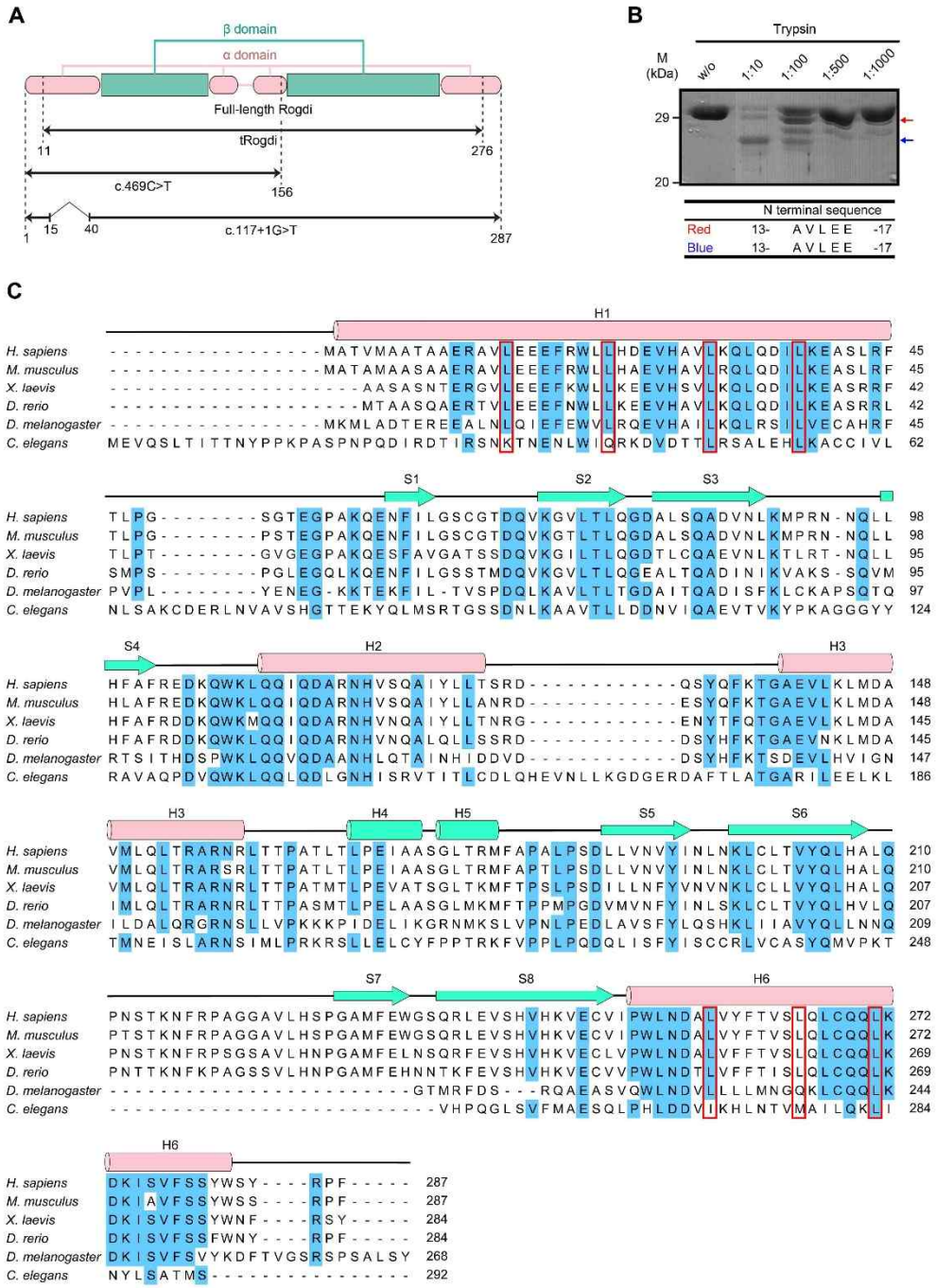

Figure 3.1. Domain Structure of Rogdi.

(**A**) Diagram showing the domain structure of human Rogdi as defined by structural analysis. The crystal structures of full-length and truncated Rogdi (tRogdi, residues 11–276) were determined in this study. Two representative mutants causing KTS are shown to compare the domain structure of wild-type and mutant proteins.

(**B**) Protease digestion of full-length Rogdi by trypsin. Rogdi was mixed with trypsin at the indicated trypsin:Rogdi ratio for 1 h at 4 °C. Reactions were stopped by adding SDS sample buffer, and the products were separated by SDS-PAGE. The two resistant fragments, indicated by red and blue arrows, were subjected to N-terminal sequencing.

(**C**) Sequence alignment of Rogdi from six species (*H. sapience*, *M. musculus*, *X. laevis*, *D. rerio*, *D. melanogaster*, and *C. elegans*). Secondary structural elements are indicated above the sequences, with helices depicted as cylinders and strands as arrows. Conserved residues (five out of six organisms) are highlighted in blue. The repeated heptad leucine residues in H1 and H6, which were predicted to form a leucine zipper motif, are indicated by a red box.

Table 3.1. Data Collection and Refinement Statistics.

	Full-length Rogdi	tRogdi
Data set:	Native	Se-SAD
X-ray source	Beamline 5C, PAL	Beamline 5C, PAL
Temperature (K)	100	100
Space group:	R3	$P2_12_12$
Cell parameters a, b, c (Å)	169.00, 169.00, 220.62	63.36, 114.69, 44.21
	90.00, 90.00, 120.00	90.00, 90.00, 90.00
Data processing		
Wavelength (Å)	1.00000	0.97940
Resolution (Å)	50-2.80	50-2.04
R_{merge} (%)[a]	6.7 (55.1)*	8.2 (46.9)
I/σ	44.6 (5.7)	49.8 (5.9)
Completeness (%)	99.8 (100.0)	99.9 (99.9)
Redundancy	9.1 (9.2)	9.4 (9.3)
Measured reflections	273212	199950
Unique reflections	30008	21207

Refinement statistics

Data range (Å)	36.17-2.80	34.57-2.04
Reflections	57748	39509
Nonhydrogen atoms	8459	1707
Water molecules	104	170
R.m.s. Δ bonds (Å)[b]	0.006	0.004
R.m.s. Δ angles (°)[b]	1.239	0.790
R-factor (%)[c]	21.9	20.1
R_{free} (%)[c, d]	26.8	24.5
Ramachandran plot, residues in		
Most favored regions (%)	90.5	94.4
Additional allowed regions (%)	8.6	5.1
Generously allowed regions (%)	0.8	0.0
Disallowed regions (%)	0.1	0.5

*Highest resolution shell is shown in parenthesis.

[a] $R_{merge} = 100 \times \sum_h \sum_i | I_i(h) - \langle I(h) \rangle | / \sum_h \langle I(h) \rangle$, where $I_i(h)$ is the ith measurement and $\langle I(h) \rangle$ is the weighted mean of all measurement of $I(h)$ for Miller indices h.

[b] Root-mean-squared deviation (r.m.s. Δ) from target geometries.

[c] $R\text{-factor} = 100 \times \sum |F_P - F_{P(calc)}| / \sum F_P$.

[d] R_{free} was calculated with 5% of the data.

3.3.2. Structure of Human Rogdi.

Molecular models of Rogdi are presented in Figure 3.2. The crystal structure shows that Rogdi resembles a boomerang with an elongated curved structure comprising two distinct α and β domains. The α domain consists of four helices (H1 to H3, and H6) that form a left-handed four-helix bundle through van der Waals interactions. Overall, the α domain is a compact rod of 75 Å in length and 25 Å in diameter. The four helices lie in an anti-parallel orientation, with their axes almost parallel to each other, and a hydrophobic core lies buried within. In the four-helix bundle, H2 and H3 are connected to each other via a relatively short loop (residues 129–139), forming a helix-loop-helix structure. By contrast, the secondary structural elements between H1 and H2 and between H3 and H6 are not directly linked by short loops, and are instead separated by a β domain. However, the α domain is not completely isolated from the β domain in terms of the primary structure of Rogdi. Although the H1 helix starts from the N-terminus (residue 1), the first α-helix involved in forming the four-helix bundle starts from residue 19. Residues 1–18 of helix H1 are not directly involved in forming the four-helix bundle structure, consistent with a high degree of flexibility for this region, as indicated in the crystal structure and by the limited proteolysis results. The H1 helix of the four-helix bundle starts at residue 19 and ends at residue 45, and its adjacent anti-parallel paired helix (H6) begins from residue 252 and ends at the C-terminus (residue 287). Therefore, the α domain spans from the N-terminus to the C-terminal of the Rogdi sequence (Figures 3.1.A and 3.2B).

The β domain adopts a β-sandwich structure comprising two β-sheets that are stacked layer in a layer and twisted anticlockwise relative to each other. Both β-sheets contain four (S1 to S4 and S5 to S8) anti-parallel β-strands, and are flanked by two short α-helices (H4 and H5). The first sheet forms a canonical up-and-down anti-parallel β-strand structure. The second β-sheet folds into a more unique structure by combining a β-hairpin structure consisting of S5 and S6 with a Greek key-like motif comprising S6 to S8 plus a flexible loop (residues 209 to 228)[29]. Overall, the β domain has eight anti-parallel β-strands and two α-helices, which are packed into a compact domain with dimensions of 40 Å × 28 Å × 33 Å.

The α and β domains are not separated from each other, but rather are tightly packed together. In particular, the β-hairpin structures of each sheet are embedded in a crevice formed by one end of the two anti-parallel α-helices. To form the tight association, Leu 77 and Ile 194 from the β-strands are inserted into the center of the interface and form hydrophobic interactions with Phe 45 of helix H1, Leu 110 and Ile 113 of helix H2, Leu 160 of helix H3, and Trp 253 and Leu 254 of helix H6 from the α domain. These interacting residues are highly conserved, suggesting that the van der Waals contacts between α and β domains are preserved among different species. In addition to hydrophobic interactions,

the side chains of Asp 80 and Asn 197 in the β-hairpin engage in hydrogen bonds with the side chains of residues Arg 117 and Asn 255 from the α domain helices (Figure 3.2.D).

Human Rogdi has a polymorphism, E59K. It is located at the end of loop generated between H1 helix and S1 strand (Figure 3.1.C and 3.2.D). The side of Glu59 projects toward protein surface, and is not directly involved in the interaction with other residues. Furthermore, the residue is not conserved in the *C. elegans*. Based on these observations, the E59K polymorphism in Rogdi might not affect the overall structure and function of Rogdi.

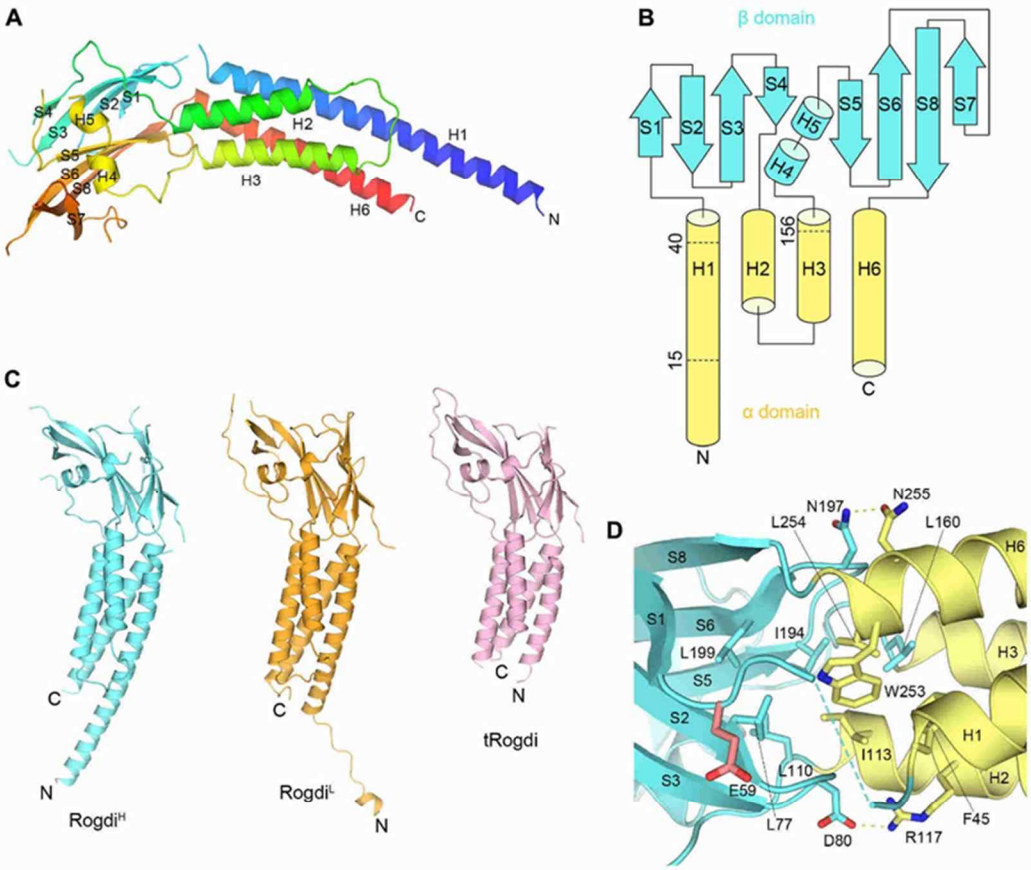

Figure 3.2. Crystal Structure of Rogdi.

(**A**) Ribbon diagram showing the structure of full-length Rogdi. The protein is composed of two distinct α and β domains. The protein chain is colored blue to red from the N- to C-terminus.

(B) Topological diagram showing the secondary structural elements and domain organization of human Rogdi. Helices and strands are depicted by cylinders and arrows, respectively. The color scheme is identical to that in Figure 3.1.C.

(**C**) Overall structure of full-length Rogdi ($Rogdi^{H}$ = cyan, $Rogdi^{L}$ = orange) and tRogdi (pink) in the same orientation for comparative purposes.

(**D**) Close-up view showing residues that contribute to the tight association at the interface between the β (cyan) and β (yellow) domains. Oxygen and nitrogen atoms are colored red and blue, respectively. Yellow dotted lines indicate intermolecular hydrogen bonds.

3.3.3. The α Domain of Rogdi adopts a Leucine Zipper-Like Structure.

Rogdi is a predicted leucine zipper (ZIP) protein based on sequence analysis, which reveals a periodic repetition in leucine residues at every seventh position. Most heptad leucine residues are in the N-terminal region, specifically residues 15 to 47, but residues 251 to 282 are near the C-terminus (Figure 3.1.C). However, the crystal structure reveals that full-length Rogdi is unexpectedly monomeric, unlike most ZIP proteins that exhibit a left-handed parallel dimeric coiled-coil structure or a higher order oligomer[30]. The monomeric organization of Rogdi was confirmed in solution by biochemical experiments including size-exclusion chromatography and analytical ultracentrifugation (Figure 3.3.A and 3.3.B). Although Rogdi does not self-associate through the coiled-coil α domain, a set of predominantly repeated leucine residues are buried and involved in forming hydrophobic interfaces in the four-helix bundle structure. Based on this observation, we propose that two parallel helical pairs (H1/H3 or H2/H6) arrange into leucine zipper-like domains within the Rogdi monomer (Figure 3.3.C). The hydrophobic side chains of V27, L31, L34, and L38 of H1, and those of V142, M146, V149, and L153 of the parallel H3, are oriented towards each other, where they contribute to the stabilization of the four-helix bundle structure by forming hydrophobic interactions. Likewise, the hydrophobic side chains of I113, A116, V120, and A123 of H2, and those of L254, A257, F261, and S264 of its parallel H6, are buried at the interface and involved in hydrophobic interactions. However, the axes of H2 and H6 are not parallel, but slightly tilted. In addition to hydrophobic interactions, six hydrogen bonds are present at the surface of the amphipathic helices. In particular, the side chains of Glu 26 and Arg 44 from H1 form salt bridges with the side chains of Lys 274 and Asp 256 from H6. Furthermore, the side chains of Asp 147 and Gln 152 from H3 form H-bonds with the side chains of Lys 272 from H6 and His 119 from H2. Lastly, the side chain of Gln 35 from H1 forms an H-bond contact with the side chain of Gln 132 from H2 (Figure 3.3.D).

In general, the basic ZIP interacts with the DNA via its positively charged motifs located next to the ZIP[31]. However, the crystal structure revealed that Rogdi is likely not a DNA-binding protein, because although it has a comparable ZIP structure, but it does not have the basic motif for protein-DNA interactions (Figure 3.4.C). Indirect evidence for DNA binding was from a previous immunostaining study using Rogdi-transfected HEK293 cells, which revealed that Rogdi is localized at the nuclear envelope[21].

In summary, although Rogdi itself does not self-oligomerize, the α domain adopts a leucine zipper-like structure in which repeated hydrophobic residues are involved in forming the hydrophobic core of the four-helix bundle. Nevertheless, at this point, we cannot exclude the possibility that Rogdi might interact with other proteins through the coiled-coil motif of the α domain.

A

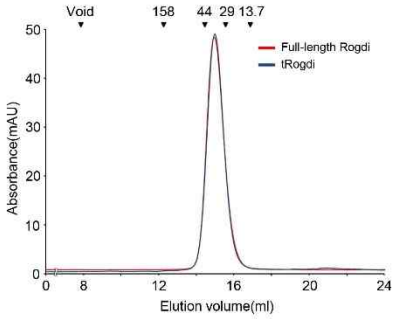

B

Protein	Theoretical M.W.(kDa)	Estimated M.W.(kDa)	Estimated M.W. /Theoretical M.W.
Full-length Rogdi	32.2	32.7	1.02
tRogdi	29.9	30.0	1.00

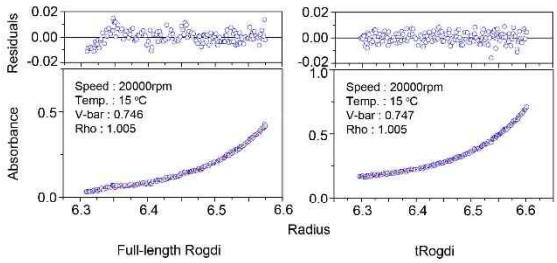

C

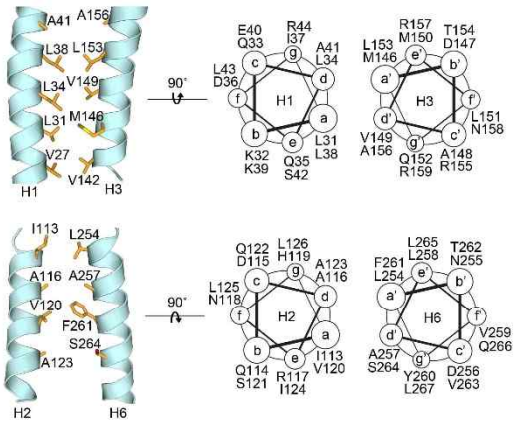

D

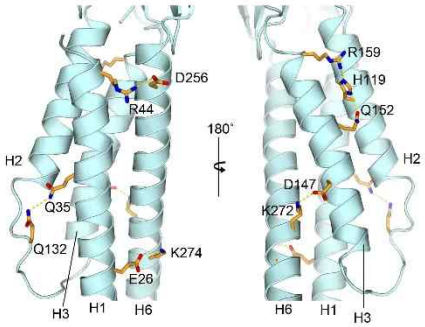

Figure 3.3. The Leucine Zipper-Like Domain of Rogdi.

(**A**) Size-exclusion chromatography analysis of full-length and truncated (residues 11–276) Rogdi showing the oligomeric state. Molecular mass standards for SEC experiments (top) were aldolase (158 kDa), ovalbumin (44 kDa), carbonic anhydrase (29 kDa) and RNase A (13.7 kDa). Chromatography was performed on a Superdex 200 column in buffer containing 25 mM TRIS, 150 mM NaCl, and 5 mM DTT (pH 7.5).

(**B**) Equilibrium fitting of the results of analytical ultracentrifugation for full-length (left) and truncated (right) Rogdi. The lower panel depicts the fitted overlay (red line) to the experimental data (blue circles). The upper panel depicts the residuals.

(**C**) Helical wheel representation and cartoon diagrams showing the heptad repeat and intermolecular interactions within two parallel helices (H1/H3, top and H2/H6, bottom) of the Rogdi α domain.

(**D**) Detailed view of the intermolecular hydrogen bonds between the surface of amphipathic helices of the α domain. Dotted lines indicate hydrogen bonds (Q35-Q132, R159-H119, and H119-Q152) and three ion pairs (see text for details).

3.3.4. Extended H1 and H6 Helices Mediate Coiled-Coil Protein Interactions.

As mentioned earlier, crystals of full-length Rogdi revealed two conformations, designated as Rogdi^{H} and Rogdi^{L}, depending on the continuity of H1 helix. Given that the N-terminal residues 1−11 are easily accessible and prone to proteolytic degradation, the non-paired region of H1 in the four-helix bundle (residues 1−14) might be flexible in solution. This is consistent with the structure of Rogdi^{L}, in which H1 helix residues 1−14 are disassociated from the helix and form a sharp bend due to steric hindrance by neighboring molecules in the crystal (Figure 4A). However, this region might undergo a conformational change and adopt a helical structure with a parallel helix from a neighboring molecule, as shown in Rogdi^{H} (Figure 3.4.B). The extended H1 helix in Rogdi^{H} engages in a parallel coiled-coil interaction with the adjacent H1 and H6 helices from the other molecule via crystal packing. The interface residues facing the coiled-coil domain are composed of hydrophobic residues such as Ala 6, Ala 10, Val 14 and Trp 21 from H1, and Val 259, Tyr 260, Val 263, and Leu 267 from H6. In particular, a highly conserved hydrophobic patch comprising Leu 23, Ile 37, Leu 267, and Val 277 from H1 and H6 is exposed to the surface, suggesting that the hydrophobic surface generated by helices H1 and H6 could provide a platform for a protein–protein interaction module by conformational changes of the N-terminus into an extended H1 helix (Figure 4C).

Previous studies using the yeast-two hybrid technique discovered that Rogdi might interact with DISC1 (MIM 605210), a protein implicated in the development of schizophrenia and involved in cytoskeletal stability and organization, neuronal migration, intracellular transport, and cell division[21, 25, 26]. Future work will be required to address whether the extended H1 helix might be involved in interactions with other binding partners such as DISC1.

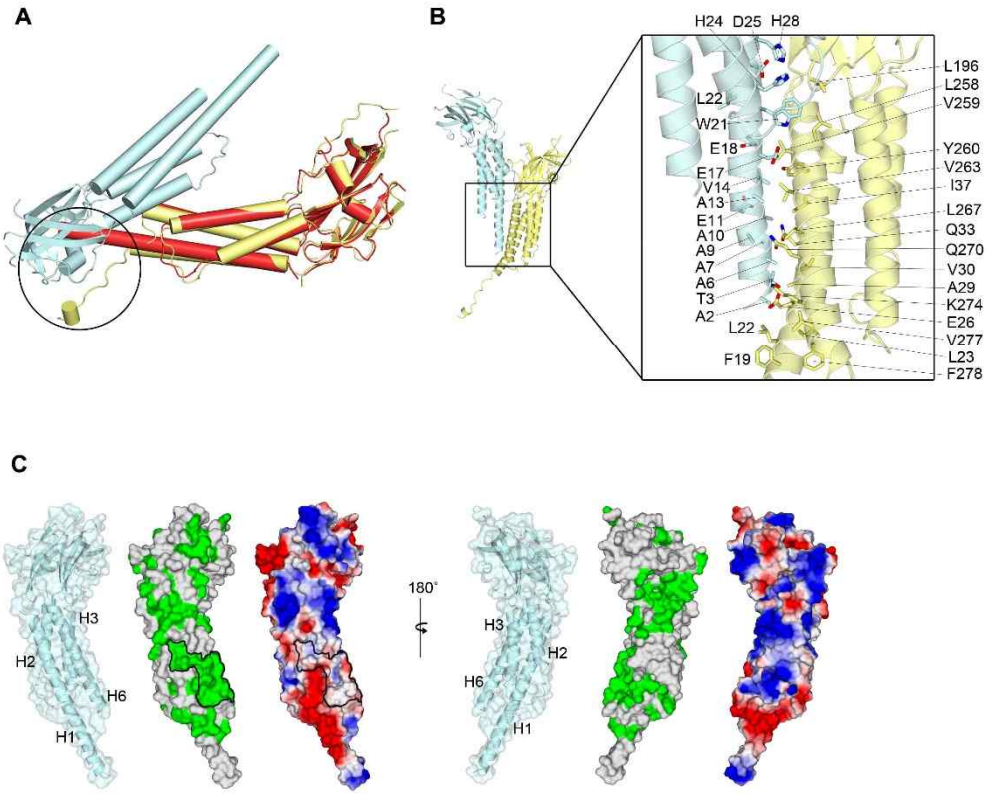

Figure 3.4. Extended H1 and H6 Helices Mediate Protein–Protein Interactions.

(**A**) Crystal contacts of Rogdi^{L} in the asymmetric unit. Circles indicate the flexible N-terminal helix of Rogdi^{L}, which is bent sharply due to steric hindrance. The structure of Rogdi^{H} (red) is overlaid with that of Rogdi^{L} (yellow) for structural comparison and to highlight steric hindrance between molecules in the crystal asymmetric unit.

(**B**) Rogdi molecules showing crystal contacts (left). The close-up view on the right shows residues that contribute to contact surfaces. Oxygen and nitrogen atoms are colored red and blue, respectively.

(**C**) Surface representation of Rogdi^{H}. The surface is colored according to residue identity (middle) as shown in Figure 1B, and according to charge distribution (right), highlighting the conservation of hydrophobic residues that might be involved in protein–protein interactions.

3.3.5. Rogdi Resembles the Claudin-15, Tight Junctions Component.

To obtain insight into the molecular functions of Rogdi based on its structure, we searched the Protein Data Bank (PDB) using DALI[32], and found that full-length Rogdi is most similar to Claudin-15 (Z-score = 8.4), which is a major membrane component of tight junctions[33]. In particular, the structure of Rogdi appears to share four structural features with Claudin-15 (Figure 3.5.A). (i) Claudin-15 is also composed of a characteristic β-sheet fold and a four-helix bundle; (ii) the typical left-handed four-helix bundle of Claudin-15 spans the entire protein chain from the N- to the C-terminus, as is the case for the α domain of Rogdi; (iii) the β-strands in the β-sheet are organized in an anti-parallel manner and are flanked by a short α-helix; and (iv) the two distinct α and β domains are not spatially separated but tightly packed together. Since these structural features are also shared with the Rogdi structure, the two proteins could conceivably share similar functions, most likely as scaffolds and/or engaging in self-polymerization in tight junctions[33]. Other than Claudin-15, the full-length Rogdi structure did not share a great deal of similarity with any other soluble proteins.

Although the full-length Rogdi structure could only be aligned with Claudin-15, the separate domains could be superimposed with pectin methylesterase inhibitor and staphostatin A with an RMSD of 3.3 and 5.7 Å, respectively (Figures 3.5.B and 3.5.C). However, we propose that the similarity with these domains does not clearly reflect their molecular functions, because the RMSD values do not indicate a close structural similarity, and the two distinct domains of Rogdi are not separate but are tightly associated with each other.

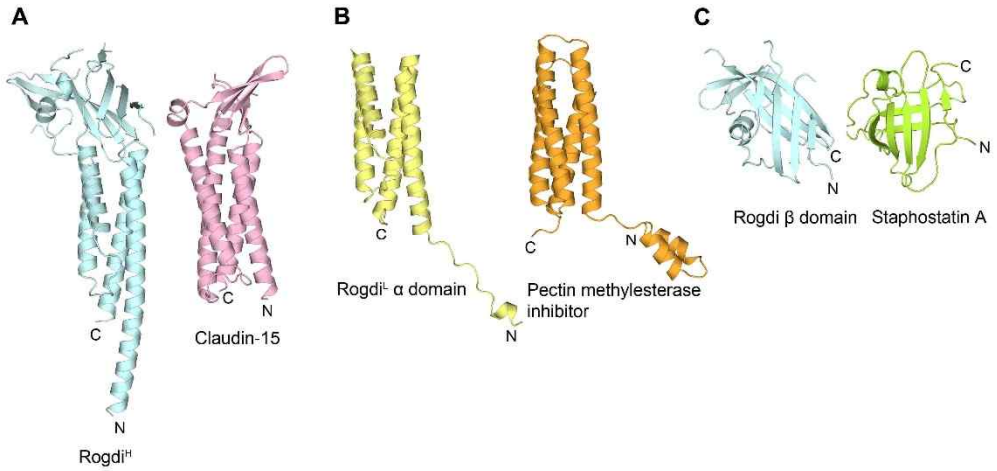

Figure 3.5. Structural Comparison between Rogdi and Claudin-15.

Structural comparison of Rogdi and proteins with a similar fold, shown in the same orientation. Full-length Rogdi^{H} most closely resembles Claudin-15 (A, PDB ID: 4P79), an essential component of tight junctions. Rogdi^{L} shows structural similarity with pectin methylesterase inhibitor (B, PDB ID: 1X8Z) and staphostatin A (C, PDB ID: 1OH1).

3.3.6. The Relationship between Rogdi Mutations and KTS.

xtensive genetic analyses have revealed that mutations in the *ROGDI* gene appear to cause KTS. Mutations of Rogdi implicated in KTS are summarized in Table 3.2. All mutations identified to date are frameshift, nonsense, or splice-site mutations that are expected to either cause premature mRNA degradation by nonsense-mediated decay, or dramatically alter the protein structure and thereby cause a complete loss of protein function. In particular, *ROGDI* c.469C>T and c.286C>T mutations cause the premature termination of translation at residue 157 and residue 96, respectively[22]. Residue 157 is located at the C-terminal end of H3, indicating that this mutant is truncated at the second β-sheet and H6. Since H6 is a component of the four-helix bundle in the α domain, the mutant would disrupt both α and β domains (Figures 3.1.A and 3.6.A). Recently, the novel *ROGDI* homozygous mutation (c.117+1G>T) was identified in a patient with KTS[23]. The mutation abolishes the usual splice donor site of intron 2, which causes the deletion of exon 2 and the in-frame assembly of exon 3. Exon 2 encodes a highly conserved 24 amino acid region (residues 16–39), which corresponds to the central region of H1 (Figure 3.1.A). Apart from these residues, the mutant protein would have no further truncations. Deletion mutations may reduce the length of helix H1 from 45 to 20 amino acids, or disrupt the structure of the H1 helix itself. In both cases, mutation would break the hydrophobic core responsible for stabilizing the four-helix bundle (Figure 3.6.B). Based on this hypothesis, we propose that defects in the α domain would affect the stability and hence the molecular function of the Rogdi protein, and thereby cause KTS. Notably, there are numerous reports demonstrating that the stability of four-helix bundles is essential for the structure and function of proteins[34-36].

To further investigate the potential importance of the α domain to the stability of the Rogdi protein, we generated point mutant constructs (F261A and L271A) to induce interruptions in the hydrophobic core of the α domain, and measured protein stability using circular dichroism (CD) spectroscopy. A wavelength scan of the mutants showed no significant differences in spectra, suggesting that mutations did not affect the secondary structure (Figure 3.6.C). We determined the folding free energy value of wild-type and mutant Rogdi proteins using chemical and thermal denaturation experiments in which the loss of α-helical structure was monitored by CD spectroscopy at neutral pH. Surprisingly, the melting temperatures for the F261A and L271A mutants were decreased by ~4–5 °C compared with the wild-type protein and a negative control mutant (Q266A), suggesting the disruption of the hydrophobic core destabilizes the helical bundle of the α domain and affects the overall protein stability (Figure 3.6.D). Consistent with the thermal stability data, all affected mutants exhibited significantly less resistance to urea-induced protein denaturation (Figure 3.6.E).

Most interestingly, although deletion of the N-terminus (residues 16–39) did not affect the CD

wavelength spectrum, the dramatic disruption of the thermal and chemical stability indicated that the deletion affected the protein structure and stability, which might explain the KTS disease-causing phenotype (Figures 3.6.B to 3.6.E). It is still unknown whether the α domain is involved in protein–protein interactions, and what the molecular functions of such interactions might be. However, we believe that the α domain of Rogdi contributes to the overall structure and stability, and perturbation of the α domain by mutation likely results in the loss of function and the eventual onset of KTS.

Table 3.2. Summary of KTS-associated *Rogdi* mutations.

Type of Mutation	Genotype	Molecular Phenotype	Ref.
Deletion mutation	homozygous for c.229_230del	p.Leu77Alafs*64	[14]
	homozygous for c.507delC	p.Glu170Argfs*72	[16]
	homozygous for c.46–37_46–30del	N/A	[16]
	homozygous for c.45+9_45+20del	p.Glu16Valfs*57	[16]
Nonsense mutation	homozygous for c.286C>T	p.Gln96*	[14]
	homozygous for c.469C>T	p.Arg157*	[13]
Duplication and deletion mutation	heterozygous for c.366dupA and c.45+9_45+20del	p.Ala123Serfs*19	[16]
Splicing-site mutation	heterozygous for c.531+5G>C and c.532-2A>T	N/A	[14]
	homozygous for c.117+1G>T	24 A.A. deletion from position Glu16 to Lys39	[15]

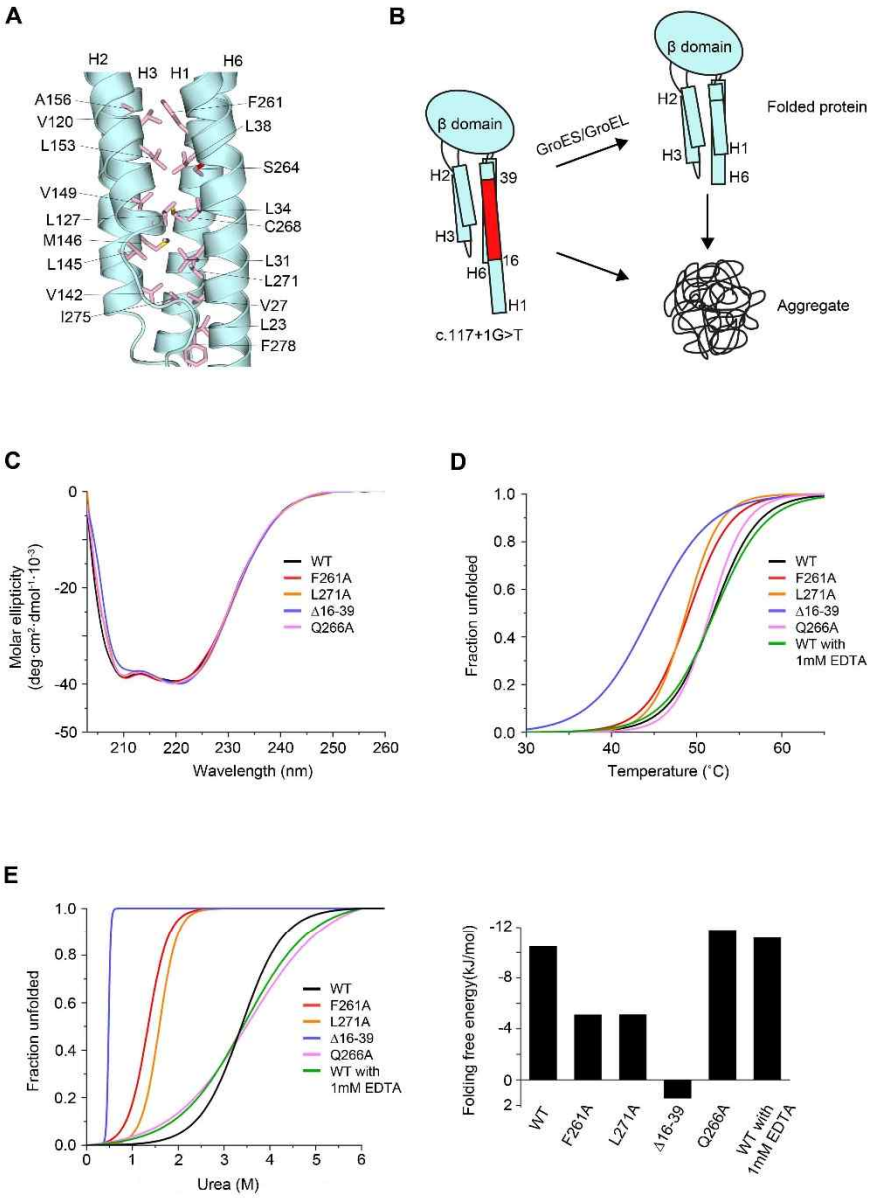

Figure 3.6. Mutation of Rogdi affects Structure and Stability.

(**A**) Close-up view of the four-helix bundle hydrophobic interface in the α domain of Rogdi.

(**B**) Schematic diagram showing the possible domain organization in the c. 117+1G>T mutant[23]. The red region (residues 16–39) of H1 is deleted in the mutant due to a splicing error.

(**C**) Far-UV CD spectra of wild-type and mutant Rogdi scanned from 203 to 260 nm.

(**D**) Thermal unfolding curves of wild-type and mutant Rogdi measured by CD spectroscopy.

(**E**) Urea-induced unfolding of wild-type and mutant Rogdi[37] conducted by monitoring loss of helicity during CD spectroscopy at 222 nm.

3.4. Discussion

Rogdi has been predicted to be a leucine zipper protein and a transcription factor. However, our crystal structure revealed that the N- and C- termini of Rogdi include periodically repeating leucine residues that contribute to the formation of a four-helix bundle structure rather than a typical leucine zipper, although the α domain does adopt an internal ZIP-like structure (Figure 3.3.C). Most importantly, we also found that the N-terminal H1 helix (residues 19–45) is paired with the C-terminal H6 helix (residues 252–287) in an anti-parallel manner, indicating that the integrity of the four-helix bundle requires both N- and C-terminal residues (Figure 3.2.B). Thus, truncation mutations might seriously affect the overall structure, and cause the protein to be degraded (Figure 3.6). Mounting evidence suggests mutation of Rogdi is the genetic cause of KTS. In particular, quantitative RT-PCR data from KTS patients showed that transcription of Rogdi is lower than in wild-type controls, indicating that mutated transcripts are selectively degraded through a nonsense-mediated decay[22]. In the present study, we further demonstrated that even if translation of mutated Rogdi transcripts is completed, the structure of the truncated Rogdi protein is likely to be unstable and prone to degradation, based on the crystal structure. The α domain in particular appears to be very important for the overall structure and stability, and presumably for mediating protein–protein interactions.

Rogdi appears to share several key structural features with Claudin-15 (Figure 3.5.A). In addition, it was recently reported that Claudin-4 and Claudin-19, which are structurally similar to Claudin-15, interact with a *Clostridium perfringens* enterotoxin via their β-sheet structures, resulting in the disintegration of tight junctions[38, 39]. Although future work is clearly necessary, the β domain of Rogdi might also perform essential molecular functions, such as providing a binding platform for interacting partners.

Recently, patients showing atypical KTS phenotypes without any mutations in the *ROGDI* gene have been reported, suggesting that other genes might also cause KTS[22, 24, 40]. Indeed, according to the report, mutation in the *SLC13A5* gene, which encodes a sodium-dependent citrate transporter, might also cause KTS[41]. Moreover, the *ROGDI* gene is reported to play an important role in tumorigenesis and the cell cycle[27, 42]. However, it has not yet been elucidated whether there is a molecular correlation between *ROGDI* and *SLC13A5* in cancerous cells. Therefore, further study is needed to expand our understanding of the cellular functions of Rogdi and its relationship to KTS phenotypes. Nevertheless, the structural and biochemical results of the present study provide structural insight into the relationship between Rogdi and KTS, and this fundamental knowledge might prove useful for the development of pharmaceutical agents for the treatment or cure of this debilitating neurological disease.

3.5. Materials and Methods

3.5.1. Protein Production.

Human full-length (residues 1–287) and truncated (tRogdi, residues 11–276) Rogdi proteins were expressed in *E. coli* BL21(DE3) cells from a modified pET-Duet vector with an N-terminal His_6 tag followed by a TEV protease cleavage site. Cells were lysed in 25 mM sodium phosphate (pH 7.5) containing 400 mM NaCl and protease inhibitors. After Ni^{2+} affinity chromatography, the His_6 tag was cleaved by TEV protease, and the protein was purified further by ion-exchange and gel-filtration chromatography steps. Selenomethionine-substituted protein was generated by expressing the tRogdi protein in *E. coli* B834 (DE3) cells (Novagen) using M9 minimal medium plus selenomethionine. The protein was concentrated to ~20 mg/ml by centrifugation in 25 mM TRIS-HCl containing 150 mM NaCl and 5 mM DTT (pH 7.5) and flash-frozen in liquid nitrogen for storage. Rogdi mutants were generated using PCR-based methods. All mutants were overexpressed at room temperature in the same *E. coli* host as glutathione S-transferase (GST) fusion proteins using the pGEX-6P1 vector (GE Healthcare). To increase the solubility of the deletion mutant, we co-expressed with bacterial GroESL chaperone proteins. The GST-Rogdi mutants were purified using glutathione S-sepharose and cleaved by PreScission protease (GE healthcare). Mutant proteins were purified further by cation-exchange chromatography on a HiTrap SP column and by gel-filtration chromatography on a Superdex 200 column.

3.5.2. Crystallization and Structure Determination by SAD.

Human tRogdi protein was crystallized at 4 °C by the hanging-drop vapor diffusion method by adding 1 μl of a 9 mg/ml protein solution to 1 μl of well solution comprising 11% PEG 4K, 100 mM MES pH 6.5, and 5 mM DTT. The resultant orthogonal crystals belong to space group $P2_12_12$ (a = 63.4 Å, b = 114.7 Å, c = 44.2 Å) and contain one molecule in the asymmetric unit. For X-ray diffraction experiments, crystals were transferred to well solution containing 30% glycerol and flash-frozen in liquid nitrogen. Single-wavelength anomalous diffraction (SAD) data were collected from a Se-Met crystal at beamline 5C of the Pohang Accelerator Laboratory (PAL) and processed using HKL-2000 software[43]. SAD data analysis was performed using Phenix [5] software using data between 50 and 2.04 Å resolution. Phenix found eight of the nine selenium sites and refined them to a mean figure-of-merit of 0.38. Electron density modification using RESOLVE software[44] yielded an initial electron density map of excellent quality. Successive rounds of model building and refinement were performed using Coot and Phenix, respectively[5, 6]. The final model contains one tRogdi monomer in the asymmetric unit. Residues 11 to

23, 47 to 56, 64 to 68, 92 to 96, 130 to 138, and 266 were not modelled due to weak electron density.

For full-length Rogdi crystals, protein solution (1 μl) was mixed with an equal volume of 2 M sodium chloride, 130 mM magnesium chloride, and 100 mM TRIS pH 7.0. Crystals (space group R3; a = b = 169.0 Å, c = 220.6 Å) grew within 1 week at 4 °C. For diffraction experiments, crystals were transferred to well solution containing an additional 30% glycerol and flash-frozen in liquid nitrogen. X-ray diffraction data were collected at the same PAL beamline and processed as described above. The structure was solved by molecular replacement using Phaser[45] with the tRogdi structure as the search model. An initial model of tRogdi was improved by rigid-body and positional refinement, and the structure was built into the resulting electron density map. Final refinement yielded an R-factor of 21.9% (R_{free} = 26.8%) for data between 35 and 2.8 Å resolution (Table 3.1). The final model consists of 8459 protein atoms and contains four copies of Rogdi in the asymmetric unit. Of these, the following residues were not modelled due to weak electron density: Residues 48 to 55, 211, 235, and 286 to 287 in the first copy; residues 48 to 55, 211, and 286 to 287 in the second copy; residues 48 to 56, 64 to 68, 92 to 96, 212 to 221, and 284 to 287 in the third copy; residues 48 to 56, 64 to 68, 94 to 96, 181, 212 to 221, and 284 to 287 in the fourth copy. The refinement statistics and composition of the final models are summarized in Table 3.1.

3.5.3. CD Spectroscopy.

The secondary structure of Rogdi mutants were monitored using a CD spectrometer (Jasco J-815) with wavelength scans from 190 to 260 nm. Possible conformational changes were also monitored by CD spectroscopy at various temperatures by raising the temperature from 25 to 85 °C over a 5 min period, with detection at 222 nm. All samples were prepared in 25 mM TRIS pH 7.5, 150 mM NaCl, 5 mM β-mercaptoethanol, pH 7.5. For chemical denaturation, protein samples were mixed with 0 to 8 M urea, incubated for 5 h at room temperature, and measured at 222 nm on the same CD spectrometer.

3.5.4. Unfolding Titration for Determination of Folding Free Energy.

To determine the folding free energy of Rogdi proteins, we assumed that all proteins had folded and unfolded states that were dependent on the concentration of urea, and that the two states were reversible, as summarized in the following expressions:

Unfolded protein $\rightleftarrows$ folded protein (1)

In the reaction (1), the folding constant, K_F, was calculated from the following formula:

$K_F = [F]/[U]$ (2)

where [F] is the concentration of the folded protein, and [U] is the concentration of the unfolded protein.

Each concentration can be expressed in terms of the total protein concentration (P_t) and the fraction unfolded (f_U). Equation (2) can be expressed in terms of P_t and f_U as follows:

$K_F = P_t*(1-f_U)/(P_t*f_U)$

$= (1-f_U)/f_U$ (3).

The fraction unfolded is then calculated from the observed ellipticity ([θ]) as follows:

$f_U = ([\theta] - [\theta]_F)/([\theta]_U - [\theta]_F)$ (4).

The $[\theta]_F$ is the ellipticity of the fully folded protein, and $[\theta]_U$ is the ellipticity of the fully unfolded protein. The free energy of the protein is calculated using the following formula:

$\Delta G = -RT\ln(K_F)$ (5)

where R is the gas constant and T is the absolute temperature. The free energy of the protein can then be calculated depending on the concentration of urea ([urea]). To determine the folding free energy of the protein (ΔG^o), ΔG and [Urea] are fitted to a y = ax + b plot using the following:

$\Delta G = m[urea] + \Delta G^o$ (6)

where m is the slope, and G is the folding free energy when the concentration of urea is zero.

3.5.5. Analytical Ultracentrifugation.

The molecular mass of human full-length and truncated Rogdi was analyzed by analytical ultracentrifugation (Optima XL-A; Beckman) using the sedimentation equilibrium technique. For sedimentation equilibrium analytical ultracentrifugation, protein samples were prepared in buffer containing 25 mM TRIS-HCl (pH 7.5), 150 mM NaCl, and 5 mM β-mercaptoethanol at concentrations of 10 μM, 15 μM, and 20 μM. Data were evaluated using a nonlinear least-squares curve-fitting algorithm in the XL-A data analysis software. For equilibrium analysis, scans obtained at equilibrium using multiple speeds (10000, 20000 and 30000 rpm) were collected at 15 °C using an An-60 Ti rotor (Beckman) by measuring the absorbance at 280 nm. Measurements were fitted to a single species model using Origin 6.03 software (Beckman Coulter, Inc.).

3.5.6. Sequence Analysis.

For sequence alignment (Figure 3.1.C), Rogdi sequences from six organisms were aligned: *Homo sapiens* (NP_078865), *Mus musculus* (NP_573448), *Xenopus laevis* (AAH94137), *Caenorhabditis elegans* (NP_498641), *Danio rerio* (NP_956257), and *Drosophila melanogaster* (NP_648956).

3.5.7. Limited Proteolysis.

Limited proteolysis experiments were carried out to define domain boundaries. Full-length Rogdi was

digested with trypsin using a range of protein concentrations and incubation times at 4 °C. The reaction was stopped with 1 mM PMSF, and products were analyzed by SDS-PAGE and N-terminal protein sequencing.

3.6. References

1. Lee, C.; Park, H. K.; Jeong, H.; Lim, J.; Lee, A. J.; Cheon, K. Y.; Kim, C. S.; Thomas, A. P.; Bae, B.; Kim, N. D.; Kim, S. H.; Suh, P. G.; Ryu, J. H.; Kang, B. H., Development of a Mitochondria-Targeted Hsp90 Inhibitor Based on the Crystal Structures of Human TRAP1. *Journal of the American Chemical Society* **2015,** *137* (13), 4358-67.

2. Taldone, T.; Patel, P. D.; Patel, M.; Patel, H. J.; Evans, C. E.; Rodina, A.; Ochiana, S.; Shah, S. K.; Uddin, M.; Gewirth, D., Experimental and structural testing module to analyze paralogue-specificity and affinity in the Hsp90 inhibitors series. *Journal of medicinal chemistry* **2013,** *56* (17), 6803-6818.

3. Lavery, L. A.; Partridge, J. R.; Ramelot, T. A.; Elnatan, D.; Kennedy, M. A.; Agard, D. A., Structural asymmetry in the closed state of mitochondrial Hsp90 (TRAP1) supports a two-step ATP hydrolysis mechanism. *Molecular cell* **2014,** *53* (2), 330-43.

4. Otwinowski, Z.; Minor, W., Processing of X-ray diffraction data collected in oscillation mode. *Method Enzymol* **1997,** *276*, 307-326.

5. Adams, P. D.; Afonine, P. V.; Bunkoczi, G.; Chen, V. B.; Davis, I. W.; Echols, N.; Headd, J. J.; Hung, L. W.; Kapral, G. J.; Grosse-Kunstleve, R. W.; McCoy, A. J.; Moriarty, N. W.; Oeffner, R.; Read, R. J.; Richardson, D. C.; Richardson, J. S.; Terwilliger, T. C.; Zwart, P. H., PHENIX: a comprehensive Python-based system for macromolecular structure solution. *Acta Crystallogr D Biol Crystallogr* **2010,** *66* (Pt 2), 213-21.

6. Emsley, P.; Lohkamp, B.; Scott, W. G.; Cowtan, K., Features and development of Coot. *Acta Crystallogr D Biol Crystallogr* **2010,** *66* (Pt 4), 486-501.

7. Hansen, S., BayesApp: a web site for indirect transformation of small-angle scattering data. *J Appl Crystallogr* **2012,** *45*, 566-567.

8. Kang, M. S.; Kim, J.; Ryu, E.; Ha, N. Y.; Hwang, S.; Kim, B. G.; Ra, J. S.; Kim, Y. J.; Hwang, J. M.; Myung, K.; Kang, S., PCNA Unloading Is Negatively Regulated by BET Proteins. *Cell Rep* **2019,** *29* (13), 4632-4645 e5.

9. Pauling, L.; Itano, H. A.; Singer, S. J.; Wells, I. C., Sickle Cell Anemia, a Molecular Disease. *Science* **1949,** *110* (2865), 543-548.

10. Ingram, V. M., Gene Mutations in Human Haemoglobin: the Chemical Difference Between Normal and Sickle Cell Haemoglobin. *Nature* **1957,** *180* (4581), 326-328.

11. Hoban, M. D.; Cost, G. J.; Mendel, M. C.; Romero, Z.; Kaufman, M. L.; Joglekar, A. V.; Ho, M.; Lumaquin, D.; Gray, D.; Lill, G. R.; Cooper, A. R.; Urbinati, F.;

Senadheera, S.; Zhu, A.; Liu, P.-Q.; Paschon, D. E.; Zhang, L.; Rebar, E. J.; Wilber, A.; Wang, X.; Gregory, P. D.; Holmes, M. C.; Reik, A.; Hollis, R. P.; Kohn, D. B., Correction of the sickle cell disease mutation in human hematopoietic stem/progenitor cells. *Blood* **2015,** *125* (17), 2597.

12. Dong, L. M.; Wilson, C.; Wardell, M. R.; Simmons, T.; Mahley, R. W.; Weisgraber, K. H.; Agard, D. A., Human apolipoprotein E. Role of arginine 61 in mediating the lipoprotein preferences of the E3 and E4 isoforms. *Journal of Biological Chemistry* **1994,** *269* (35), 22358-22365.

13. Dong, L.-M.; Weisgraber, K. H., Human Apolipoprotein E4 Domain Interaction: ARGININE 61 AND GLUTAMIC ACID 255 INTERACT TO DIRECT THE PREFERENCE FOR VERY LOW DENSITY LIPOPROTEINS. *Journal of Biological Chemistry* **1996,** *271* (32), 19053-19057.

14. Ma, J.; Yee, A.; Brewer, H. B.; Das, S.; Potter, H., Amyloid-associated proteins [alpha]1-antichymotrypsin and apolipoprotein E promote assembly of Alzheimer [beta]-protein into filaments. *Nature* **1994,** *372* (6501), 92-94.

15. Kohlschütter, A.; Chappuis, D.; Meier, C.; Tönz, O.; Vassella, F.; Herschkowitz, N., Familial epilepsy and yellow teeth--a disease of the CNS associated with enamel hypoplasia. *Helvetica paediatrica acta* **1974,** *29* (4), 283-294.

16. Christodoulou, J.; Hall, R.; Menahem, S.; Hopkins, I.; Rogers, J., A syndrome of epilepsy, dementia, and amelogenesis imperfecta: genetic and clinical features. *Journal of medical genetics* **1988,** *25* (12), 827-830.

17. Zlotogora, J.; Fuks, A.; Borochowitz, Z.; Tal, Y., Kohlschütter-Tönz syndrome: Epilepsy, dementia, and amelogenesis imperfecta. *American journal of medical genetics* **1993,** *46* (4), 453-454.

18. Haberlandt, E.; Svejda, C.; Felber, S.; Baumgartner, S.; Günther, B.; Utermann, G.; Kotzot, D., Yellow teeth, seizures, and mental retardation: a less severe case of Kohlschütter–Tönz syndrome. *American Journal of Medical Genetics Part A* **2006,** *140* (3), 281-283.

19. Schossig, A.; Wolf, N. I.; Kapferer, I.; Kohlschutter, A.; Zschocke, J., Epileptic encephalopathy and amelogenesis imperfecta: Kohlschutter-Tonz syndrome. *Eur J Med Genet* **2012,** *55* (5), 319-22.

20. Mory, A.; Dagan, E.; Shahor, I.; Mandel, H.; Illi, B.; Zolotushko, J.; Kurolap, A.; Chechik, E.; Valente, E. M.; Amselem, S.; Gershoni-Baruch, R., Kohlschutter-Tonz syndrome: clinical and genetic insights gained from 16 cases deriving from a close-knit village in Northern Israel. *Pediatr Neurol* **2014,** *50* (4), 421-6.

21. Mory, A.; Dagan, E.; Illi, B.; Duquesnoy, P.; Mordechai, S.; Shahor, I.; Romani, S.; Hawash-Moustafa, N.; Mandel, H.; Valente, E. M.; Amselem, S.; Gershoni-Baruch, R., A nonsense mutation in the human homolog of Drosophila rogdi causes Kohlschutter-Tonz syndrome. *Am J Hum Genet* **2012,** *90* (4), 708-14.

22. Schossig, A.; Wolf, N. I.; Fischer, C.; Fischer, M.; Stocker, G.; Pabinger, S.; Dander, A.; Steiner, B.; Tonz, O.; Kotzot, D.; Haberlandt, E.; Amberger, A.; Burwinkel, B.; Wimmer, K.; Fauth, C.; Grond-Ginsbach, C.; Koch, M. J.; Deichmann, A.; von Kalle, C.; Bartram, C. R.; Kohlschutter, A.; Trajanoski, Z.; Zschocke, J., Mutations in ROGDI Cause Kohlschutter-Tonz Syndrome. *Am J Hum Genet* **2012,** *90* (4), 701-7.

23. Huckert, M.; Mecili, H.; Laugel-Haushalter, V.; Stoetzel, C.; Muller, J.; Flori, E.; Laugel, V.; Maniere, M. C.; Dollfus, H.; Bloch-Zupan, A., A Novel Mutation in the ROGDI Gene in a Patient with Kohlschutter-Tonz Syndrome. *Mol Syndromol* **2014,** *5* (6), 293-8.

24. Tucci, A.; Kara, E.; Schossig, A.; Wolf, N. I.; Plagnol, V.; Fawcett, K.; Paisan-Ruiz, C.; Moore, M.; Hernandez, D.; Musumeci, S.; Tennison, M.; Hennekam, R.; Palmeri, S.; Malandrini, A.; Raskin, S.; Donnai, D.; Hennig, C.; Tzschach, A.; Hordijk, R.; Bast, T.; Wimmer, K.; Lo, C. N.; Shorvon, S.; Mefford, H.; Eichler, E. E.; Hall, R.; Hayes, I.; Hardy, J.; Singleton, A.; Zschocke, J.; Houlden, H., Kohlschutter-Tonz syndrome: mutations in ROGDI and evidence of genetic heterogeneity. *Hum Mutat* **2013,** *34* (2), 296-300.

25. Lipina, T. V.; Roder, J. C., Disrupted-In-Schizophrenia-1 (DISC1) interactome and mental disorders: impact of mouse models. *Neuroscience & Biobehavioral Reviews* **2014,** *45*, 271-294.

26. Soares, D. C.; Carlyle, B. C.; Bradshaw, N. J.; Porteous, D. J., DISC1: structure, function, and therapeutic potential for major mental illness. *ACS chemical neuroscience* **2011,** *2* (11), 609-632.

27. Chen, Y.-F.; Cho, J. J.; Huang, T.-H.; Tseng, C.-N.; Huang, E.-Y.; Cho, C.-L., Downregulation of a novel human gene, ROGDI, increases radiosensitivity in cervical cancer cells. *Cancer Biology & Therapy* **2016,** *17* (10), 1070-1078.

28. Abba, M. C.; Hu, Y.; Sun, H.; Drake, J. A.; Gaddis, S.; Baggerly, K.; Sahin, A.; Aldaz, C. M., Gene expression signature of estrogen receptor α status in breast cancer. *BMC Genomics* **2005,** *6* (1), 37.

29. Hutchinson, E. G.; Thornton, J. M., The Greek key motif: extraction, classification and analysis. *Protein Engineering, Design and Selection* **1993,** *6* (3), 233-245.

30. Alber, T., Structure of the leucine zipper. *Current opinion in genetics & development* **1992,** *2* (2), 205-210.

31. Busch, S. J.; Sassone-Corsi, P., Dimers, leucine zippers and DNA-binding domains. *Trends in Genetics* **1990,** *6*, 36-40.

32. Holm, L.; Rosenström, P., Dali server: conservation mapping in 3D. *Nucleic acids research* **2010,** *38* (Web Server issue), W545-W549.

33. Suzuki, H.; Nishizawa, T.; Tani, K.; Yamazaki, Y.; Tamura, A.; Ishitani, R.; Dohmae, N.; Tsukita, S.; Nureki, O.; Fujiyoshi, Y., Crystal structure of a claudin provides insight into the architecture of tight junctions. *Science* **2014,** *344* (6181), 304-307.

34. Kamtekar, S.; Hecht, M. H., Protein Motifs. 7. The four-helix bundle: what determines a fold? *The FASEB Journal* **1995,** *9* (11), 1013-22.

35. Nakagawa, S.; Maeda, S.; Tsukihara, T., Structural and functional studies of gap junction channels. *Current Opinion in Structural Biology* **2010,** *20* (4), 423-430.

36. Narayanaswami, V.; Kiss, R. S.; Weers, P. M. M., The helix bundle: A reversible lipid binding motif. *Comparative biochemistry and physiology. Part A, Molecular & integrative physiology* **2010,** *155* (2), 123-133.

37. Greenfield, N. J., Determination of the folding of proteins as a function of denaturants, osmolytes or ligands using circular dichroism. *Nature protocols* **2006,** *1* (6), 2733-2741.

38. Saitoh, Y.; Suzuki, H.; Tani, K.; Nishikawa, K.; Irie, K.; Ogura, Y.; Tamura, A.; Tsukita, S.; Fujiyoshi, Y., Structural insight into tight junction disassembly by *Clostridium perfringens* enterotoxin. *Science* **2015,** *347* (6223), 775.

39. Shinoda, T.; Shinya, N.; Ito, K.; Ohsawa, N.; Terada, T.; Hirata, K.; Kawano, Y.; Yamamoto, M.; Kimura-Someya, T.; Yokoyama, S.; Shirouzu, M., Structural basis for disruption of claudin assembly in tight junctions by an enterotoxin. *Scientific Reports* **2016,** *6*, 33632.

40. De Souza, C. M.; Souza, J.; Furtado, C. M. G.; Cleto, J. L. T.; Antoniuk, S. A.; Raskin, S., Kohlschütter-Tönz syndrome in siblings without ROGDI mutation. *Oral health and dental management* **2014,** *13* (3), 728-730.

41. Schossig, A.; Bloch-Zupan, A.; Lussi, A.; Wolf, N. I.; Raskin, S.; Cohen, M.; Giuliano, F.; Jurgens, J.; Krabichler, B.; Koolen, D. A.; de Macena Sobreira, N. L.; Maurer, E.; Muller-Bolla, M.; Penzien, J.; Zschocke, J.; Kapferer-Seebacher, I.; Joseph, C.; Perelman, S.; von Hülsen, E.; de Souza, C.; Kohlschütter, A.; Tönz, O.; Verhoeven, J. S., SLC13A5 is the second gene associated with Kohlschütter–Tönz syndrome. *Journal of Medical Genetics* **2016,** *54* (1), 54-62.

42. Rupaimoole, R.; Lee, J.; Haemmerle, M.; Ling, H.; Previs, Rebecca A.; Pradeep, S.; Wu, Sherry Y.; Ivan, C.; Ferracin, M.; Dennison, Jennifer B.; Millward, Niki M. Z.; Nagaraja, Archana S.; Gharpure, Kshipra M.; McGuire, M.; Sam, N.; Armaiz-Pena,

Guillermo N.; Sadaoui, Nouara C.; Rodriguez-Aguayo, C.; Calin, George A.; Drapkin, Ronny I.; Kovacs, J.; Mills, Gordon B.; Zhang, W.; Lopez-Berestein, G.; Bhattacharya, Pratip K.; Sood, Anil K., Long Noncoding RNA Ceruloplasmin Promotes Cancer Growth by Altering Glycolysis. *Cell Reports* **2015,** *13* (11), 2395-2402.

43. Otwinowski, Z.; Minor, W., [20] Processing of X-ray diffraction data collected in oscillation mode. In *Methods in Enzymology*, Charles W. Carter, Jr., Ed. Academic Press: 1997; Vol. Volume 276, pp 307-326.

44. Terwilliger, T. C.; Berendzen, J., Automated MAD and MIR structure solution. *Acta Crystallogr D Biol Crystallogr* **1999,** *55* (Pt 4), 849-61.

45. McCoy, A. J.; Grosse-Kunstleve, R. W.; Adams, P. D.; Winn, M. D.; Storoni, L. C.; Read, R. J., Phaser crystallographic software. *Journal of applied crystallography* **2007,** *40* (4), 658-674.

Acknowledgements

먼저 학부 3학년 때부터 학부연구생을 시작으로 박사학위까지 마무리할 수 있도록 이끌어 주신 이창욱 교수님께 감사드립니다. 많이 부족하고 힘들었지만, 아낌없는 격려와 도움을 주셔서 박사학위를 마칠 수 있게 되었습니다. 여기서 끝이 아니라 앞으로 더 발전하고 훌륭한 과학자가 되도록 노력하겠습니다.

그리고 저에게 공동연구의 기회를 주신 강병헌 교수님과 이현우 교수님께 감사드립니다. 공동연구를 통해 박사학위 과정동안 다양한 연구분야를 경험하고 좋은 결과를 얻을 수 있었습니다. 학위논문 심사일 맡아주시고, 학위논문을 마무리 하는데 큰 조언과 의견을 주신 강병헌 교수님, 채영찬 교수님, 김은희 교수님, 박철민 교수님께도 감사드립니다.

그리고 많은 시간을 함께 보내온 연구실 동료들에게 감사드립니다. 연구실 생활을 시작하면서 전반적인 실험에 대해서 알려주고 선배로서 이끌어준 한빈이 형과 대학원 생활동안 많이 부족한 저를 도와주고 함께 연구실에서 고생한 주미, 동영, 현우, 서황, 혜진이에게도 고맙습니다.

또한 중학교 때부터 인생의 가장 많은 시간을 공유하고 기쁠 때나 힘들 때나 언제든 힘이 되어준 화용, 현승, 건엽이에게 고맙다는 말을 하고 싶습니다. 그리고 처음 울산에 왔지만 잘 적응하고 재밌게 생활할 수 있도록 도와준 태훈, 황필, 형준이에게도 고맙다고 전합니다. 이 외에도 박사학위 과정동안 도움을 주셨던 모든 분들께 감사드립니다.

마지막으로, 어떤 상황에서도 무조건적인 사랑과 응원, 그리고 저의 의견을 항상 존중해준 어머니, 외가 친척 분들께 감사하고 사랑한다는 말을 전하고 싶습니다.